

Aus dem Deutschen Krebsforschungszentrum
Vorstand: Prof. Dr. med. Dr. h. c. Michael Baumann, Ursula Weyrich
Abteilung Medizinische Physik in der Strahlentherapie
Leiter: Prof. Dr. Oliver Jäkel

**In-phantom dosimetry study for target and
organs at risk during breathing-induced motion:
improving pancreatic cancer treatment by
combining carbon ion and mini-beam irradiation**

Inauguraldissertation
zur Erlangung des Doctor scientiarum humanarum (Dr. sc. hum.)
an der
Medizinischen Fakultät Heidelberg
der
Ruprecht-Karls-Universität

vorgelegt von
Christina Stengl
aus Worms

Juni 2024

Dekan: Herr Prof. Dr. Michael Boutros
Doktorvater: Herr Prof. Dr. Oliver Jäkel

Contents

List of Abbreviations	7
Introduction	9
1.1 Pancreatic cancer	9
1.2 Photons and ions for radiotherapy	11
1.3 Spatial fractionated dose delivery	15
1.4 Combination of CIRT and MBRT	19
1.5 Organ motion impact on radiotherapy	19
1.6 Phantoms for radiotherapy	20
1.7 Goal of this thesis	24
Publications for cumulative thesis	25
2.1 Paper I: Abdominal anthropomorphic phantom PPIeT	27
2.2 Paper II: Mini-beam collimator	43
2.3 Paper III: Organ motion during carbon ion mini-beam therapy	61
Discussion	77
3.1 3D printing for radiotherapy	77
3.2 Anthropomorphic phantoms	80
3.3 Carbon ion therapy	83
3.4 Spatial fractionation in radiotherapy	85
3.5 Phantom irradiation with iMBRT	87
3.6 Organ motion during radiotherapy	89
Conclusion	93

Summary	94
Zusammenfassung	95
References	97
Personal Contribution to Data Acquisition / Assessment and Personal Publications	111
8.1 Contribution to publications for cumulative thesis	111
8.2 Peer-reviewed publications	112
8.3 Conference contributions	113
Appendix	115
9.1 Supplementary material Paper I	116
9.2 Supplementary material Paper II	121
9.3 Supplementary material Paper III	131
9.4 CV - Christina Stengl	141
Acknowledgments	143
Eidesstattliche Versicherung	145

List of Abbreviations

ABS	acrylonitrile butadiene styrene
AP	anterior-posterior
ARDOS	Advanced Radiation DOSimetry
BMI	body mass index
CC	cranial-caudal
CIRT	carbon ion radiotherapy
CT	computer tomography
ctc	center-to-center distance
DIBH	deep inspiration breath hold
DNA	deoxyribonucleic acid
DSBs	double-strand breaks
FDM	fused deposition modeling
FWHM	full width at half maximum
GI	gastrointestinal
HIT	Heidelberg Ion Beam Therapy Center
HR	homologous recombination
HU	Hounsfield unit
IC	ionization chamber
ICRU	International Commission on Radiation Units and Measurements
IL	interleukin
iMBRT	ion mini-beam radiotherapy
INF	interferon
LEM	local effect model
LET	linear energy transfer
LINAC	linear accelerator
MC	Monte Carlo
MRgRT	magnetic resonance image-guided radiotherapy
MRI	magnetic resonance imaging
MRT	microbeam radiotherapy
MBRT	mini-beam radiotherapy
NiDTPA	nickel-diethylenetriaminepentaacetic acid
NHEJ	non-homologous end-joining

OARs	organs at risk
OD	optical density
OER	oxygen enhancement ratio
OSLD	optically stimulated luminescence detectors
PACK	pancreatic cancer and carbon ion radiotherapy
PDAC	pancreatic ductal adenocarcinoma
PET	positron emission tomography
PLA	polylactic acid
PMMA	polymethylmethacrylate
PPIeT	Pancreas Phantom for Ion beam Therapy
PVDR	peak-to-valley dose ratio
RBE	relative biological effectiveness
RG	respiratory gating
RL	right-left
ROS	reactive oxygen species
SCD	source-to-collimator distance
SFRT	spatially fractionated radiation therapy
SOBP	spread-out Bragg peak
SPECT	single photon emission computed tomography
SSBs	single-strand breaks
TLD	thermoluminescent detector
VPDR	valley-to-peak dose ratio

1. Introduction

Pancreatic cancer poses significant challenges due to its aggressive progression and poor prognosis (Liu et al. 2022). The treatment options for this cancer are scarce, with the surgical intervention being the only potential cure (Rawla et al. 2019). However, pancreatic cancer patients are often diagnosed in an advanced and inoperable stage. Consequently, there is a pressing need for novel therapeutic approaches to enhance survival rates and quality of life. Recent advancements in radiotherapy have yielded two promising treatment modalities: mini-beam radiotherapy (MBRT) and carbon ion radiotherapy (CIRT). Latter has already demonstrated favorable oncological outcomes in clinical studies (Kawashiro et al. 2018). Nevertheless, factors such as breathing and bowel motion within the abdomen may lead to inadequate coverage of the tumor and overexposure of the organs at risk (OARs) during radiotherapy (Velec et al. 2011). Therefore, accurate evaluation of the dose distribution in both, the tumor and OARs, is crucial for assessing the effectiveness of these techniques.

1.1 Pancreatic cancer

Pancreatic cancer ranks as the seventh leading cause of global cancer-related mortality, with a five-year survival rate ranging from 5 % to 10 %. By 2030, it is estimated to become the second leading cause of cancer-related death in the United States (Anderson et al. 2021). Approximately 90 % of pancreatic cancer cases are attributed to pancreatic ductal adenocarcinoma (PDAC) (Park et al. 2021). Despite the application of standard treatments including the three foundational pillars of cancer treatment, namely surgery, chemotherapy, and radiotherapy, their effectiveness remains only partially satisfactory (Figure 1) (Jan and Ch'ang 2023). This may be attributed to factors such as late diagnosis or significant resistance exhibited by PDAC against these treatment modalities.

Treatment of pancreatic cancer

The assessment of resectability, referring to the capacity to remove the cancer fully, is crucial in selecting the most suitable treatment method for PDAC. For each patient, the tumor is categorized as either resectable PDAC, borderline resectable PDAC, or locally advanced PDAC, depending on factors such as tumor size and invasion into

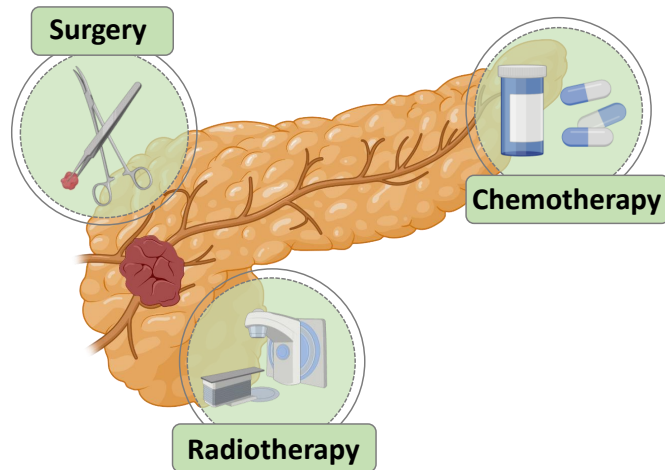


Figure 1: Treatment options for pancreatic cancer including surgery, chemotherapy and radiotherapy. Created using Biorender, adapted from (Liu et al. 2023).

neighboring vessels (Park et al. 2021). Locally advanced PDAC is characterized by the extent of tumor invasion into adjacent blood vessels. Unfortunately, a significant number of patients experience an asymptomatic early onset of the disease, leading to its discovery only in an advanced and therefore mostly inoperable state (Bouchart et al. 2020). In general, the initial treatment of locally advanced PDAC involves different chemotherapy regimes such as FOLFIRINOX or Gemcitabine/nab-Paclitaxel (Principe et al. 2021). If a tumor is still unresectable after chemotherapy, the combination of simultaneous chemotherapy and conventional radiation therapy, also called chemoradiotherapy, might be an option. Nonetheless, its role remains disputed since several randomized studies have failed to demonstrate a survival benefit (Garajová et al. 2023). An analysis of 11 trials with 794 patients indicated that chemoradiation led to improved survival compared to radiotherapy alone (Sultana et al. 2017, Park et al. 2021). Comparing chemotherapy with concurrent chemoradiotherapy, the addition of radiotherapy contributed to an extension in median survival time, increasing from 9.2 months to 11.1 months. However, this was associated with an increased occurrence of adverse side effects, such as fatigue and gastrointestinal (GI) toxicities (Loehrer et al. 2011, Falco et al. 2023). However, another study yielded contrasting findings, indicating that chemoradiotherapy led to more toxic and less effective treatment of locally advanced PADC compared to chemotherapy with gemcitabine alone (Chauffert et al. 2008). Transitioning from conventional radiotherapy to other treatment regimes such as intensity-modulated radiation therapy or image-guided radiotherapy, decreases the previously found toxicity, while the same outcome is achieved (Bittner et al. 2015, Falco et al. 2023).

Challenges in pancreatic cancer

Nevertheless, uncertainties remain regarding the role of radiation, the optimal radiation modality, and the dosing schedule for locally advanced PDAC. Although the combination of radiation therapy with chemotherapy might provide an improved treatment approach, several challenges must be addressed. One of them is the pronounced hypoxia in the micro-environment of locally advanced PDAC (Wang et al. 2022). During tumor progression, the chaotic and rapid growth of the tumor stimulates increased angiogenesis, resulting in a permeable vasculature lacking the ability to effectively transport oxygen and nutrients to each part of the tumor tissue, making the tumor partially hypoxic (Abou Khouzam et al. 2023). Treating hypoxic tumors, particularly with photon irradiation, is difficult because oxygen is required to generate reactive oxygen species (ROS), which play a key role in causing deoxyribonucleic acid (DNA) damage. As a result, achieving the desired tumor control is challenging (Dewhirst et al. 2008, Graham and Unger 2018, Huang et al. 2020, Telarovic et al. 2021).

Additionally, the radiation dose for treating locally advanced PADC is constrained by the proximity of critical intestinal organs also referred to as OARs. In the case of the pancreas, the main OARs to be considered are the duodenum, the two kidneys, the spine and the spinal cord (Petit et al. 2012, Malouff et al. 2020, Wang et al. 2022). Nevertheless, the recent advancements in technology, particularly MR-guided radiotherapy (MRgRT) and adaptive planning have reopened the possibility of irradiating PDAC due to improved protection of OARs (Meyer et al. 2023).

The pancreas's position in the abdomen, along with its neighboring OARs, presents an additional challenge for radiotherapy. These organs are prone to motion caused by respiration and digestion, further complicating the treatment of pancreatic cancer. Typically irradiation treatments aim at delivering a homogeneous dose distribution. However, breathing-induced pancreas motion can be significant, reaching up to 27.3 mm with high variations in standard deviation (Bussels et al. 2003, Bhasin et al. 2006, Knybel et al. 2014, Dolde et al. 2019, Jing et al. 2021). Therefore, this organ motion can blur the boundaries between the tumor and its OARs, potentially leading to a higher dose in the OARs and inhomogeneous dose distribution within the pancreas tumor (Jing et al. 2021). Apart from breathing-induced motion, gradual displacement of GI organs can occur due to bowel peristalsis, muscle relaxation, or tensioning (Grimbergen et al. 2021). Given these challenges and only moderate improvements in treatment outcomes with chemotherapy and radiotherapy, there is a need for further progress in therapeutic options.

1.2 Photons and ions for radiotherapy

Radiotherapy continuously evolves, providing a non-invasive approach to treat cancer by employing ionizing irradiation. The primary modalities for ionizing

irradiation of cancer treatments are photons, electrons and charged particles such as protons and carbon ions. Each of these modalities possesses distinct physical and biological characteristics that determine their efficacy in treating different tumor types.

Physical properties of irradiation

The radiation response of the tumor is influenced by several physical factors such as the linear energy transfer (LET), determining the energy deposition events of radiation. Photon irradiation disperses energy in all directions, resulting in sparse energy deposition, and is thus classified as low-LET radiation. In contrast, charged particles focus their energy along the primary track, leading to dense energy deposition, and are consequently termed high-LET radiation (Nickoloff 2015, Busato et al. 2022). This property is advantageous as it leads to increased and complex DNA damage, which results in a high relative biological effectiveness (RBE). The RBE is the ratio of biological effectiveness between one form of ionizing radiation, usually considering photons as reference and another radiation type when the same dose is absorbed (Busato et al. 2022, Vedelago et al. 2022). In clinical practice, treatment planning takes into consideration both RBE and LET to tailor therapeutic doses for effective cancer treatment while minimizing adverse effects (Palumbo et al. 2019).

Another advantage of particle radiotherapy is that the majority of the dose is concentrated in a well-defined depth in the tissue determined by the initial energy of the particle. This characteristic in-depth dose deposition of charged particles is known as the “Bragg peak” (Figure 2 A). Thereby, improved dose localization compared to photons can be achieved by employing a spectrum of energies to cover the whole tumor geometry, named “spread-out Bragg peak” (SOBP) (Figure 2 B). This results in the possibility of modulating radiation dose intensity along the beam trajectory, resulting in a relative increase in dose to the tumor target compared to normal tissue in the entrance region. This way, the effect of dose to OARs is minimized, thus potentially reducing toxicity. Furthermore, since only a small percentage of energy is emitted beyond the point where the particles come to rest, normal tissue located behind the tumor receives minimal to no radiation dose (Scharadt et al. 2010, Nichols 2015, Jäkel 2020, Wang et al. 2022).

Biological effects of radiotherapy

Radiation absorbed by cells can lead to DNA damage, initiating processes such as apoptosis, necrosis, and senescence in cancer cells (Wang et al. 2018). It causes DNA damage either directly by energy deposition leading to single-strand breaks (SSBs), double-strand breaks (DSBs), DNA crosslinks and DNA-protein cross-links or indirectly by generating ROS, which damages DNA, lipids, and proteins (Dertinger and Jung 1970). Particular DSBs are difficult to repair and are the major factor responsible for cell death (Mahaney et al. 2009, Vignard et al. 2013). One main

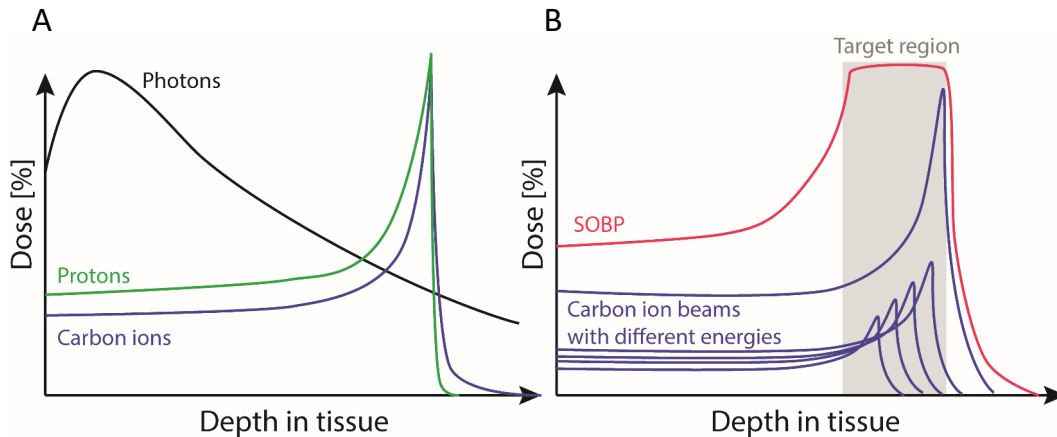


Figure 2: Dose distribution of photon beam (black), proton beam (green) and carbon ion beam (blue) over tissue depth (A). Multiple mono-energetic carbon ion beams are used to create the SOBP to cover the whole target (B).

indicator for DSBs induced by ionizing irradiation is the phosphorylation of histone H2AX on serine 139 (known as γ H2AX) (Sak and Stuschke 2010). In general, DSBs can be repaired by two different pathways, homologous recombination (HR) and non-homologous end-joining (NHEJ). However, if the repair mechanisms fail, these lesions can trigger apoptosis or senescence (Wang et al. 2018). Photon irradiation primarily results in isolated lesions such as SSBs. In contrast to photons, carbon ions induce more direct and clustered DNA damage, making them more lethal (Lopez Perez et al. 2019, van de Kamp et al. 2021). Consequently, the landscape of radiotherapy modalities has rapidly expanded over recent decades, with particle therapy emerging as a promising treatment option.

Comparison of carbon ions and protons

Particle therapy mainly involves the use of either carbon ions or protons (Kiseleva et al. 2022). Although they have some physical attributes in common, such as the Bragg peak, carbon ions and protons differ according to their radiobiological properties and characteristics of the beam. Carbon ions exhibit a narrower lateral penumbra compared to protons, due to their increased mass, which leads to reduced deflection, resulting in a more localized dose distribution (Wang et al. 2022). Additionally, proton beams have a lower LET similar to photons, while carbon ions exhibit high LET characteristics. The radiobiology associated with low LET irradiation is well understood, however, there is limited clinical data characterizing the RBE of high LET irradiation (Glowa et al. 2017, Vedelago et al. 2022). While the RBE of protons compared to photons is accepted as 1.1, indicating that proton beams offer a 10 % higher RBE compared to photons for equivalent physical

dose delivery, the RBE of carbon ions is higher, within 2.5 and 3.5, depending on the initial energy of the carbon ions, also varying between the tumor and normal tissue (Nichols 2015, Wang et al. 2022). When RBE models are used for the dose calculation in the treatment plan, usually the units Gy (RBE) are used instead of Gy.

Additionally, carbon ions are more effective against hypoxic tumors due to their low oxygen enhancement ratio (OER) (Wang et al. 2022). The OER is the ratio of radiation required to produce the same biological effect for hypoxic conditions and oxygenated conditions (Sokol and Durante 2023). Heavy ions primarily cause direct DNA damage, thus reducing their dependence on free radical production and surrounding oxygen concentrations (Hirayama et al. 2009, Sokol and Durante 2023).

However, certain aspects related to CIRT require further consideration. For instance, the fragmentation tail distal to the tumor deposits more dose beyond the Bragg peak compared with protons. This is attributed to the presence of lower atomic weight particles resulting from the fragmentation of primary carbon ions or fragments generated within the target tissue atoms. Additionally, carbon ion irradiation may result in increased damage to normal tissue, particularly in the entrance region of the beam compared to lighter ions (Volz et al. 2023). This could potentially increase the risk of secondary cancer (Girst et al. 2016, Martinez-Rovira et al. 2017, Volz et al. 2023).

Carbon ion treatment for pancreatic cancer

Due to the radioresistance and lack of therapy options for pancreatic cancer, carbon ions might be a highly promising choice. Nevertheless, CIRT facilities are expensive and ongoing clinical studies are still evaluating the potential benefits of CIRT for pancreatic cancer. Currently, there are only 12 carbon ion radiotherapy facilities operational in Austria, China, Germany, Italy, and Japan (Malouff et al. 2020, Liermann et al. 2020b, Durante et al. 2021).

Therefore, CIRT trials are sparse, however, they were already introduced as a preoperative treatment modality as well as a definite treatment method for locally advanced PDAC and locally recurrent pancreatic cancer (Liermann et al. 2020b). Thus far, Shinoto et al. (2013) demonstrated a phase I trial for CIRT as a preoperative treatment modality, increasing the dose from 30 Gy (RBE) up to 36.8 Gy (RBE) in 8 fractions over 2 weeks (Shinoto et al. 2013). CIRT was well tolerated and resection could be performed in 81 % of the cases. An overall survival of 48 % over 5 years was reported (Shinoto et al. 2013, Liermann et al. 2020b). As a drawback, distant metastasis were found in a majority of the patients increasing the need for additional chemotherapy. Nonetheless, the data provide a promising foundation for subsequent trials, which are currently ongoing with concurrent chemotherapy applications of Gemcitabine or FOLFIRINOX (Vitolo et al. 2019).

Another trial treating locally advanced PDAC with CIRT and concurrent Gemcitabine application has been demonstrated by Shinoto et al. (2016) using a dose-escalating radiation scheme from 43.2 Gy (RBE) up to 55.2 Gy (RBE) for 12 fractions (Shinoto et al. 2016). There was only one instance of clearly radiation-induced grade 3 toxicity, including severe pain and vomiting, but the overall survival was 19.6 months. Kawashiro et al. (2018) conducted a retrospective analysis of CIRT for locally advanced PDAC (Kawashiro et al. 2018). Concurrent chemotherapy was administered to 57 % of the patients. The 1- and 2-year overall survival rates were reported as 79 % and 51 %, respectively. A significant improvement in overall survival compared to photon irradiation, increasing from approximately one to two years, was observed. Notably, no instances of clearly radiation-induced grade 3 toxicity were found.

A currently ongoing study is the pancreatic cancer and carbon ion radiotherapy (PACK)-study at the Heidelberg Ion Beam Therapy Center (HIT), Germany, that investigates CIRT in patients with locally advanced PDAC or locally recurrent pancreatic cancer looking for the overall survival after 12 months (Liermann et al. 2020a). Additionally, secondary endpoints are assessed including progression-free survival, safety, and quality of life. In this study, 48 Gy (RBE) was applied in 12 fractions. In general, due to the limited data worldwide on further prospective studies, the efficacy of CIRT needs to be further evaluated as precise radiobiological responses to charged particle irradiation remain incompletely understood (Liu et al. 2022).

1.3 Spatial fractionated dose delivery

Recent advancements in technology, such as mini-beam radiotherapy (MBRT), aim to minimize normal tissue damage in the entrance channel. Therefore, the combination of MBRT with CIRT presents a promising possibility, offering a synergistic approach to enhance the strengths of both techniques (Martinez-Rovira et al. 2017, Volz et al. 2023).

Mini-beam dose distribution parameters

MBRT is a form of spatially fractionated radiation therapy (SFRT), a technique that uses spatially modulated beams to create alternating regions of high and low doses, which strongly differs from homogeneous conventional radiotherapy (Mali 2024). It has a century-long history and was pioneered in 1909 when the initial method of SFRT was delivered as GRID therapy (Kohler 1909, Laissue et al. 2012, Yan et al. 2019). With this technique, bulky tumors were frequently treated by administering a non-uniform dose using an attenuation block. Selected areas were blocked, creating a field of high and low doses, resulting in higher tolerance for the

healthy tissue (Yan et al. 2019). In the 1990s, spatial fractionation was rediscovered, leading to the introduction of microbeam radiotherapy (MRT) and MBRT (Meyer et al. 2019, Datzmann et al. 2020). While MRT employs usually peak sizes of up to 50 μm and valley sizes of 200 μm to 400 μm , the mini-beam pattern typically employs valley regions ranging from 1.0 mm to 4.0 mm, being separated by air gaps ranging from 0.2 mm to 1.0 mm, thus creating the peaks (Prezado 2017, Bazyar et al. 2017, Treibel et al. 2021, Tubin et al. 2023).

To describe the geometry of the mini-beam pattern, different parameters have been reported (Schneider 2022, Ortiz et al. 2022). Two commonly used geometrical parameters are the full width at half maximum (FWHM) and the center-to-center distance (ctc). Modifying the FWHM of the peaks significantly affects radiation toxicity. For instance, FWHM ranging from 0.5 mm to 1.0 mm did not result in any observable toxic effects. However, in an *in vivo* mice experiment, a peak width of 3.0 mm led to severe skin reactions (Sammer et al. 2019). Another commonly used parameter, linked to the biological response is the peak-to-valley dose ratio (PVDR). It was found, that a higher PVDR was associated with a more pronounced tissue sparing (Dilmanian et al. 2002, Schneider et al. 2020).

Mechanisms of the mini-beam effect

The so-called mini-beam effect, responsible for the sparing of healthy tissue and the preferential targeting of tumors remains poorly understood, especially considering the biological processes leading to this effect (Girst et al. 2016, Mazal et al. 2020, Bertho et al. 2023). In SFRT, potential mechanisms may include the bystander effects, as well as changes in vascularization and immunomodulation (Billena and Khan 2019). The bystander effect is usually defined as the biological response of a cell reacting to an event in a nearby cell. This effect is dependent on intercellular communication and can amplify the outcomes of the original event (Mitchel 2004). In the context of spatial fractionation, bystander cells are those located in the valley area. These cells undergo cell death to a greater extent than would be expected solely from exposure to valley dose, indicating a cytotoxic bystander effect (Asur et al. 2012). An additional factor playing a role in the mini-beam effect might be the altered tumor microvasculature. Spatial fractionation demonstrated selective vascular damage in immature tissue, such as tumor tissue, compared to mature tissue. For the immature tissue, the regeneration of the vessel was not possible anymore (Brönnimann et al. 2016). On top of that, the immune system might also be a factor playing a role in the mini-beam effect. Spatial fractionation increased the secretion of interleukin 10 (IL-10) and proinflammatory cytokines such as interleukin 6 (IL-6) and interferon- γ (INF- γ). These cytokines are rapidly released upon SFRT, aligning with the observations of rapid and increased intratumoral infiltration of T-cells compared to broad beam irradiation. However, within immunodeficient mice, spatial fractionation did not lead to an anti-tumor immune response linking the mini-beam effect to the immune system (Bertho et al. 2023).

MBRT: X-ray and proton applications

Originally, MBRT was developed in synchrotrons, but it has been demonstrated that this technique can also be applied in conventional orthovoltage small animal irradiators (Treibel et al. 2021, Sotiropoulos et al. 2021). For X-rays, the mini-beam pattern traverses the entire tissue depth with uniform intensity similar to broad-beam X-ray irradiation (Figure 3 A). It was demonstrated that MBRT with X-rays could enhance the therapeutic index compared to conventional radiotherapy as the tissue tolerance in mice brains increased significantly. Normal brain tissue appeared to tolerate peak doses up to 100 Gy with valley doses of 7 Gy (Sotiropoulos et al. 2021). Another study investigated MRT with X-rays of the spinal cord of rats with similar findings (Dilmanian et al. 2006). It was reported that three out of four mice survived over 7 months after a 400 Gy peak dose MRT irradiation. In contrast, using a comparable broad-beam dose led to a 75 % rate of paralysis in the mice.

Nonetheless, the amount of mini-beam studies with X-rays remains limited. Particle radiotherapy, especially with protons, shows potential benefits over X-rays by providing improved dose conformity at the tumor site. Similar physical characteristics of spatial fractionation can be achieved when using charged particles for generating mini-beams. As an advantage of the mini-beams generated with charged particles, the multiple Coulomb scattering leads to a broadening of the FWHM of every single mini-beam resulting in a homogeneous coverage of the target site, similar to conventional radiotherapy (Figure 3 A, B). Consequently, there has been an increase in particle MBRT studies over the last decade (Dilmanian et al. 2015, Schneider 2022). One of the pioneering studies with protons produced a mini-beam pattern with a FWHM of 400 μm and 700 μm and ctcs of 3200 μm and 3500 μm (Peucelle et al. 2015). Biological analysis from this study, along with others, demonstrated enhanced healthy tissue sparing, as evidenced by the absence of skin damage and significantly reduced brain damage compared to broad-beam irradiation, later confirmed by subsequent publications (Prezado et al. 2017b, Meyer et al. 2019).

Generation of mini-beam patterns

For generating proton mini-beam patterns, there are several options available including the use of a mini-beam collimator made from various metals like brass or tungsten or the magnetically focusing of the beam to achieve the desired beam width (Prezado et al. 2017a, Schneider et al. 2020, Prezado 2021, Volz et al. 2023). Magnetically focused beams lead to an increase in the achievable PVDR and an overall improvement of the efficiency of the treatment outcome. This, however, makes modifications to the current proton beam nozzles necessary, or even the installation of a new linear accelerator (Kim et al. 2022). Additionally, up to date, there are no facilities with the technology to deliver magnetically focused carbon ions for mini-beam patterns (Volz et al. 2023). This limitation extends to

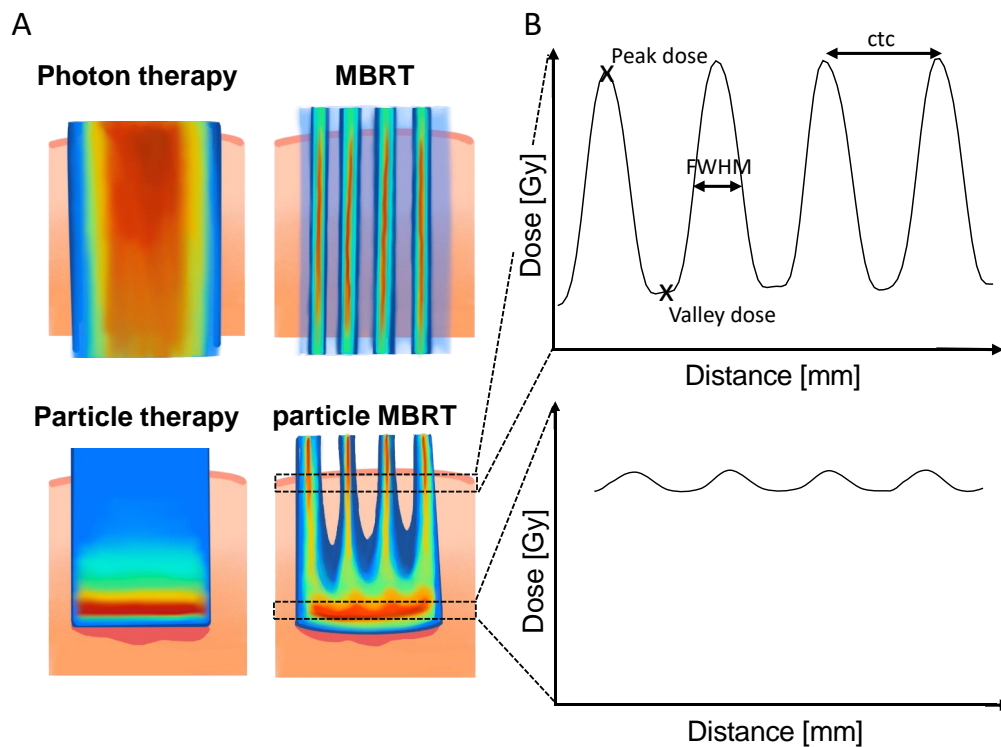


Figure 3: Illustration of beam distribution in tissue for conventional X-rays (A, top-left) and changes when a mini-beam collimator is applied (A, top-right), with high doses depicted in red and low doses in blue. Particle beam distribution in tissue (A, bottom-left) and changes when a mini-beam collimator is applied (A, bottom-right). Mini-beam pattern at skin level highlighting important parameters such as FWHM, ctc, peak and valley doses (B, top), and mini-beam pattern at tumor level for particle MBRT (B, bottom).

X-rays, where such technology is also not feasible. Hence, mini-beam collimators emerge as the preferred choice for these modalities. Nevertheless, most available mini-beam collimators are rigid and non-modular, requiring costly wire eroding for manufacturing. Consequently, there is a growing demand for a more versatile mini-beam collimator that facilitates easy and cost-effective adaptation to various experimental setups.

1.4 Combination of CIRT and MBRT

Dilmanian et al. (2015) initially investigated the combination of CIRT and MBRT, referred to as carbon ion mini-beam radiation therapy (iMBRT). This study on rabbit brains demonstrated no cognitive damage following a single dose of 40 Gy iMBRT treatment. MRI and histological examinations conducted six months post-irradiation indicated the potential for healthy tissue sparing (Dilmanian et al. 2015). Other than that, there are not many *in vivo* studies but publications focussed on the characterization and dosimetry of iMBRT. Martínez-Rovira et al. (2017) demonstrated that iMBRT was feasible with a mini-beam collimator producing a mini-beam pattern with 700 μm FWHM peak size and 3200 μm ctc (Martinez-Rovira et al. 2017). Dependence of the PVDR with depth was observed, with a significant PVDR decrease over a depth of 80 mm from 60 to 10 (Martinez-Rovira et al. 2017). Similar findings were demonstrated by experimental studies and simulations revealing a decreased PVDR over depth for different ctcs (Gonzalez et al. 2017, Volz et al. 2023). The simulations also suggest that the valley region mainly comprises scattered primary particles, indicating a comparable LET in both the peak and the valley (Gonzalez et al. 2017). While some studies on iMBRT have been conducted, their number remains limited and largely restricted to either the physical characterization of the beams or biological experiments focused solely on the cranial region of animal models. Thus, future research efforts to evaluate this technique's clinical potential, particularly in human-sized conditions, will provide insights into the feasibility of translating iMBRT to patients.

1.5 Organ motion impact on radiotherapy

When considering radiotherapy treatment for humans, the motion of the internal anatomical structures plays a crucial role, making the treatment region a moving target (Bert and Durante 2011, Brandner et al. 2017). Organ motion manifests in various forms, including breathing-induced motion and bowel motion. Each type of motion presents unique challenges for radiotherapy, with differing susceptibility to errors in the dose delivery. Breathing-induced motion provides the main challenge for the treatment of thoracic and abdominal tumors, causing significant displacement of the tumor and nearby healthy tissue. Additionally, bowel motion complicates dose delivery for abdominal tumor treatments due to the fluctuation of organ positions

and the introduction of gases in the intestine (Li et al. 2020).

The breathing-induced motion diminishes the effectiveness of irradiation in treating moving tumors, particularly in particle therapy due to the precise positioning of the Bragg peak and its sensitivity to organ position changes (Kalantzopoulos et al. 2020, Lebbink et al. 2022). If the mass density distribution of the patient changes from the one used for the treatment plan to the one at the actual moment of the beam delivery, the ranges of the charged particles will be altered, modifying the planned dose distribution. Thus, due to the breathing-induced motion, blurring of the dose distribution can appear, leading to significant discrepancies in the applied dose compared to the planned dose (Kim et al. 2020). Furthermore, bowel motion can influence the dose distribution in the tumor and the OARs. Kumagai et al. (2009) demonstrated that bowel gas motion during pancreatic cancer treatment with carbon ion caused dosimetric variations, leading to either over- or underdosing of the tumor and overdosage of OARs such as the spinal cord and the duodenum (Kumagai et al. 2009). Therefore, it is crucial to optimize beam arrangements such that the interference with the bowel is minimized (Narita et al. 2021).

Preclinical testing of MBRT and iMBRT has so far predominantly focused on cranial anatomical regions of animal models (Dilmanian et al. 2002, Kundapur et al. 2022). This narrow focus has resulted in a limited understanding of how to address moving volumes in humans if treated with SFRT, especially concerning abdominal organs such as the pancreas.

The mini-beam effect depends on the application of a sharp and well-distinguishable mini-beam pattern with high peak doses and low valley doses. Breathing-induced motion, however, can potentially reduce the mini-beam effect due to the blurring of the mini-beam pattern. In the brain, the breathing-induced motion is relatively small in comparison to abdominal organs. While mini-beam irradiation of the murine brain was found to have no significant impact due to breathing motion (Bazyar et al. 2017), MRT led to a 50 % reduction in the PVDR (Chtchevov et al. 2013). This implies that the degree of motion effects varies depending on the size of the SFRT structure. For instance, when considering breathing-induced motion in the abdomen, which can be significantly greater than that observed in the brain, even with grid therapy, employing beam sizes as large as 10 mm, it has been demonstrated that accounting for the motion of abdominal tumors in humans becomes necessary (Naqvi et al. 2008). Given the susceptibility of mini-beam irradiation to breathing-induced motion, it is crucial to conduct further analysis of the impact of breathing-induced motion on the mini-beam pattern.

1.6 Phantoms for radiotherapy

To characterize the dose delivery during radiotherapy treatment without harming the patients, phantoms are typically employed. There is a wide range of different

phantoms available including static and geometrical phantoms as well as more realistic and anthropomorphic phantoms. These are either commercially available phantoms or in-house developed phantoms (Tino et al. 2019, Yadav et al. 2021, Tajik et al. 2022). Of particular interest is the development of anthropomorphic phantoms with features such as organ motion. This capability gains significance in scenarios where tumor and OAR movement needs to be evaluated (Cheung and Sawant 2015, Ehrbach et al. 2019, Colvill et al. 2020).

Phantom classification

The classification of phantoms commonly distinguishes between two main categories: geometrical and anthropomorphic. Geometric phantoms, characterized by simple geometry and mostly uniform distribution within the phantom body, are used for various applications, including assessing image quality and radiation accuracy (Lennie et al. 2021, Kadoya et al. 2021). Geometric phantoms meet the needs of numerous routine quality assurance procedures in the clinic and even some research questions, but they fall short of addressing situations where the effect of radiation impact during motion or adaptative treatment planning needs to be examined. In contrast, anthropomorphic phantoms are realistic models of the human body that mimic anatomical structures, replicating organ characteristics in terms of imaging and radiotherapy modalities (Figure 4 A). Thus, the demand for more realistic anthropomorphic phantoms, encompassing both structural and functional aspects, arises from the continual need to enhance existing and under-development imaging and radiation methodologies (Medeiros Oliveira Ramos 2017).

Commercially available phantoms

One commercially available phantom is the motion management phantom offered by the company CIRS/SunNuclear (Figure 4 B)¹. This phantom replicates the size of the human abdomen and features imaging contrast suitable for computer tomography (CT) scans. Within the phantom, a moving cylinder can be placed to simulate tumor motion. However, the shape of the organs and coordinated motion of several organs can not be simulated. Another commercially available phantom from the same company is the ZEUS: MRgRT motion management quality assurance phantom, which can be employed in magnetic resonance imaging (MRI) including anthropomorphic organs such as the liver and the spine ². Nonetheless, also in this phantom, only a rod can be moved within the phantom.

¹<https://www.sunnuclear.com/products/motion-management-phantoms>, accessed on 26 April 2024.

²<https://www.sunnuclear.com/products/zeus-mrgrt-motion-management-qa-phantom>, accessed on 01 May 2024.

In-house developed phantoms

There have also been efforts to develop anthropomorphic phantoms tailored to address specific research questions. For example, the MRgRT dynamic lung motion thorax anthropomorphic quality assurance phantom was developed (Figure 4 C) (Steinmann et al. 2019). It facilitates lung motion via a pneumatic system during both imaging and treatment, enabling the implementation of MRI workflows and the development of new methods to address motion uncertainties. Another in-house developed phantom is an anthropomorphic phantom with a deformable lung and liver (Figure 4 D) (Colvill et al. 2020). It allows for imaging of simultaneous lung and liver motion, representing an improvement compared to the phantoms where a single cylinder moves inside the phantom. Similarly, an anthropomorphic abdominal phantom including the liver and kidneys with breathing motion capability has been developed, featuring human equivalent tissue contrast in MRI and CT, enabling end-to-end tests in radiotherapy (Weidner et al. 2022). In many cases, the in-house phantom development was assisted by the advances in 3D printing technology (Cloonan et al. 2014, Filippou and Tsoumpas 2018, Okkalidis 2022). Nonetheless, these in-house phantoms have only been recommended or used for linear accelerators (Linacs) and tomotherapy so far and not for particle therapy.

Phantoms for CIRT

The in-house developed Advanced Radiation DOSimetry (ARDOS) phantom represents an advancement in radiation dosimetry as it can be used to measure the dose during ion beam therapy for a lung tumor (Figure 4 E) (Kostiukhina et al. 2017, Kostiukhina et al. 2020, Lebbink et al. 2022). The phantom's motion involves independent movements of the chest wall with the lungs, the rib cage and the tumor insert cylinder with translational and rotational motions. The dose in the tumor can be measured with different dosimeters including thermoluminescent detectors (TLDs), radiochromic films and ionization chambers (ICs) (Kostiukhina et al. 2017). However, an anthropomorphic abdomen phantom with motion capability for CIRT that can measure the dose in different organs simultaneously has not been developed yet.

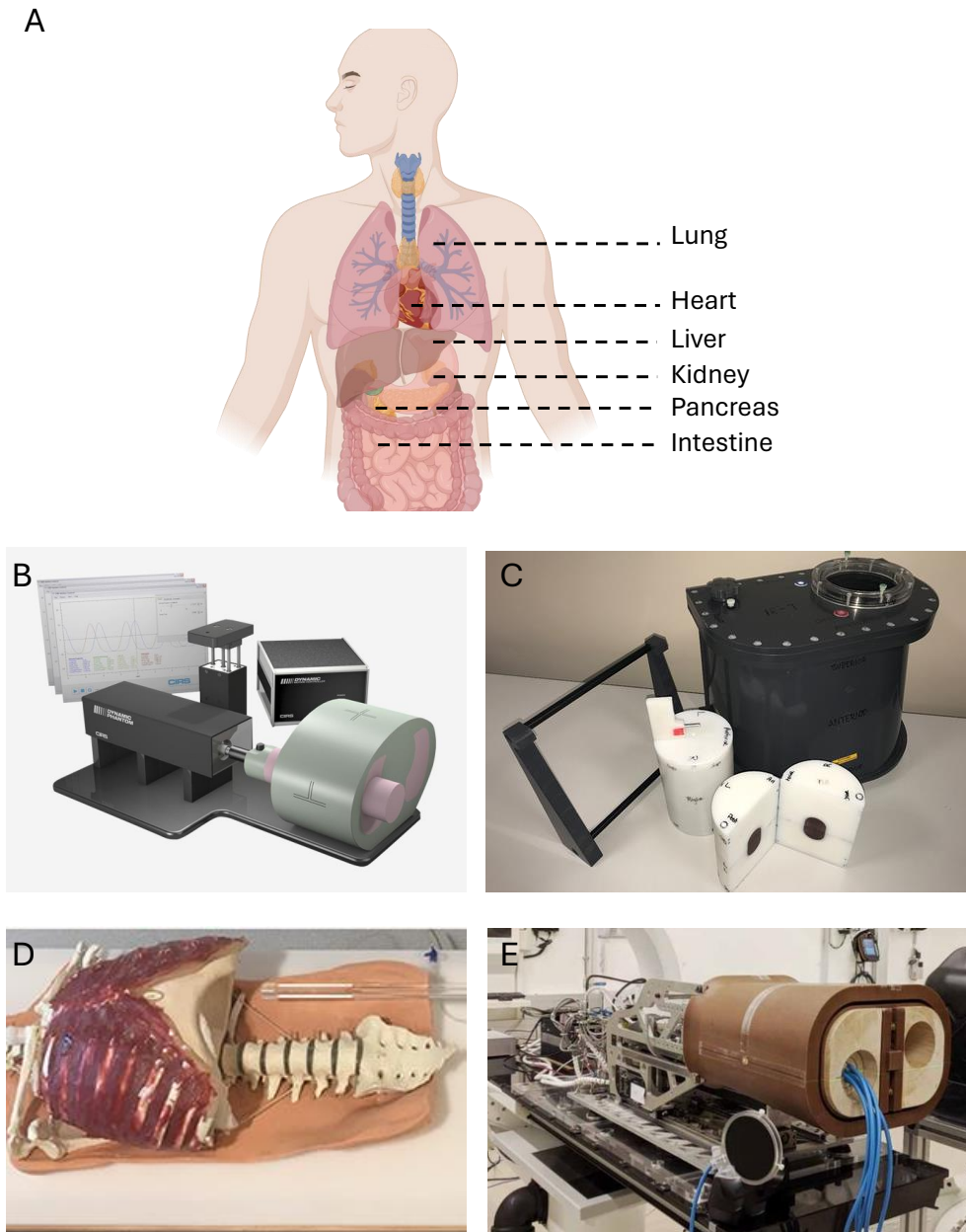


Figure 4: Anatomy of a human body serving as the model for anthropomorphic phantoms (Created with biorender) (A). Commercially available motion management phantom from CIRS/SunNuclear (B). Abdomen phantom for MRgRT (Steinmann et al. 2019) (C). Anthropomorphic, deformable lung phantom (Colvill et al. 2020) (D). ARDOS phantom for ion beam therapy using IC for dose measurements (E).

1.7 Goal of this thesis

The general goal of this thesis is to investigate the impact of organ motion on dose distribution during carbon ion mini-beam radiotherapy for pancreatic cancer using an anthropomorphic phantom. To reach this goal, three specific aims are set:

1. The first specific aim is the development and application of an anthropomorphic Pancreas Phantom for Ion beam Therapy (PPIeT) that integrates respiratory and gastrointestinal motion dynamics for precise dose measurements. By replicating tissue properties and organ motion characteristics observed in patients, PPIeT should enable accurate motion simulation of the pancreas and its OARs to measure the dose during carbon ion radiotherapy at the target and in the OARs.
2. The second specific aim is the development of a novel, adaptable mini-beam collimator designed for pre-clinical dosimetry and *in vitro* studies. To facilitate spatially fractionated dose delivery tailored to specific experimental setups the mini-beam collimator should offer flexibility in adjusting dosimetric parameters including FWHM, etc and PVDR.
3. The last specific aim is to evaluate organ motion effects in carbon ion mini-beam therapy. For this, the dose at the target in the pancreas and OARs of PPIeT should be simultaneously measured for different breathing-induced organ motions comparable to those of humans.

Investigating the effects of motion across various organs, including both target and OARs, would help to advance the understanding of carbon ion mini-beam dose distributions. As an ultimate goal, this research seeks to contribute to a comprehensive analysis of the dose uncertainties due to organ motion, leading to improved outcomes in the radiotherapy treatments delivered to pancreatic cancer patients.

2. Publications for cumulative thesis

In this thesis, breathing-induced motion effects during CIRT and iMBRT were investigated for pancreatic cancer. In this chapter, the three peer-reviewed papers that comprise the cumulative thesis are framed in the overall context of iMBRT for pancreatic cancer. A graphical summary is depicted in Figure 5, presenting an overview of the publications and their connections. The three publications are from here on labeled as **Paper I**, **Paper II** and **Paper III**. The full text of each publication is added in this chapter. Additionally, the published supplementary material of each paper is added in the **Appendix**.

Paper I: Christina Stengl, Kathrin Panow, Eric Arbes, Iván D. Muñoz, Jeppe B. Christensen, Christian Neelsen, Fabian Dinkel, Artur Weidner, Armin Runz, Wibke Johnen, Jakob Liermann, Gernot Echner, José Vedelago, Oliver Jäkel (2023). A phantom to simulate organ motion and its effect on dose distribution in carbon ion therapy for pancreatic cancer. *Physics in Medicine & Biology*, 68(24), 245013. DOI: 10.1088/1361-6560/ad0902
Journal impact factor: 3.5.

Paper II: Christina Stengl, Eric Arbes, Long-Yang Jan Thai, Gernot Echner, José Vedelago, Jeannette Jansen, Oliver Jäkel, Joao Seco (2023). Development and characterization of a versatile mini-beam collimator for pre-clinical photon beam irradiation. *Medical Physics*, 50(8), 5222-5237. DOI: 10.1002/mp.16432
Journal impact factor: 3.8.

Paper III: Christina Stengl, Ivan D. Munoz, Eric Arbes, Evelyn Rauth, Jeppe B. Christensen, José Vedelago, Armin Runz, Oliver Jäkel, Joao Seco (2024). Dosimetric study for breathing-induced motion effects in an abdominal pancreas phantom for carbon ion mini-beam radiotherapy. *Medical Physics*. DOI: 10.1002/mp.17077
Journal impact factor: 3.8.

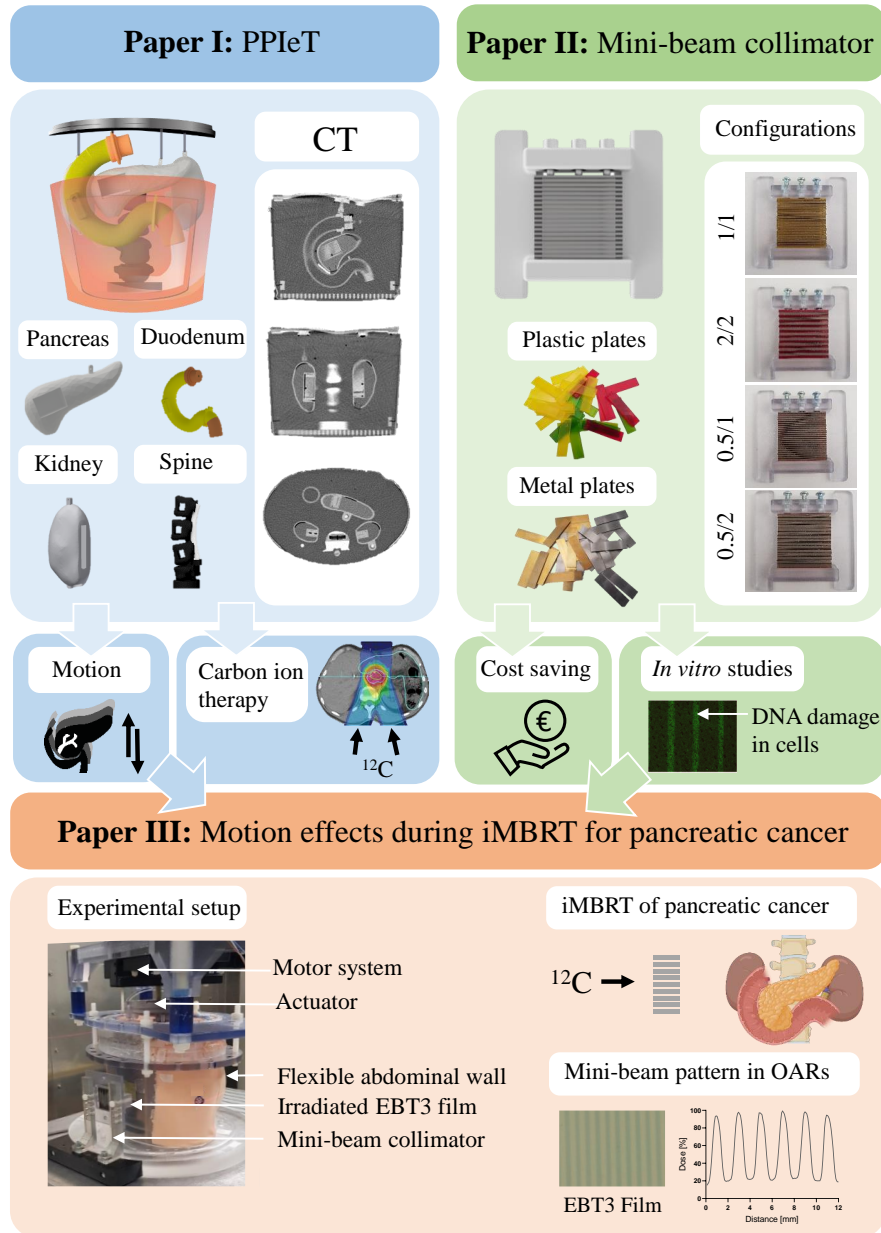


Figure 5: Graphical summary and connection between **Paper I**, **Paper II** and **Paper III** constituting this cumulative thesis.

2.1 Paper I

A phantom to simulate organ motion and its effect on dose distribution in carbon ion therapy for pancreatic cancer

Authors: Christina Stengl*, Kathrin Panow, Eric Arbes, Iván D. Muñoz, Jeppe B. Christensen, Christian Neelsen, Fabian Dinkel, Artur Weidner, Armin Runz, Wibke Johnen, Jakob Liermann, Gernot Echner, José Vedelago, Oliver Jäkel.

*Corresponding author.

Journal reference: Phys. Med. Biol. 2023, 68, 245013

DOI: 10.1088/1361-6560/ad0902

Journal Impact Factor: 3.5

Source: https://iopscience.iop.org/journal/0031-9155/page/About_the_journal#metrics, accessed on 24 May 2024.



PAPER

A phantom to simulate organ motion and its effect on dose distribution in carbon ion therapy for pancreatic cancer

OPEN ACCESS

RECEIVED
27 June 2023REVISED
20 October 2023ACCEPTED FOR PUBLICATION
2 November 2023PUBLISHED
11 December 2023

Original content from this work may be used under the terms of the [Creative Commons Attribution 4.0 licence](https://creativecommons.org/licenses/by/4.0/).

Any further distribution of this work must maintain attribution to the author(s) and the title of the work, journal citation and DOI.



Christina Stengl^{1,2,3,*}, Kathrin Panow^{2,3}, Eric Arbes^{4,5}, Iván D Muñoz^{2,3,5}, Jeppe B Christensen⁶, Christian Neelsen^{7,8,9}, Fabian Dinkel^{2,3}, Artur Weidner^{1,2,3}, Armin Runz^{2,3}, Wibke Johnen^{2,3}, Jakob Liermann^{3,10,11,12}, Gernot Echner^{2,3}, José Vedelago^{2,3,10} and Oliver Jäkel^{2,3,11}

¹ Medical Faculty Heidelberg, Heidelberg University, Im Neuenheimer Feld 672, Heidelberg D-69120, Germany

² Division of Medical Physics in Radiation Oncology, German Cancer Research Center (DKFZ), Im Neuenheimer Feld 280, Heidelberg D-69120, Germany

³ Heidelberg Institute for Radiation Oncology (HIRO), National Center for Radiation Research in Oncology (NCRO), Heidelberg, Germany

⁴ Biomedical Physics in Radiation Oncology, German Cancer Research Center (DKFZ), Im Neuenheimer Feld 280, Heidelberg D-69120, Germany

⁵ Department for Physics and Astronomy, Heidelberg University, Im Neuenheimer Feld 226, Heidelberg D-69120, Germany

⁶ Department of Radiation Safety and Security, Paul Scherrer Institute (PSI), Forschungsstrasse 111, Villigen PSI 5232, Switzerland

⁷ Department of Radiology, German Cancer Research Center (DKFZ), Im Neuenheimer Feld 280, Heidelberg D-69120, Germany

⁸ Department of Nuclear Medicine, German Cancer Research Center (DKFZ), Im Neuenheimer Feld 280, Heidelberg D-69120, Germany

⁹ Department of Radiology, Charité—Universitätsmedizin Berlin, Charitéplatz 1, Berlin D-10117, Germany

¹⁰ Department of Radiation Oncology, Heidelberg University Hospital (UKHD), Im Neuenheimer Feld 400, Heidelberg D-69120, Germany

¹¹ Heidelberg Ion-Beam Therapy Center (HIT), Department of Radiation Oncology, Heidelberg University Hospital (UKHD), Im Neuenheimer Feld 450, Heidelberg D-69120, Germany

¹² National Center for Tumor Diseases (NCT), Im Neuenheimer Feld 460, D-69120 Heidelberg, Germany

* Author to whom any correspondence should be addressed.

E-mail: christina.stengl@dkfz.de

Keywords: anthropomorphic phantom, 3D printing, breathing motion, carbon ion radiotherapy

Supplementary material for this article is available [online](#)

Abstract

Objective. Carbon ion radiotherapy is a promising radiation technique for malignancies like pancreatic cancer. However, organs' motion imposes challenges for achieving homogeneous dose delivery. In this study, an anthropomorphic Pancreas Phantom for Ion-beam Therapy (PPIeT) was developed to simulate breathing and gastrointestinal motion during radiotherapy. **Approach.** The developed phantom contains a pancreas, two kidneys, a duodenum, a spine and a spinal cord. The shell of the organs was 3D printed and filled with agarose-based mixtures. Hounsfield Units (HU) of PPIeT's organs were measured by CT. The pancreas motion amplitude in cranial-caudal (CC) direction was evaluated from patients' 4D CT data. Motions within the obtained range were simulated and analyzed in PPIeT using MRI. Additionally, GI motion was mimicked by changing the volume of the duodenum and quantified by MRI. A patient-like treatment plan was calculated for carbon ions, and the phantom was irradiated in a static and moving condition. Dose measurements in the organs were performed using an ionization chamber and dosimetric films. **Main results.** PPIeT presented tissue equivalent HU and reproducible breathing-induced CC displacements of the pancreas between (3.98 ± 0.36) mm and a maximum of (18.19 ± 0.44) mm. The observed maximum change in distance of (14.28 ± 0.12) mm between pancreas and duodenum was consistent with findings in patients. Carbon ion irradiation revealed homogenous coverage of the virtual tumor at the pancreas in static condition with a 1% deviation from the treatment plan. Instead, the dose delivery during motion with the maximum amplitude yielded an underdosage of 21% at the target and an increased uncertainty by two orders of magnitude. **Significance.** A dedicated phantom was designed and developed for breathing motion assessment of dose deposition during carbon ion radiotherapy. PPIeT is a unique tool for dose verification in the pancreas and its organs at risk during end-to-end tests.

1. Introduction

Pancreatic cancer is one of the deadliest cancers worldwide and it progresses aggressively with a five-year survival rate of 2%–9% (McGuigan *et al* 2018, Rawla *et al* 2019, Michl *et al* 2021). Its treatment options are scarce, and the best potential curative treatment is complete resection (Doi *et al* 2008). However, 80% of pancreatic cancer patients are diagnosed in a locally advanced or metastatic state, suffering from unresectable cancer. In non-metastasized unresectable cases or as a neoadjuvant therapy concept, radiotherapy can improve local tumor control (Chang *et al* 2009, Mahadevan *et al* 2010, Yovino *et al* 2011, Hammel *et al* 2016, Versteijne *et al* 2022). Nevertheless, factors such as motion induced by breathing can lead to an inaccurate dose delivery during radiotherapy, increasing the potential exposure of the organs at risk (OARs). In pancreatic cancer treatment, the main OARs are the kidneys, the duodenum and the spinal cord (Hassanzadeh *et al* 2021, Liermann *et al* 2021).

Among different radiation techniques, pancreatic cancer patients presented promising results when treated with carbon ions (Kawashiro *et al* 2018). A favorable outcome with a 47% overall survival rate after 2 years was shown, compared to 36% when using intensity-modulated radiation therapy with high-energy x-rays (Krishnan *et al* 2016). Following these results, multiple prospective clinical trials testing carbon ion radiotherapy in pancreatic cancer are currently being conducted (Vitolo *et al* 2019, Liermann *et al* 2022). Nevertheless, inconsistencies between planned and delivered doses in carbon ion radiotherapy can be large due to variations of depth-dose distribution, even when considering small spatial displacements of the target (Fontana *et al* 2016). Additionally, organ motion can lead to underdosage of the target volume and over-dosage of the OARs (Phillips *et al* 1992, Bert *et al* 2008).

The pancreatic motion is highly variable, where values from 1.0 mm up to 27.3 mm in the craniocaudal (CC) direction were found (Bhasin *et al* 2006, Knybel *et al* 2014, Dolde *et al* 2019a, Jing *et al* 2021). Although motion management strategies have improved pancreatic treatment outcomes, these often impose unease on the patient by the obligation of breath holding or wearing a corset (Dolde *et al* 2019a). Additionally, gastrointestinal (GI) motion is a challenge during carbon ion radiotherapy since it causes internal anatomic variation during dose delivery. In fact, peristalsis and gas accumulation make it difficult to deliver a homogenous dose to the tumor while sparing the bowel (Kumagai *et al* 2009). Previous studies reported relative motion differences between the pancreas and the duodenum from 13.0 up to 18.5 mm (Mostafaei *et al* 2018).

The use of phantoms in radiotherapy enables dose measurements by providing quality assurance (QA) procedures and allowing for the testing of new treatment scenarios without harming patients. Most of these phantoms have geometrical shapes that do not resemble the human body while anthropomorphic phantoms enable end-to-end tests in a more human-like environment (Tajik *et al* 2022, Vedelago *et al* 2022). In the last years, the development of anthropomorphic phantoms increased continuously, and specialized phantoms have gained significant attention due to their ability to simulate human-like characteristics, particularly in terms of breathing motion. This capability becomes especially relevant when considering scenarios involving the movement of tumors and OARs (Cheung and Sawant 2015, Kim *et al* 2016, Mann *et al* 2017, Ehrbar *et al* 2019). Recently, the development of a phantom for liver treatment made it possible to combine breathing motion of different organs with human equivalent CT and MRI contrast to perform end-to-end studies in MR-Linacs (Weidner *et al* 2022). Notably, there is a growing emphasis on compatibility with MRI systems, leading to the design of phantoms tailored for optimal performance within these environments. Other authors presented a Magnetic Resonance Image-Guided Radiotherapy dynamic lung motion thorax anthropomorphic QA phantom (Steinmann *et al* 2019) as well as an anthropomorphic phantom developed for deformable lung and liver studies, which (Colvill *et al* 2020) have tackled the increasing need for MRI-compatible phantoms (Colvill *et al* 2020). One other phantom to be named is the Advanced Radiation DOSimetry phantom (ARDOS) which incorporates a moving rigid ribcage and can be used to measure dose during ion beam therapy (Kostiukhina *et al* 2017, Kostiukhina *et al* 2020, Lebbink *et al* 2022). Additionally, an anthropomorphic thorax breathing phantom was developed specifically for pencil beam scanning proton therapy (Perrin *et al* 2017).

The present study aims to develop a Pancreas Phantom for Ion-beam Therapy (PPIeT), in which the pancreas is the target organ, while the duodenum, kidneys, spine, and spinal cord serve as OARs. Breathing-induced organ motion within PPIeT was analyzed for different motion inputs with increasing amplitudes. In addition, the influence of the tested motion on dose distribution within the organs in carbon ion therapy was explored. Thanks to the designed features, PPIeT could be used to conduct thorough end-to-end tests for upcoming pancreatic cancer treatment with carbon ions.

2. Materials and methods

2.1. Phantom design

Based on the development of a phantom for liver treatment (Weidner *et al* 2022), PPIeT was constructed out of two 5 l cylindrical polypropylene containers, with a height of 26.0 cm, a wall thickness of 2 mm and a transversal ellipse shape with 29.0 cm major axis and 21.0 cm minor axis. These two containers were interlocked and had a frontal cut-out of $(24.0 \times 10.5) \text{ cm}^2$ for a flexible abdominal wall. This area was covered with a 3 mm thick TFC silicone caoutchouc type 6 layer with a shore of 22 (Troll Factory Rainer Habekost e.K., Germany), and clamped between the two containers. The bottom of the inner container was removed, yielding a cavity with a total volume of 6.5 l, which was filled with a 0.25% w/w superabsorber-water mixture (Schauch, Germany). The top part was covered with a diaphragm made from TFC silicone and attached to the lid with 23 screws (figure 1). The circumference of the phantom is 75 cm, in agreement with an average woman's body.

2.2. Design and construction of the organs

The organ models were designed with anthropomorphic shapes using Inventor 2018 (Autodesk, USA) and Meshmixer (Autodesk, USA). A total of five organs were included in PPIeT, namely the pancreas, two kidneys, flexible duodenum and spine with a spinal cord. The pancreas and kidneys consist of a hollowed structure with an outer shell of 3 mm thickness 3D printed using VeroClear (Stratasys, Israel, 3D printer Stratasys J55). In each of the outer shells a cavity was designed to fit the 3D printed detector inserts. The dimensions and volume of the organs (table 1) correspond to those of humans (Brant 2006, Cheong *et al* 2007). Figures 1(A)–(D) illustrate PPIeT and its organs.

The pancreas and kidney shells (figures 1(E), (F)) were filled with a mixture made from agarose, nickel-diethylene triamine pentaacetic acid (NiDTPA) and potassium chloride (KCl) to mimic human tissue within different imaging techniques and in terms of the stopping power ratio (SPR) (Elter *et al* 2021). Briefly, agarose, NiDTPA, KCl, and water were mixed according to the compositions of supplementary table 1 and heated up to 80 °C. Agarose was degassed using a desiccator to 150 mbar and the mixture was used to fill the 3D printed organs via openings. Afterward, the holes were closed with a polyethylene plug with a diameter of 12.8 mm (BN 1095, TL-4-128, Bossard, Germany), and cooled down to room temperature. The outer shells were designed such that they could remain sealed containing the agarose mixture inside during the experiments.

For the spine, Diran 410MF07 (Stratasys, Israel, 3D printer Stratasys F370) was used, and one cavity was designed in each of the three vertebrae to fit the 3D printed detector inserts (figure 1(G)). The spinal cord imitation made of VeroClear was fixed to the posterior part of the spine. Elastico (Stratasys, Israel, 3D printer Stratasys J55) with shore 60 served as the flexible material for the duodenum, so its volume can be modified to mimic GI motion. To mimic the human body, the duodenum was designed with a C-shape and positioned around the pancreas' head. The hollow internal cavity of the duodenum is connected to the exterior through a polyurethane tube (Festo, Germany) of 6 mm outer diameter and 1 mm wall thickness, so fluids can be taken in or out at any time (figure 1(H)).

2.3. 3D printing of detector inserts

Pluggable detector inserts were 3D designed to fit each organ. In these detector inserts, EBT3 Gafchromic films (Ashland, USA) or a 0.03 cm^3 PinPoint 31015 ionization chamber (PTW, Germany) can be inserted. Inside the pancreas insert, either the films or the ionization chamber could be fitted, while for the kidneys only a film insert was placed on the medial side. In the spine, film inserts were positioned in each of the three segments, complemented by one insert in the spinal cord. The size of each insert is reported in table 2, and an illustration of each organ with its detector inserts is shown in supplementary figure S1.

2.4. Reproducibility of organ positioning inside the phantom

The pancreas, duodenum and kidneys are attached to the diaphragm, whereas the spine is screwed to the bottom of the phantom. When the phantom is opened to exchange detector inserts, the diaphragm lid and the organs attached to it are removed. Thus, for the pancreas and kidneys, guiding pins in the CC direction were fixed to the bottom of the phantom, enabling reproducible re-positioning. Since some of the superabsorber-water mixture can be lost during this process, PPIeT was refilled with the superabsorber-water mixture to weigh 8.50 kg each time after the inserts were changed. Therefore, the phantom was not damaged while changing the inserts or applying motion. The exchange procedure can be done by a trained user in 8 min. The quantification of the organs' re-positioning was done by repetitively opening and closing PPIeT's lid and measuring the deviations from the original position in a 3 T MRI scanner (Biograph mMR, Siemens Healthineers, Germany) using a 3D MRI T1 vibe Dixon sequence with a resolution of $(1 \times 1 \times 1) \text{ cm}^3$.

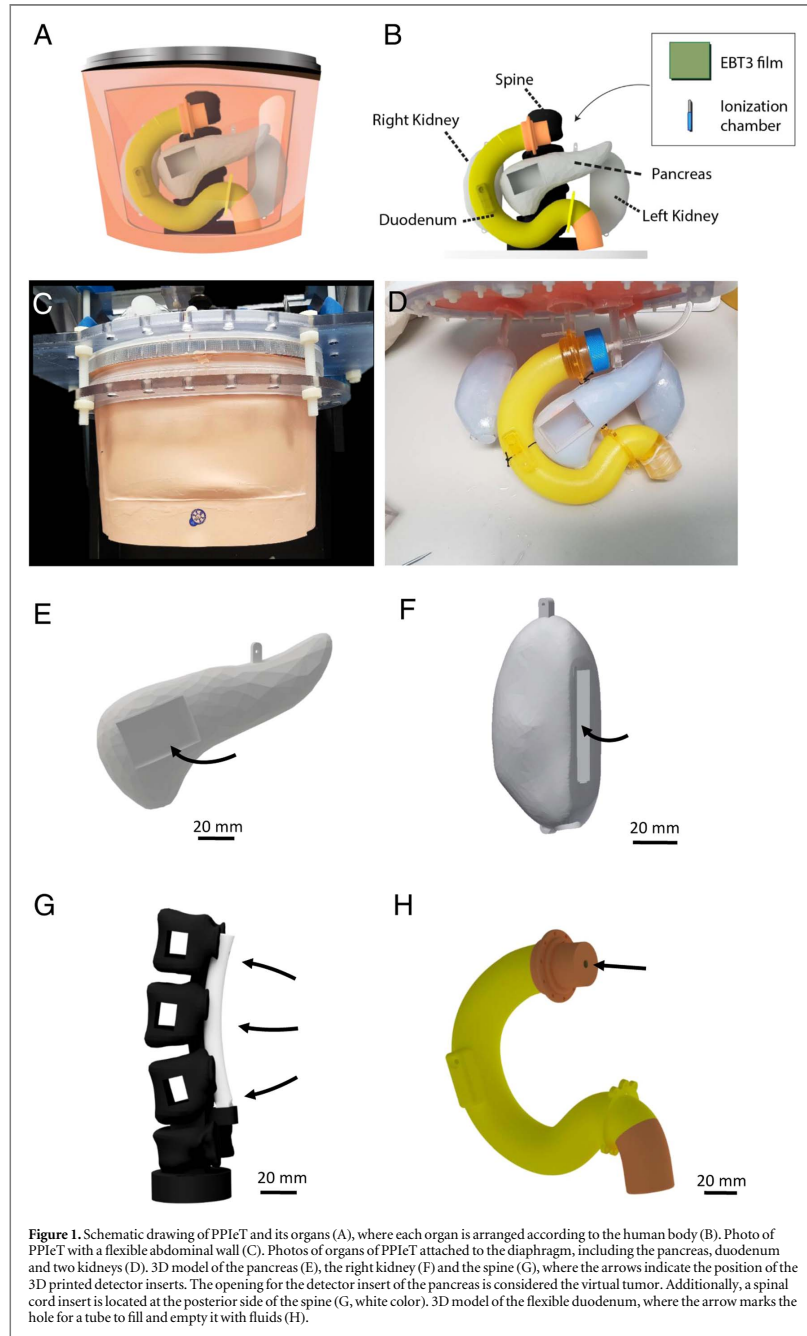


Table 1. Dimensions of organs in PPIeT for height in CC direction, length in right–left (RL) direction, and thickness in anterior–posterior (AP) direction. The given values are the maximum values in each direction since the measures vary due to the anthropomorphic shape.

Organ	Height CC [mm]	Length RL [mm]	Thickness AP [mm]
Pancreas	65	140	35
Kidney	106	64	40
Duodenum	145	138	36
Spine	164	46	44
Spinal cord	102	10	10

Table 2. Size of inserts for each organ along with the film size and number of films fitting in each of them.

	Insert size [mm ³]	Film size [mm ²]	Number of films
Pancreas	25.6 × 37.6 × 23.3	34.0 × 23.0	4
Kidney	20.0 × 50.0 × 8.6	37.0 × 18.0	4
Spine	14.8 × 42.9 × 11.5	29.0 × 11.0	4
Spinal cord	10.0 × 100.6 × 7.0	54.0 × 6.0	1

2.5. Motor-controlled movement: fixed displacement and breathing motion

Breathing motion was simulated with a hydraulic system, including two MRI-compatible double-acting cylinders (PSK Ingenieurgesellschaft mbH, Germany). One of the cylinders was connected to a linear stage, and the other to an actuator positioned cranial from the diaphragm. The stage was moved by a Nema 23 stepper motor (EC Motion GmbH, Germany) and controlled by a PLC CX5020 (Beckhoff, Germany) using TwinCat Version 3 (TcXaeShell Version 15.0.28010.2050 D15.8, Beckhoff, Germany), as illustrated in supplementary figure S2. Therewith, fixed input displacements including 10 mm, 20 mm and 30 mm were applied. Additionally, sinusoidal breathing motions over time t were used as described by Weidner *et al* (2022):

$$Position(t) = A * \sin^2\left(\frac{\pi}{T}t\right),$$

where A is the amplitude, set to 10 mm, 20 mm or 30 mm, and T is the motion period set to 7 s. A video showing the breathing motion in the phantom is given in the supplements (supplementary video S1).

2.6. CT measurements for contrast evaluation

CT measurements were performed with a Definition Flash CT scanner (Siemens Healthineers, Germany). An abdominal scan with 480 mA and 120 kV was used, with a voxel size of $(1 \times 1 \times 1) \text{ mm}^3$. Average Hounsfield units (HU) were retrieved from several slices of each organ using RadiAnt Dicom viewer (Medixant, Version 2022.1.1). The CT numbers of PPIeT's organs were compared to previously published data from humans for the pancreas, kidneys and spine, whereas the CT number of the superabsorber–water mixture was compared to the one of water (Cropp *et al* 2013, Lamba *et al* 2014, Lim *et al* 2014, Irie *et al* 2021).

2.7. MRI measurement for motion analysis

Thanks to its MRI compatibility, the position of the organs in PPIeT during motion was evaluated using a 3 T MRI scanner (Biograph mMR, Siemens Healthineers, Germany) by applying two different sequences. First, a T1 vibe Dixon sequence was applied with a 3D resolution of $(1 \times 1 \times 1) \text{ mm}^3$, a repetition time of 4.22 ms and an echo time of 1.35 ms for organ motion induced by fixed input displacements. Three independent measurements of each amplitude were then compared to 0 mm input displacement, which is the static condition of PPIeT. For this, a free medical image processing platform MITK v2021.10 was used with an affine registration algorithm (Nolden *et al* 2013), with the center of mass of each organ used as the position.

To measure the position of the pancreas and kidneys during breathing, a fast real-time single-slice cine sequence was used for each breathing motion input amplitude. For these acquisitions, the repetition time was 265.35 ms and the echo time was 1.26 ms. 2D images were acquired every 0.315 s with a resolution of $(256 \times 256) \text{ pixels}^2$ for a $(187 \times 187) \text{ mm}^2$ area. Organs were segmented in MITK and the center of mass of each organ over all slices was calculated to retrieve the position over time.

The filling and emptying of the duodenum were done with water and therefore its movement was realized by connecting the tube to a 50 ml syringe. For emptying the duodenum, 25 ml of the water was suctioned out of it, representing a reduction of 8.6% of its total volume, in agreement with other studies (Mudie *et al* 2014, Waal *et al* 2020). In both states, full (control) and empty, measurements with a 3 T MRI scanner (Biograph mMR, Siemens Healthineers, Germany) were conducted using a T1 vibe Dixon sequence with a resolution of $(1 \times 1 \times 1) \text{ mm}^3$ to measure the duodenum shape as its distance to the pancreas. To assess reproducibility, the filling and emptying procedure was repeated three times and parameters were compared with a two-tailed t-test.

2.8. Human pancreas motion analysis from patient data

For analysis of the pancreas motion in CC direction, 4D CT data from 23 patients from Heidelberg University Hospital (Heidelberg, Germany) were retrospectively analyzed. The pancreas was segmented by a radiology expert with MITK and registered using the same methodology used for the phantom. This study was performed in accordance with the ethical standards of the institutional and national research committee, along with the 1964 Helsinki Declaration and its later amendments. This study was approved by the ethics committee of the Medical Faculty of Heidelberg University (Heidelberg, Germany) under No. S-688/2020.

2.9. Carbon ion irradiation

PPIeT was irradiated with carbon ions at the Heidelberg Ion-Beam Therapy Center (HIT; Heidelberg, Germany). A treatment plan was calculated using RayStation (Version 11B (12.0.0.932), RaySearch Laboratories, USA) with the dose calculation engine Pencil beam (Version 4.4) for the virtual tumor in the pancreas head as target. In the treatment plan, the dose grid was set to 2 mm isotropically, the spot spacing was 3.6 mm hexagonal and the energy layer spacing was 3.1 mm. As usually done for patients, two beams at angles 250° and 290° were used. A relative biologic effectiveness (RBE)-weighted dose of 4 Gy (RBE) was planned at the target, calculated with the Local effect model 1. Constraints of a maximum of 3 Gy (RBE) were set for the duodenum, spinal cord and kidneys as done in clinics (Liermann *et al* 2022). During irradiation, static conditions and 30 mm input amplitude breathing motion were compared, either with the pinpoint chamber in the pancreas or EBT3 films in all organs. In the course of irradiation, the duodenum was in control state and did not change its shape. The collected charge in the ionization chamber for four independent irradiations was corrected by temperature and pressure, multiplied by the detector calibration factor from PTW to get the absorbed dose. Finally, the physical dose was multiplied by the RBE factor, calculated as the mean RBE-weighted dose divided by the mean physical dose within the virtual tumor retrieved from RayStation. Next, control and motion conditions were compared by a two-tailed t-test. The EBT3 films were scanned 24 h after irradiation with an Epson Expression 10000XL (Epson, Japan), using a standardized film scanning procedure (Niroomand-Rad *et al* 2020, Stengl *et al* 2023).

3. Results

3.1. Internal structure of PPIeT

The internal disposition of the organs inside the assembled phantom can be seen in the CT images reported in figures 2(A)–(C), along with the CT numbers for the pancreas (48.4 ± 7.5) HU, kidneys (26.58 ± 6.3) HU, and spine (259 ± 18) HU plotted in figure 2(D). For the kidneys, the mean values of the two kidneys were averaged. The CT numbers of PPIeT's organs present no significant differences compared to human data for the pancreas (54.6 ± 5.8) HU, kidneys (29.5 ± 5.1) HU and spine (203 ± 76) HU. For the superabsorber-water mixture, the measured (2.1 ± 5.8) HU presents no significant difference compared to water with (0 ± 7) HU.

An illustration of the open PPIeT, with the pancreas, duodenum and two kidneys hanging from the diaphragm lid and the spine remaining inside is shown in figure 3(A). The quantification of the organs' repositioning was done by repetitively opening and closing PPIeT's lid and measuring the deviations from the original position. As reported in figure 3(B), the differences in the mean values of the absolute position in the CC direction were less than 1 mm. The measured differences in the positions are in the range of the MR resolution and the segmentation uncertainty.

3.2. PPIeT's organs motion: fixed displacements, breathing and GI motion

Pancreas motion of patients was evaluated revealing a range of 0.11 mm up to 19.84 mm with an average value of (5.7 ± 4.6) mm (figure 4(A)). The induced displacements in PPIeT's pancreas (figure 4(B)) agreed with those of the patients. Linear dependencies from the fixed input displacements were obtained for the pancreas, duodenum and two kidneys in PPIeT (figure 4(C)). The parameters of each linear fit $y = a \cdot x + b$ where x is the fixed input displacement and y is the measured displacement, are depicted in table 3. The linear dependency is supported by the obtained R^2 values higher than 0.99 for all the organs and makes it possible to obtain a desired

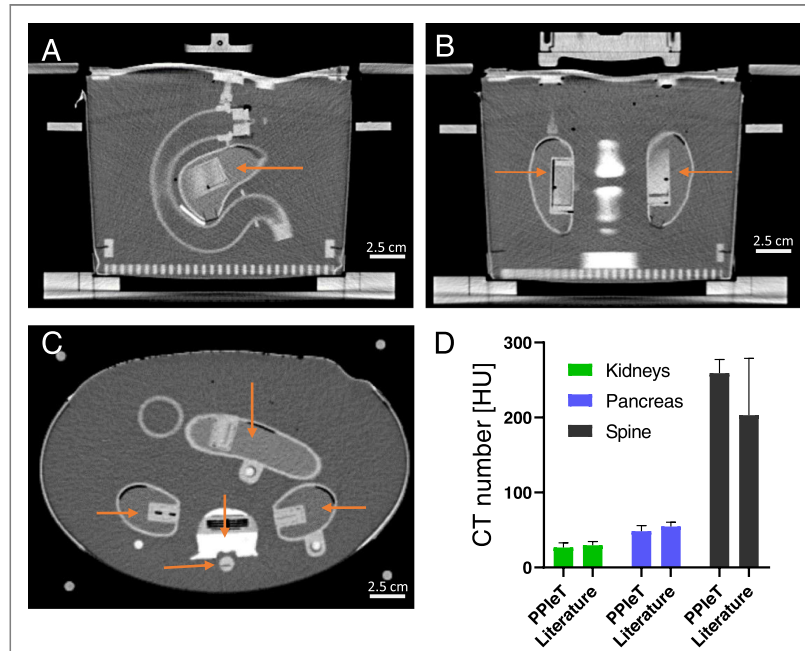


Figure 2. CT images of PPIeT in the coronal plane of the pancreas (A) and kidneys (B). Axial plane with all organs visible (C). The orange arrows indicate the film positions inside the organs in (A), (B) and (C). The measured CT numbers of PPIeT are reported in (D), along with values from literature.

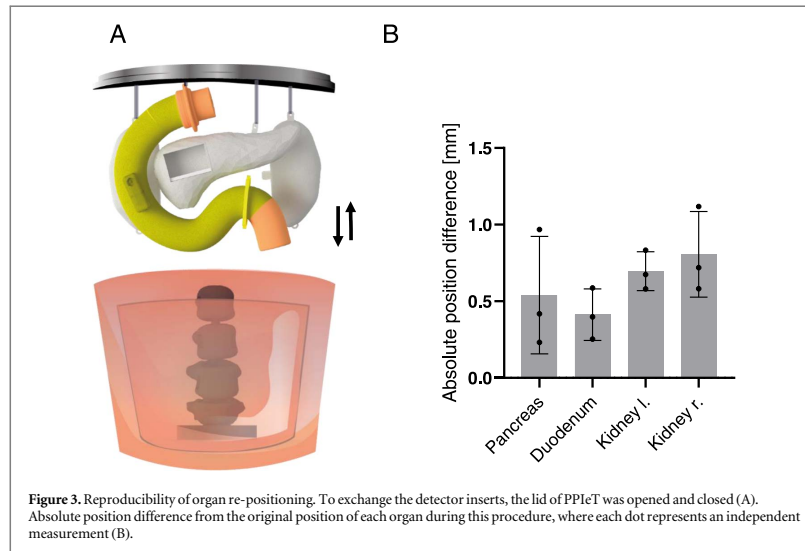


Figure 3. Reproducibility of organ re-positioning. To exchange the detector inserts, the lid of PPIeT was opened and closed (A). Absolute position difference from the original position of each organ during this procedure, where each dot represents an independent measurement (B).

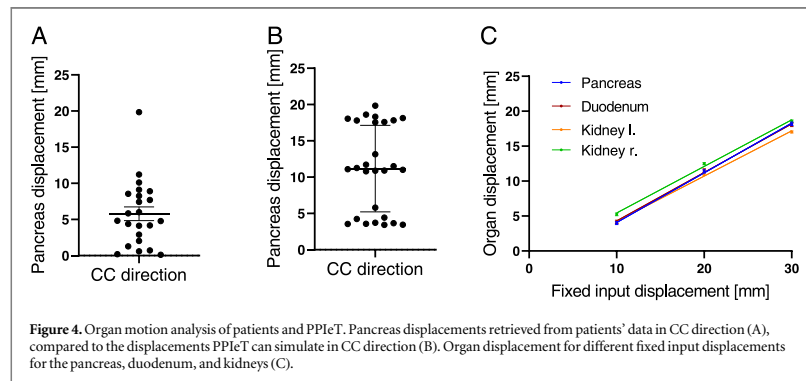


Figure 4. Organ motion analysis of patients and PPIeT. Pancreas displacements retrieved from patients' data in CC direction (A), compared to the displacements PPIeT can simulate in CC direction (B). Organ displacement for different fixed input displacements for the pancreas, duodenum, and kidneys (C).

Table 3. Parameters of the linear fit $y = a * x + b$ for each organ when applying a fixed input displacement, as reported in figure 4(D).

Organ \ parameter	a [mm/mm]	b [mm]	R^2
Pancreas	0.711 ± 0.016	-3.03 ± 0.84	0.996
Duodenum	0.693 ± 0.018	-2.62 ± 0.94	0.995
Left kidney	0.647 ± 0.015	-2.21 ± 0.78	0.996
Right kidney	0.666 ± 0.017	-1.22 ± 0.87	0.995

displacement between (3.98 ± 0.36) mm and (18.19 ± 0.44) mm. The y -intercepts are negative due to a small offset between the actuator and the diaphragm, thus the minimum fixed input amplitude used was 10 mm.

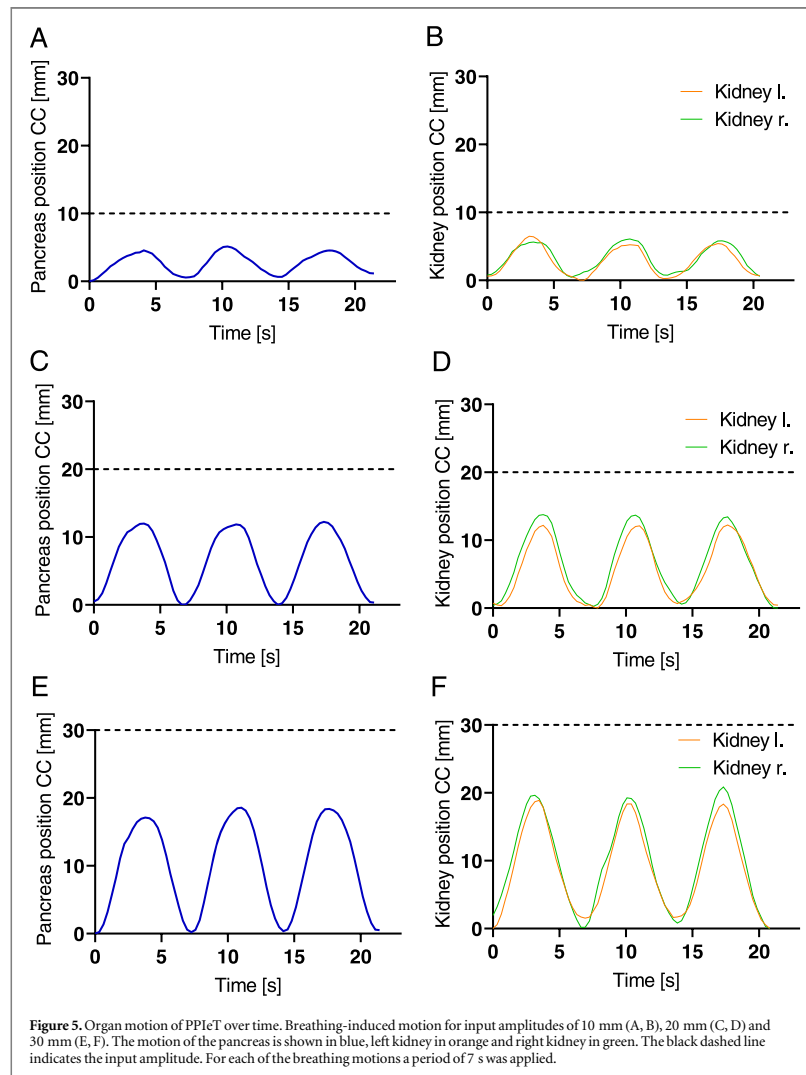
The breathing-induced motion of the pancreas and kidneys is reported in figure 5, where it is observed that the organs follow the sinusoidal shape of the input motion. When increasing the input amplitude, an increase in the organs' amplitudes was found with a mean maximum amplitude of (18.02 ± 0.79) mm. The resulting amplitudes of the breathing motion profiles in the pancreas agree with the fixed displacement amplitudes reported in figure 4(C) with mean differences of 0.8 mm, 0.7 mm and 0.2 mm for input amplitudes of 10 mm, 20 mm and 30 mm, respectively. By averaging the results from the three input amplitudes, the pancreas motion yielded a period of (6.9 ± 0.2) s, in accordance with the input period of 7 s.

To simulate GI motion, the duodenum was filled with water and partially emptied, resulting in a shape change. MR images of PPIeT with the full duodenum, considered as the control condition, and the empty duodenum, are reported in figures 6(A)–(D), respectively (for a zoomed-in region). The distance between the duodenum and pancreas yielded an increase from (1.62 ± 0.20) to (15.91 ± 0.21) mm for the control and empty state, respectively ($p = 0.0001$), as plotted in figure 7(A). For further quantification, the outer shape of the duodenum in the axial plane was modeled by an ellipse. The major and minor axes were quantified, and the obtained axis lengths are reported in figure 7(B). Significant differences were obtained for the major axis ($p = 0.0319$) and the minor axis ($p = 0.0001$), showing the capabilities of PPIeT to mimic GI motion.

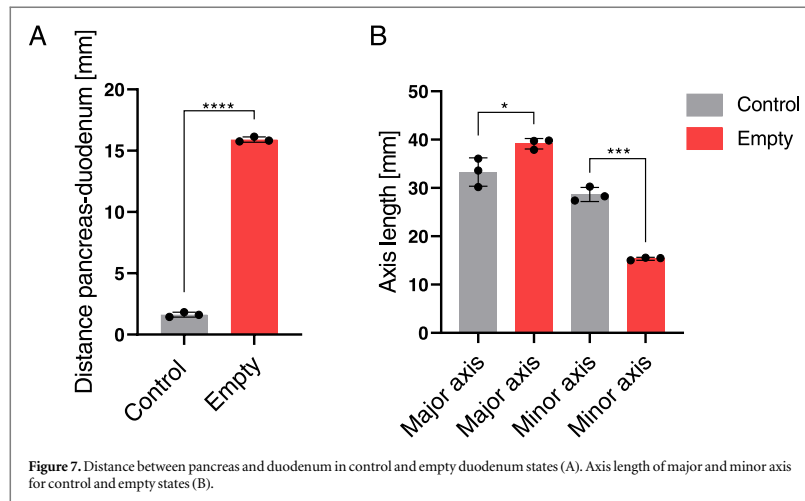
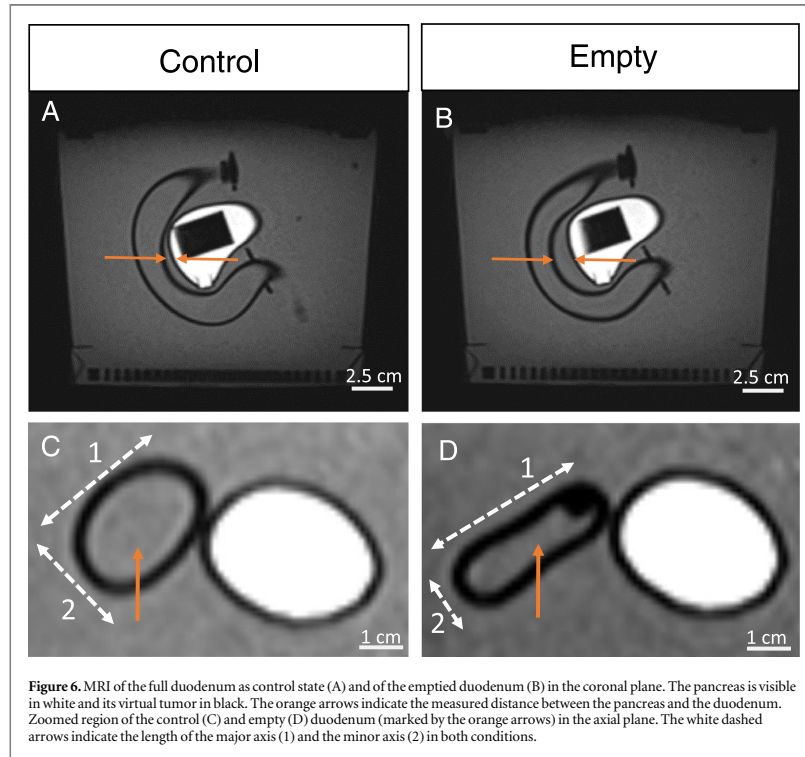
3.3. Dosimetric validation of carbon ion dose delivery

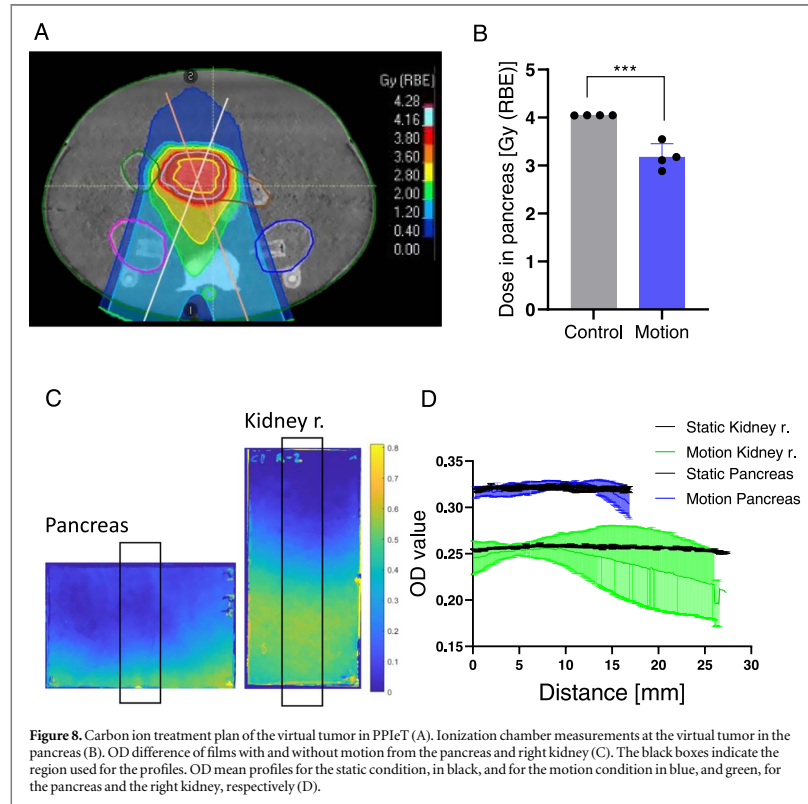
To test the feasibility of an end-to-end test using PPIeT, the phantom was irradiated with carbon ions to treat the virtual tumor located at the pancreas head. The treatment plan consists of two beams at different angles, as shown in the planned RBE-weighted dose distribution in figure 8(A). The similarity of PPIeT's treatment plan compared to two different patients is reported in supplementary figure S3.

First, static irradiation of PPIeT was carried out, yielding a total physical dose of (1.39 ± 0.03) Gy and an RBE-weighted dose of (4.05 ± 0.08) Gy (RBE) in the virtual tumor, for an RBE factor of 2.89. Instead, when breathing motion was applied to PPIeT, lower ionization chamber readings with higher variability were obtained, resulting in a total physical dose of (1.09 ± 0.10) Gy and an RBE-weighted dose of (3.18 ± 0.29) Gy (RBE). A significant difference ($p = 0.0009$) in the mean values was found (figure 8(B), supplementary figure S4(A)), with an increase in the relative uncertainty from less than 0.04% in the static condition to 8.67% during the breathing motion. The physical dose from every single beam is shown in supplementary figure S4(B).



To further quantify this effect with higher spatial resolution, film dosimetry measurements were done in both static and during breathing motion of PPIeT. Two-dimensional differences between films in static and motion conditions are shown in figure 8(C). The mean profiles from three independent measurements are reported in figure 8(D) for the pancreas and right kidney. Supplementary figure S5 reports raw film data, two-dimensional OD differences of films in static and motion conditions, and mean OD profiles for all the organs. As reported in figure 8(D) for the pancreas, films irradiated during static conditions show reproducibility with a relative uncertainty of at most 1.3%. However, films irradiated during breathing motion show inhomogeneous target irradiation with a relative uncertainty of 5.3%. For the right kidney, a maximum relative uncertainty of 19.0% was found, while for the static condition, the maximum relative uncertainty was 1.1%. For the left kidney, a deviation in the mean value of up to 8.4% comparing static to motion conditions was detected. For the non-





moving organs of PPIeT, namely the spine and the spinal cord, films showed mean value deviations lower than 1.5% between static and motion conditions.

4. Discussion

4.1. Phantom setup

PPIeT incorporates anthropomorphic organs of the abdomen that are composed of tissue-equivalent material in terms of their CT contrast. The outer shell of the organs was constructed by 3D printing, which allowed the design and manufacturing of artificial organs with a size and shape resembling human organs. Previous studies have already shown the capability of 3D printing to incorporate customized features in anthropomorphic phantoms (Colvill *et al* 2020, Halloran *et al* 2021). This technique enables personalized phantom adaption and easy prototyping. Furthermore, the combination of diverse materials and printing architectures provides a versatile toolkit for achieving different image contrasts or deformability (Colvill *et al* 2020). For PPIeT, Diran was used as 3D printing material for the spine due to its increased density compared to VeroClear, thus increasing the HU in CT imaging. For the duodenum, a flexible 3D printed material was chosen, making it possible to change duodenal filling independent from breathing motion. So far, the use of flexible 3D printed material for phantoms is scarce. One example is the use of flexible material for artery design (Toepker *et al* 2013, Filippou and Tsoumpas 2018). However, in most studies, 3D printing material was only used for the molds, which were then filled with silicone or similar flexible materials (Hazelaar *et al* 2018, Gillmann *et al* 2021). As shown, when using 3D printing with flexible material, the complex manufacturing steps are streamlined, offering a simplified and more efficient process.

The possibility of detector exchange has already been presented in other anthropomorphic phantoms, and it is an important feature to measure with several detectors since they can have different advantages (Kostiukhina *et al* 2017, Pallotta *et al* 2019). Thanks to the versatile process of 3D printing, different inserts can be easily prototyped for the organs such that a straightforward exchange of dosimeters is possible. For instance, in PPIeT, either an ionization chamber insert or film insert can be positioned in the pancreas, and simultaneously film inserts can be positioned in the OARs. In the future, this innovative design can be directly expanded to other detectors without major efforts.

Besides the usage of the versatile technique of 3D printing, the phantom design also incorporates NiDTPA-KCl mixtures to fill the pancreas and kidneys with tissue-equivalent material. With this approach, CT contrast and SPR values match the ones in humans (Elter *et al* 2021). This method was also used within an anthropomorphic phantom in the publication of Weidner *et al* (2022). Compared to already published anthropomorphic phantoms, PPIeT uses a superabsorber-water mixture as a filling matrix instead of agarose. Thereby, it is possible to avoid drawbacks resulting from structural breaks of the agarose during motion as well as water collection in these lesions. This can lead to changes in the phantom that are not considered in the treatment plan (Weidner *et al* 2022). The superabsorber-water mixture has the advantage that it can be physically displaced without harming its structure. It also enables the exchange of dosimeters without destroying the internal matrix, yielding mean differences in the re-positioning of the organs below the MRI resolution.

4.2. Phantom motion

When dealing with pancreatic cancer, it is important to consider the movement of the pancreas and the OARs because this can lead to differences between the planned and delivered doses. A previous study on patients treated with protons showed the robustness of dose coverage for pancreas motion below 3.7 mm (Knäusl *et al* 2023). Nevertheless, patients' pancreas movement is not restricted to the margin of the so-called small movers but can increase individually up to several cm in the CC direction (Bhasin *et al* 2006, Knybel *et al* 2014, Dolde *et al* 2019a, Jing *et al* 2021). To cover this wide range of pancreatic movement observed in patients, breathing-induced motion from 3.98 to 18.19 mm was studied with PPIeT. Smaller displacements were not studied since their influence on dose delivery is expected to be mostly neglectable (Lebbink *et al* 2022). Since it was possible to linearly correlate the fixed input displacement to the displacement of each organ, any desired organ motion can be achieved. These linear relations made it possible to study the breathing-induced organ motion in PPIeT. Moreover, the lowest amplitude movements achieved in the pancreas and kidneys presented a more precise shape compared to a previous phantom (Weidner *et al* 2022). Based on the obtained results, it is possible to calculate a desired breathing motion amplitude matching the values of an individual patient.

In addition to the breathing motion, it is important to consider the GI motion, since this can significantly change the dose at the duodenum, one critical OAR in pancreatic cancer treatment (Uchinami *et al* 2023). A recent study presented a computational phantom that models GI motion in 4D (Subashi *et al* 2023), but so far and to the best of the authors' knowledge, there is no anthropomorphic phantom that can simulate GI motion for radiotherapy. PPIeT enables mimicking GI motion by changing the volume of the duodenum, making it possible to study the impact of changes in the distance between the pancreas and duodenum in the course of radiotherapy. The quantitative analysis of this distance change in the phantom matched the results found in patients revealing a relative change from 13.0 up to 18.5 mm (Mostafaei *et al* 2018). In the future, PPIeT can also be used to study gas accumulation inside the duodenum as this causes dosimetric variations in carbon ion radiotherapy treatments (Kumagai *et al* 2009).

4.3. Carbon ion treatment of PPIeT

The feasibility of using PPIeT for carbon ion irradiation was tested with a treatment plan equal to that of a patient. Measurements done with the ionization chamber in the pancreas were reproducible within the static condition. A significant reduction in the mean dose value of 21% was observed during breathing-induced motion. The observed difference can have several reasons, one of them being related to the size of the target volume making the ionization chamber partially move out of the beam, especially for the largest input breathing amplitude used. In addition, a larger dispersion in these measurements was obtained, probably caused by dose rate changes, directly influencing the accuracy of the chamber measurements, as reported by Lebbink *et al* (2022) for carbon ion irradiation during motion. Furthermore, the breathing motion in PPIeT was not synchronized with the beam delivery leading to a possible interplay effect between each single beam spot position and the chamber position (Bert *et al* 2008, Bert and Durante 2011, Dolde *et al* 2019b). Additionally, dosimetric films were used in the pancreas and OARs to achieve a high spatial resolution in 2D. Considering that film dosimetry has a limitation related to LET-dependent response (Castriconi *et al* 2017), the films were positioned facing the beam within their organ position to reduce this effect.

Both, ionization chamber and films, were used to respectively achieve 1D or 2D dose estimations within PPIeT. To extend this to 3D, a possibility would be to use dosimetry gel, a technique that was used in an anthropomorphic phantom with a breathing feature (Mann *et al* 2017). However, the irradiation modality used in this study was photons and dosimetry gel presents challenges for carbon ion irradiation due to its LET-dependent response (Maeyama *et al* 2023).

In summary, the presented results point towards the need for motion management techniques during carbon ion irradiation for pancreatic cancer. The performance of PPIeT would make it possible to conduct end-to-end tests accounting for breathing motion effects, like gating.

5. Conclusion

To the best of the authors' knowledge, PPIeT is the first anthropomorphic Pancreas Phantom for Ion-beam Therapy with a breathing and gastrointestinal motion feature for dose QA. PPIeT enables tissue equivalent CT contrast, reproducible positioning of the organs and can simulate the pancreas motion values retrieved from patient data in the range from 4 to 18 mm. The organ motion was achieved for fixed input displacement and sinusoidal breathing motion, following the input period with 99% accuracy. In the gastrointestinal motion study, a mean change of distance between the pancreas and the duodenum of 14 mm was achieved, in accordance with previous patient studies. To assess the influence of the breathing-induced motion in the organs during carbon ion treatment, the developed detector inserts were used. Thereby, an increase of at least one order of magnitude in the dose uncertainty was found during motion conditions compared to static conditions. This is a clinically relevant difference to decide whether carbon ion radiotherapy of pancreatic cancer could be improved by using gating techniques. Overall, PPIeT is a one-of-a-kind tool for dose verifications in the pancreas as well as related organs at risk for precision radiotherapy.

Acknowledgments

We would like to thank Martina Jochim and Marliese Schenk from DKFZ and UKHD for their support during CT measurements. We are also grateful to Beata Koczur, Alexander Neuholz and Stephan Brons from HIT, who created the treatment plans and supported us during the irradiations. Furthermore, we like to thank Steffen Seeber and Carlos Murillo from DKFZ for their support with the hydraulic system. Additionally, CS wants to acknowledge the funding from the Helmholtz graduate school for cancer research of the DKFZ, within their PhD program. IDM acknowledges funding from DAAD (Research Grants-Doctoral Programs in Germany, program number: 57440921).

Data availability statement

The data cannot be made publicly available upon publication because they contain sensitive personal information. The data that support the findings of this study are available upon reasonable request from the authors.

CRediT authorship contribution statement

Christina Stengl: Conceptualization, Methodology, Software, Validation, Formal Analysis, Investigation, Data Curation, Writing—Original Draft, Writing—Review and Editing, Project Administration, Visualization.
Kathrin Panow: Conceptualization, Methodology, Investigation. **Eric Arbes:** Investigation, Data Curation.
Iván D Muñoz: Methodology, Investigation. **Jeppe B Christensen:** Methodology, Investigation. **Christian Neelsen:** Data Curation, Formal Analysis. **Fabian Dinkel:** Methodology, Software. **Artur Weidner:** Conceptualization, Methodology. **Armin Runz:** Methodology, Resources, Funding Acquisition. **Wibke Johnen:** Conceptualization, Methodology. **Jakob Liermann:** Conceptualization, Project Administration. **Gernot Echner:** Methodology, Resources, Funding Acquisition. **José Vedelago:** Conceptualization, Project Administration, Writing—Original Draft, Writing—Review and Editing. **Oliver Jäkel:** Resources, Conceptualization, Project Administration, Funding Acquisition.

ORCID iDs

Christina Stengl  <https://orcid.org/0000-0003-0273-0878>

Eric Arbes  <https://orcid.org/0000-0001-8498-2600>
 Iván D Muñoz  <https://orcid.org/0000-0001-5183-3705>
 Jeppe B Christensen  <https://orcid.org/0000-0002-6894-381X>
 Artur Weidner  <https://orcid.org/0000-0002-9926-4318>
 José Vedelago  <https://orcid.org/0000-0001-5510-9749>
 Oliver Jäkel  <https://orcid.org/0000-0002-6056-9747>

References

- Bert C and Durante M 2011 Motion in radiotherapy: particle therapy *Phys. Med. Biol.* **56** R113–44
- Bert C, Grözinger S O and Rietzel E 2008 Quantification of interplay effects of scanned particle beams and moving targets *Phys. Med. Biol.* **53** 2253–65
- Bhasin D K, Rana S S, Jahagirdar S and Nagi B 2006 Does the pancreas move with respiration? *J. Gastroenterol. Hepatol.* **21** 1424–7
- Castriconi R et al 2017 Dose-response of EBT3 radiochromic films to proton and carbon ion clinical beams *Phys. Med. Biol.* **62** 377–93
- Chang D T et al 2009 Stereotactic radiotherapy for unresectable adenocarcinoma of the pancreas *Cancer* **115** 665–72
- Cheong B, Muthupillai R, Rubin M F and Flamm S D 2007 Normal values for renal length and volume as measured by magnetic resonance imaging *Clin. J. Am. Soc. Nephrol.* **2** 38–45
- Cheung Y and Sawant A 2015 An externally and internally deformable, programmable lung motion phantom *Med. Phys.* **42** 2585–93
- Colvill E et al 2020 Anthropomorphic phantom for deformable lung and liver CT and MR imaging for radiotherapy *Phys. Med. Biol.* **65** 07NT02
- Cropp R J, Sesiija P, Tso D and Thakur Y 2013 Scanner and kVp dependence of measured CT numbers in the ACR CT phantom *J. Appl. Clin. Med. Phys.* **14** 4417
- Doi R et al 2008 Surgery versus radiochemotherapy for resectable locally invasive pancreatic cancer: final results of a randomized multi-institutional trial *Surg. Today* **38** 1021–8
- Dolde K et al 2019a Comparison of pancreatic respiratory motion management with three abdominal corsets for particle radiation therapy: Case study *JACMP* **20** 111–9
- Dolde K et al 2019b 4DMRI-based investigation on the interplay effect for pencil beam scanning proton therapy of pancreatic cancer patients *Radiat. Oncol.* **14** 30
- Ehrbar S et al 2019 ELPHA: dynamically deformable liver phantom for real-time motion-adaptive radiotherapy treatments *Med. Phys.* **46** 839–50
- Elter A et al 2021 Development of phantom materials with independently adjustable CT- and MR-contrast at 0.35, 1.5 and 3 T *Phys. Med. Biol.* **66** 45013
- Filippou V and Tsoumpas C 2018 Recent advances on the development of phantoms using 3D printing for imaging with CT, MRI, PET, SPECT, and ultrasound *Med. Phys.* **45** e740–60
- Fontana G et al 2016 MRI quantification of pancreas motion as a function of patient setup for particle therapy—a preliminary study *JACMP* **17** 60–75
- Gillmann C et al 2021 Technical Note: ADAM PETer—an anthropomorphic, deformable and multimodality pelvis phantom with positron emission tomography extension for radiotherapy *Med. Phys.* **48** 1624–32
- Halloran A, Newhauser W, Chu C and Donahue W 2021 Personalized 3D-printed anthropomorphic phantoms for dosimetry in charged particle fields *Phys. Med. Biol.* **66** 22NT01
- Hammel P et al 2016 Effect of chemoradiotherapy vs chemotherapy on survival in patients with locally advanced pancreatic cancer controlled after 4 months of gemcitabine with or without erlotinib: the LAP07 randomized clinical trial *JAMA* **315** 1844–53
- Hassanzadeh C et al 2021 Ablative five-fraction stereotactic body radiation therapy for inoperable pancreatic cancer using online MR-guided adaptation *Adv. Radiat.* **6** 100506
- Hazelaar C, van Eijnatten M, Dahele M, Wolff J, Forouzanfar T, Slotman B and Verbakel W F A R 2018 Using 3D printing techniques to create an anthropomorphic thorax phantom for medical imaging purposes *Med. Phys.* **45** 92–100
- Irie T Y, Irie T, Espinoza Orias A A, Segami K, Iwasaki N, An H S and Inoue N 2021 Three-dimensional distribution of CT attenuation in the lumbar spine pedicle wall *Sci. Rep.* **11** 1709
- Jing S, Jiang C, Ji X, Qiu X, Li J, Sun X and Zhu X 2021 Study on motion management of pancreatic cancer treated by CyberKnife *Front. Oncol.* **11** 767832
- Kawashiro S et al 2018 Multi-institutional study of carbon-ion radiotherapy for locally advanced pancreatic cancer: japan carbon-ion radiation oncology study group (J-CROS) study 1403 pancreas *IJROBP* **101** 1212–21
- Kim J et al 2016 Development of deformable moving lung phantom to simulate respiratory motion in radiotherapy *Med. Dosim.* **41** 113–7
- Knäusel B, Lebbink F, Fossati P, Engwall E, Georg D and Stock M 2023 Patient breathing motion and delivery specifics influencing the robustness of a proton pancreas irradiation *Cancers* **15** 2550
- Knybel L et al 2014 The analysis of respiration-induced pancreatic tumor motion based on reference measurement *Radiat. Oncol.* **9** 192
- Kostiukhina N et al 2017 Advanced radiation dosimetry phantom (ARDOS): a versatile breathing phantom for 4D radiation therapy and medical imaging *Phys. Med. Biol.* **62** 8136–53
- Kostiukhina N, Palmans H, Stock M, Knopf A, Georg D and Knäusel B 2020 Time-resolved dosimetry for validation of 4D dose calculation in PBS proton therapy *Phys. Med. Biol.* **65** 125015
- Krishnan S et al 2016 Focal radiation therapy dose escalation improves overall survival in locally advanced pancreatic cancer patients receiving induction chemotherapy and consolidative chemoradiation *IJROBP* **94** 755–65
- Kumagai M et al 2009 Impact of intrafractional bowel gas movement on carbon ion beam dose distribution in pancreatic radiotherapy *IJROBP* **73** 1276–81
- Lamba R, McGahan J P, Corwin M T, Li C-S, Tran T, Seibert J A and Boone J M 2014 CT Hounsfield numbers of soft tissues on unenhanced abdominal CT scans: variability between two different manufacturers' MDCT scanners *Am. J. Roentgenol.* **203** 1013–20
- Lebbink F, Stock M, Georg D and Knäusel B 2022 The influence of motion on the delivery accuracy when comparing actively scanned carbon ions versus protons at a synchrotron-based radiotherapy facility *Cancers* **14** 1788
- Liermann J, Ben-Josef E, Syed M, Debus J, Herfarth K and Naumann P 2022 Carbon ion radiotherapy as definitive treatment in locally recurrent pancreatic cancer *Strahlenther. Onkol.* **198** 378–87

- Liermann J, Naumann P, Weykamp F, Hoegen P, Debus J and Herfarth K 2021 Effectiveness of carbon ion radiation in locally advanced pancreatic cancer *Front. Oncol.* **11** 708884
- Lim S et al 2014 Differences in pancreatic volume, fat content, and fat density measured by multidetector-row computed tomography according to the duration of diabetes *Acta Diabetol.* **51** 739–48
- Maeyama T, Mochizuki A, Yoshida K, Fukunishi N, Ishikawa K L and Fukuda S 2023 Radio-fluorogenic nanoclay gel dosimeters with reduced linear energy transfer dependence for carbon-ion beam radiotherapy *Med. Phys.* **50** 1073–85
- Mahadevan A et al 2010 Stereotactic body radiotherapy and gemcitabine for locally advanced pancreatic cancer *IJROBP* **78** 735–42
- Mann P et al 2017 3D dosimetric validation of motion compensation concepts in radiotherapy using an anthropomorphic dynamic lung phantom *Phys. Med. Biol.* **62** 573–95
- McGuigan A, Kelly P, Turkington R C, Jones C, Coleman H G and McCain R S 2018 Pancreatic cancer: a review of clinical diagnosis, epidemiology, treatment and outcomes *World J. Gastroenterol.* **24** 4846–61
- Michl P et al 2021 UEG position paper on pancreatic cancer. Bringing pancreatic cancer to the 21st century: prevent, detect, and treat the disease earlier and better *UEG* **9** 860–71
- Mostafaie F et al 2018 Variations of MRI-assessed peristaltic motions during radiation therapy *PLoS One* **13** e0205917
- Mudie D M et al 2014 Quantification of gastrointestinal liquid volumes and distribution following a 240 ml dose of water in the fasted state *Mol. Pharmaceutics* **11** 3039–47
- Niroomand-Rad A et al 2020 Report of AAPM task group 235 radiochromic film dosimetry: an update to TG-55 *Med. Phys.* **47** 5986–6025
- Nolden M et al 2013 The medical imaging interaction toolkit: challenges and advances: 10 years of open-source development *IJCARS* **8** 607–20
- Pallotta S et al 2019 ADAM phantom to test 4D medical imaging and dose delivery devices *Phys. Med. Biol.* **64** 105002
- Perrin R L et al 2017 An anthropomorphic breathing phantom of the thorax for testing new motion mitigation techniques for pencil beam scanning proton therapy *Phys. Med. Biol.* **62** 2486–504
- Phillips M H, Pedroni E, Blattmann H, Boehringer T, Coray A and Scheib S 1992 Effects of respiratory motion on dose uniformity with a charged particle scanning method *Phys. Med. Biol.* **37** 223–34
- Rawla P, Sunkara T and Gaduputi V 2019 Epidemiology of pancreatic cancer: global trends, etiology and risk factors *World J. Oncol.* **10** 10–27
- Steinmann A et al 2019 MRIgRT dynamic lung motion thorax anthropomorphic QA phantom: design, development, reproducibility, and feasibility study *Med. Phys.* **46** 5124–33
- Stengl C et al 2023 Development and characterization of a versatile mini-beam collimator for pre-clinical photon beam irradiation *Med. Phys.* **50** 5222–37
- Subashi E, Segars P, Veeraraghavan H, Deasy J and Tyagi N 2023 A model for gastrointestinal tract motility in a 4D imaging phantom of human anatomy *Med. Phys.* **50** 3066–75
- Tajik M, Akhlaqi M M and Gholami S 2022 Advances in anthropomorphic thorax phantoms for radiotherapy: a review *Biomed. Phys. Eng. Express* **8** 052001
- Toepker M, Euler G, Unger E, Weber M, Kienzl D, Herold C J and Ringl H 2013 Stenosis quantification of coronary arteries in coronary vessel phantoms with second-generation dual-source CT: influence of measurement parameters and limitations *Am. J. Roentgenol.* **201** W227–34
- Uchinami Y et al 2023 Evaluation of short-term gastrointestinal motion and its impact on dosimetric parameters in stereotactic body radiation therapy for pancreatic cancer *Clin. Transl. Radiat. Oncol.* **39** 100576
- Vedelago J, Karger C P and Jäkel O 2022 A review on reference dosimetry in radiation therapy with proton and light ion beams: status and impact of new developments *Radiat. Meas.* **157** 106844
- Versteijne E et al 2022 Neoadjuvant chemoradiotherapy versus upfront surgery for resectable and borderline resectable pancreatic cancer: long-term results of the dutch randomized PREOPANC trial *J. Clin. Oncol.* **40** 1220–30
- Vitolo V et al 2019 Preoperative chemotherapy and carbon ions therapy for treatment of resectable and borderline resectable pancreatic adenocarcinoma: a prospective, phase II, multicentre, single-arm study *BMC Cancer* **19** 922
- Waal T de et al 2020 Exploring the effect of esomeprazole on gastric and duodenal fluid volumes and absorption of ritonavir *Pharmaceutics* **12** 670
- Webb W R, Brant W E and Major N M 2006 Chapter 13 - Pancreas *Fundamentals of body CT* (Philadelphia, PA: Elsevier/Saunders) 3rd edn pp 247–63
- Weidner A et al 2022 An abdominal phantom with anthropomorphic organ motion and multimodal imaging contrast for MR-guided radiotherapy *Phys. Med. Biol.* **67** 045009
- Yovino S et al 2011 Intensity-modulated radiation therapy significantly improves acute gastrointestinal toxicity in pancreatic and ampullary cancers *IJROBP* **79** 158–62

2.2 Paper II

Development and characterization of a versatile mini-beam collimator for pre-clinical photon beam irradiation

Authors: Christina Stengl*, Eric Arbes, Long-Yang Jan Thai, Gernot Echner, José Vedelago, Jeannette Jansen, Oliver Jäkel, Joao Seco

*Corresponding author.

Journal reference: Med. Phys., 2023, 50; 5222-5237

DOI: 10.1002/mp.16432

Journal Impact Factor: 3.8

Source: <https://aapm.onlinelibrary.wiley.com/journal/24734209/journal-metrics>, accessed on 24 May 2024.



Received: 17 November 2022 | Revised: 5 April 2023 | Accepted: 6 April 2023

DOI: 10.1002/mp.16432

RESEARCH ARTICLE

MEDICAL PHYSICS

Development and characterization of a versatile mini-beam collimator for pre-clinical photon beam irradiation

Christina Stengl^{1,2,3} | Eric Arbes^{4,5} | Long-Yang Jan Thai^{4,5} | Gernot Echner^{1,3} | José Vedelago^{1,3} | Jeannette Jansen⁴ | Oliver Jäkel^{1,3,6} | Joao Seco^{4,5}¹Division of Medical Physics in Radiation Oncology, German Cancer Research Center (DKFZ), Heidelberg, Germany²Faculty of Medicine, University of Heidelberg, Heidelberg, Germany³Heidelberg Institute for Radiation Oncology (HIRO), National Center for Radiation Research in Oncology (NCRO), Heidelberg, Germany⁴Biomedical Physics in Radiation Oncology, German Cancer Research Center (DKFZ), Heidelberg, Germany⁵Department for Physics and Astronomy, University of Heidelberg, Heidelberg, Germany⁶Heidelberg Ion Beam Therapy Center (HIT), Heidelberg University Hospital, Heidelberg, Germany**Correspondence**

Christina Stengl, Division of Medical Physics in Radiation Oncology, German Cancer Research Center (DKFZ), Im Neuenheimer Feld 280, Heidelberg D-69120, Germany. Email: christina.stengl@dkfz.de

Oliver Jäkel and Joao Seco shared last-authorship position in this study.

Funding Information

Deutsches Krebsforschungszentrum (DKFZ)

Abstract**Background:** Interest in spatial fractionation radiotherapy has exponentially increased over the last decade as a significant reduction of healthy tissue toxicity was observed by mini-beam irradiation. Published studies, however, mostly use rigid mini-beam collimators dedicated to their exact experimental arrangement such that changing the setup or testing new mini-beam collimator configurations becomes challenging and expensive.**Purpose:** In this work, a versatile, low-cost mini-beam collimator was designed and manufactured for pre-clinical applications with X-ray beams. The mini-beam collimator enables variability of the full width at half maximum (FWHM), the center-to-center distance (ctc), the peak-to-valley dose ratio (PVDR), and the source-to-collimator distance (SCD).**Methods:** The mini-beam collimator is an in-house development, which was constructed of $10 \times 40 \text{ mm}^2$ tungsten or brass plates. These metal plates were combined with 3D-printed plastic plates that can be stacked together in the desired order. A standard X-ray source was used for the dosimetric characterization of four different configurations of the collimator, including a combination of plastic plates of 0.5, 1, or 2 mm width, assembled with 1 or 2 mm thick metal plates. Irradiations were done at three different SCDs for characterizing the performance of the collimator. For the SCDs closer to the radiation source, the plastic plates were 3D-printed with a dedicated angle to compensate for the X-ray beam divergence, making it possible to study ultra-high dose rates of around 40 Gy/s. All dosimetric quantifications were performed using EBT-XD films. Additionally, *in vitro* studies with H460 cells were carried out.**Results:** Characteristic mini-beam dose distributions were obtained with the developed collimator using a conventional X-ray source. With the exchangeable 3D-printed plates, FWHM and ctc from 0.52 to 2.11 mm, and from 1.77 to 4.61 mm were achieved, with uncertainties ranging from 0.01% to 8.98%, respectively. The FWHM and ctc obtained with the EBT-XD films are in agreement with the design of each mini-beam collimator configuration. For dose rates in the order of several Gy/min, the highest PVDR of 10.09 ± 1.08 was achieved with a collimator configuration of 0.5 mm thick plastic plates and 2 mm thick metal plates. Exchanging the tungsten plates with the lower-density metal brass reduced the PVDR by approximately 50%. Also, increasing the dose rate to ultra-high dose rates was feasible with the mini-beam collimator, where a PVDR of 24.26 ± 2.10 was achieved. Finally, it was possible to deliver and quantify mini-beam dose distribution patterns *in vitro*.

This is an open access article under the terms of the [Creative Commons Attribution-NonCommercial License](https://creativecommons.org/licenses/by-nc/4.0/), which permits use, distribution and reproduction in any medium, provided the original work is properly cited and is not used for commercial purposes.

© 2023 The Authors. *Medical Physics* published by Wiley Periodicals LLC on behalf of American Association of Physicists in Medicine.

5222 | [wileyonlinelibrary.com/journal/mp](https://onlinelibrary.wiley.com/journal/10.1002/mp)*Med Phys.* 2023;50:5222–5237.

Conclusions: With the developed collimator, we achieved various mini-beam dose distributions that can be adjusted according to the needs of the user in regards to FWHM, ctc, PVDR and SCD, while accounting for beam divergence. Therefore, the designed mini-beam collimator may enable low-cost and versatile pre-clinical research on mini-beam irradiation.

KEYWORDS

3D printing, dosimetry, mini-beam collimator, spatial fractionation

1 | INTRODUCTION

Mini-beam irradiation is a novel radiotherapy technique that utilizes spatial fractionation of the beam to increase the target dose while sparing organs at risk. This has the potential to improve tumor control and decrease side effects.^{1,2} First applied using synchrotron radiation, mini-beam irradiation introduces adjacent high-dose and low-dose regions in the target area referring to peaks and valleys, respectively. Thereby, it was possible to show high normal brain tissue tolerance to several hundred Grays.^{3–5} At the same time, significant tumor growth control could be achieved. The mechanism behind this so-called “mini-beam effect” is, however, not yet fully understood. Theories on the influence of the immune system, the abscopal effect, the vascular effect, or a combination of all three were already considered.^{6,7}

Mini-beam irradiation typically refers to a 0.2 to 1 mm slit width spaced by a 1 to 4 mm metal structure.^{8–10} Thereby, two different parameters define the geometrical form of the mini-beam pattern including full width at half maximum (FWHM) and center-to-center distance (ctc). Varying the peak width and therefore the FWHM has a significant impact on radiation toxicity. While a peak width of 0.5 to 1 mm did not reveal toxic outcomes, 3 mm of peak width induced severe skin reactions in an in vivo mice experiment.¹¹ The ctc usually considers the distance from the center of one peak to the center of the peak immediately next to it, and it is ideally a constant value throughout the mini-beam dose distribution. Common ctc values range from two times up to four times the given FWHM.^{9,10,12} Another relevant parameter for the biological response is the peak-to-valley dose ratio (PVDR). The mini-effect in vivo was shown even with PVDR values of 2.7, whereas PVDR values up to 20.1 were reported for different X-ray sources.^{13–15}

To make mini-beam irradiation available to a broad group of users, its feasibility on a small animal X-ray irradiation device was first tested in 2017.⁸ Thereby, it was shown that mini-beam irradiation can be made affordable and easy to access on these X-ray devices. Nevertheless, to introduce mini-beam dose delivery, a mini-beam collimator is required. One advantage of mini-beam collimators is their easy installation in such X-ray sources.¹⁵ However, the collimator must be suited for the source in terms of divergence to achieve a sharp and distinct pattern, thus making the change of

the source-to-collimator distance (SCD) and the switching of one collimator for different devices a challenging task. Furthermore, testing of different PVDRs is also necessary, as changes in this parameter have already been identified as one of the main players in the mini-beam irradiation effect. Two of the mainly used materials for mini-beam collimators are tungsten or brass.^{16,17} In particular, tungsten is known for its high attenuation coefficient for X-ray beams, making it a suitable material to achieve high PVDR values. Finally, the ability to control FWHM, ctc, and PVDR is crucial in pre-clinical studies of the mini-beam effect to understand the impact of each parameter separately.^{10,11,18}

This work concentrates on the development of a spatially and angularly adjustable mini-beam collimator for pre-clinical photon beam irradiation with a small animal irradiation device. The X-ray source was operated at 200 kV as standard condition and at 225 kV for ultra-high dose rate irradiations. The design of the mini-beam collimator aims at delivering reproducible spatially fractionated dose patterns, providing flexibility to explore the mini-beam effect. By combining tungsten or brass plates with 3D-printed plastic plates it was possible to change the divergence of the collimator as well as the dosimetric parameters, such as PVDR, FWHM, and ctc. To evaluate the feasibility of the collimator design, a dosimetric study was conducted by means of radiochromic films and complemented with in vitro irradiation of cells.

2 | METHODS

2.1 | Design of the mini-beam collimator

The mini-beam collimator consists of a variable number of metal plates with a size of $10.0 \times 40.0 \times 1.0 \text{ mm}^3$. The metal plates were combined with 3D-printed plastic material VeroClear (Stratasys, Israel) which has the same density as polymethyl methacrylate (PMMA). These plates are arranged in a 3D-printed scaffold, also made of VeroClear. A $40.2 \times 40.2 \text{ mm}^2$ cavity in the center of the scaffold enables the positioning of the plates. For all 3D-printed parts, a J55 3D printer was used (Stratasys, Israel). To assemble the collimator, the metal plates are placed alternately with $10.0 \times 40.0 \text{ mm}^2$ plastic plates with different widths in the scaffold. Three

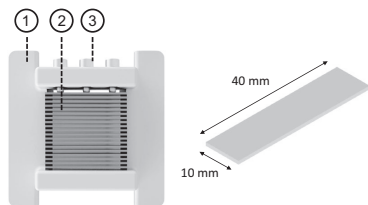


FIGURE 1 Rendering of the mini-beam collimator. The 3D-printed scaffold (1) holds the metal and plastic plates (2) screwed with three locking screws (3). The size and shape of the metal and plastic plates are represented on the right.

TABLE 1 Mini-beam collimator configurations with the information on material and collimator ID. Each collimator ID states the nominal plastic plate thickness, followed by the thickness of the metal plates, and a capital letter for the metal material, where T refers to tungsten and B refers to brass.

Mini-beam collimator ID	Plastic [mm]	Brass [mm]	Tungsten [mm]
1/1 B	1.0	1.0	-
2/2 B	2.0	2.0	-
0.5/1 B	0.5	1.0	-
0.5/2 B	0.5	2.0	-
1/1 T	1.0	-	1.0
2/2 T	2.0	-	2.0
0.5/1 T	0.5	-	1.0
0.5/2 T	0.5	-	2.0

M4 screws allow the locking of plates in their position in a reproducible way (Figure 1).

To obtain various FWHMs, the 3D-printed plastic plates were designed with nominal thicknesses of 0.5, 1.0 and 2.0 mm (Inventor Professional 2018, Autodesk, USA). To obtain different ctc values, either one or two metal plates were positioned in between the plastic plates. To gain distinct PVDR values, either tungsten (T) or brass (B) metal plates were used. For each mini-beam collimator configuration, the nominal thicknesses of the plates and the collimator IDs are given in Table 1.

A height of 10 mm of the tungsten plates was chosen to reach 100% attenuation of the applied X-ray beams of 200 and 225 keV.¹⁹ With 10 mm brass plates, no full attenuation of the beam is possible, yielding higher valley doses and consequently lower PVDR. Further details of the attenuation quantification for both metals are depicted in Figure S1. For easy handling of the mini-beam collimator, the plastic plates were 3D-printed with the same height of 10 mm. This 10 mm of plastic only attenuates 13.2% and 12.6% of a monoenergetic photon beam with an energy of 200 and 225 keV, respectively,¹⁹ making it possible to compensate for the X-ray beam divergence with a minor impact on the transmitted beam.

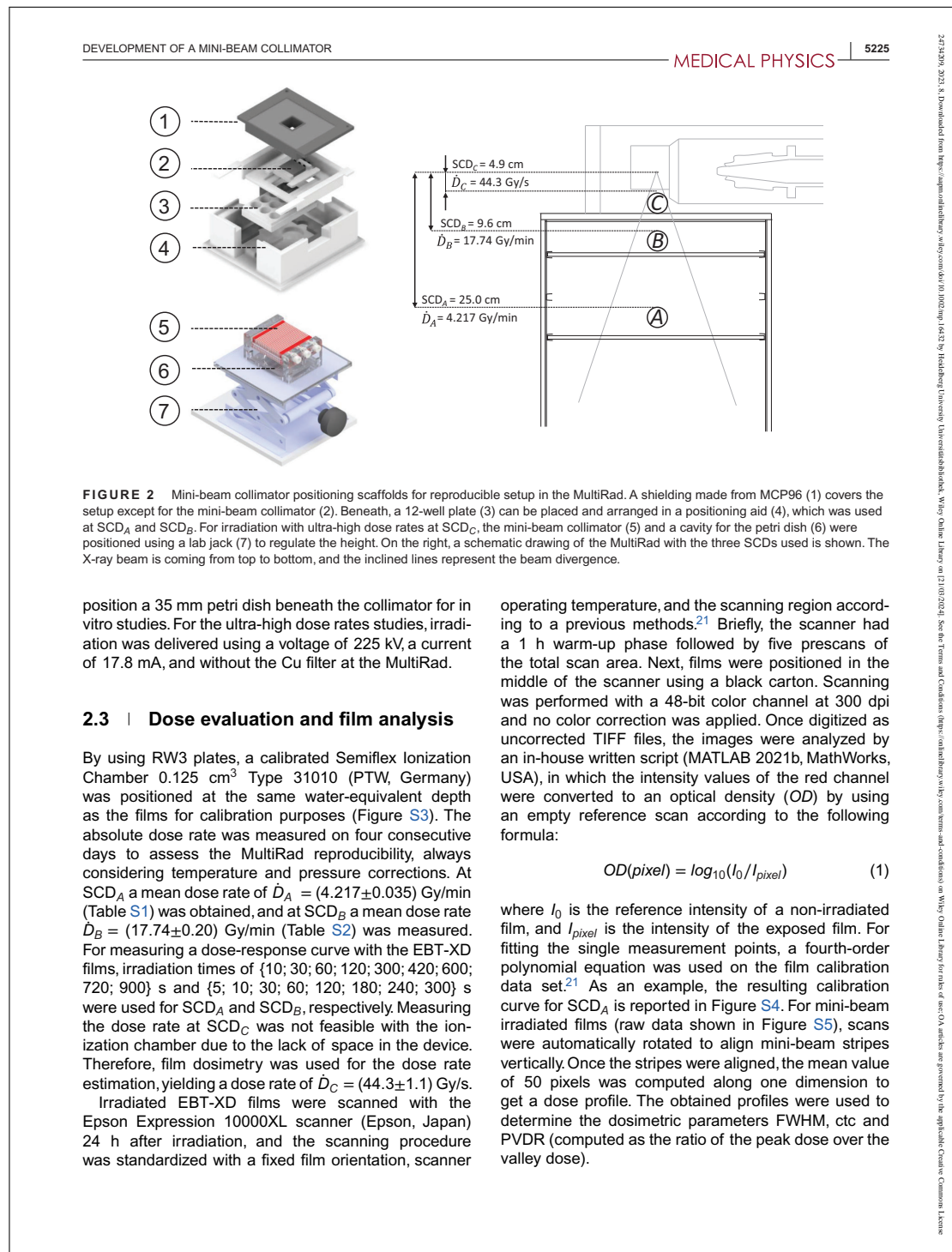
2.2 | Implementation of the mini-beam collimator at an X-ray device

The mini-beam collimator was tested at a Faxitron MultiRad 225 X-ray irradiation system (FAXITRON BIOPTICS, LLC, USA) which operates at accelerating voltages from 20 up to 225 kV. An in-house manufactured, custom-fit Plexiglas insert was used to avoid shaking and moving of the collimator at the different SCDs, enabling reproducible measurements by granting the right collimator position. A 3D-printed holder was fixed via two pins on top of the insert containing a positioning aid for a well plate to irradiate cells or to place a $2 \times 2 \text{ cm}^2$ cut EBT-XD Gafchromic film (Ashland, USA). The collimator was reproducibly positioned 25.0 cm apart from the source corresponding to SCD_A (Setup A in Figure 2). For this setup, parallel plastic plates were used (Figure S2). To measure the dose in an in vitro simulating experiment, one well of a 12-well plate was filled with 2 mL of water, and an EBT-XD film was fixed beneath the well plate such that a distance of 20.5 mm was between the collimator and the film. A home-made MCP96 shielding, with outer dimensions of $136.95 \times 110.00 \text{ mm}^2$, a height of 25.18 mm, and a $38.00 \times 38.00 \text{ mm}^2$ inner cavity, was placed on top of the mini-beam collimator to reduce scattering contributions. To measure dose profiles at various water-equivalent depths below the collimator, five films were positioned underneath the mini-beam collimator at a depth of {0; 2; 4; 10; 20} mm with 3D-printed VeroClear plates in between.

The collimator was also tested at an SCD of 9.6 cm (SCD_B) (Setup B in Figure 2). Positioning the collimator at SCD_B required 3D-printed plastic plates with an angle of 37.5° according to the beam angle reported by the manufacturer of the X-ray source to compensate for beam divergence (Figure S2). The setup is similar to the setup for SCD_A , however, due to the reduced space, no MCP96 shielding was used. Here, dosimetric films were positioned at a depth of 2 mm to simulate subcutaneous conditions. For both setups, irradiation was delivered using a voltage of 200 kV, a current of 17.8 mA, and a 0.5 mm thick Cu filter at the MultiRad.

To achieve ultra-high dose rates the collimator was placed 4.9 cm apart from the source (SCD_C). Therefore, the setup was changed to get closer to the source in the hole at the top of the MultiRad (Setup C in Figure 2), as it has been previously done in other studies with the same radiation device.²⁰ The plastic plates were designed according to the X-ray beam divergence (Figure S2). A lab jack¹ made it possible to adjust the height of the collimator to SCD_C . Similar to SCD_B , the EBT-XD films were placed at a 2 mm depth for SCD_C . The holders were constructed in such a way that it is also possible to

¹ For the render of the lab jack presented in Figure 2, an stl file from <https://grabcad.com/library/lab-jack-100mm-1>, accessed on 13 April 2022, was used.



For the parameters of the mini-beam pattern, the intra-profile-variation (σ_{intra}) of the mean values of the single peaks in one experiment was computed and in addition, the inter-profile-variation (σ_{inter}) of the mean values for three independent experiments were calculated. Since the readout resolution is of the order of 85 μm , all the mean values are reported rounded up to the tenths of micrometers.

2.4 | Mini-beam pattern in vitro

In addition to the film dosimetry characterization, in vitro studies were conducted using the H460 cell line. H460 cells were cultured to 80% confluency at 37°C with 5% CO₂ in Roswell Park Memorial Institute (RPMI) medium (22400-089, Gibco, Thermo Fisher Scientific, USA), supplemented with 10% fetal bovine serum (FBS, 10500064, Thermo Fisher Scientific, USA) and 1% PenStrep (15140122, Thermo Fisher Scientific, USA). For passaging, cells were first washed with 10 mL phosphate-buffered saline (PBS, D8537, Sigma Aldrich, USA) and then trypsinized with 3 mL TrypLE Express (12604-103, Gibco, Thermo Fisher Scientific, USA) for 8 min at 37°C. TrypLE was neutralized with 7 mL RPMI medium and centrifuged for 4 min at 1200 rpm. Next, cells were passaged 1:10, seeded with 10 mL RPMI in a 75 cm² culture flasks, and incubated at 37°C and 5% CO₂. For further experiments, cells were seeded on sterilized glass coverslips with a diameter of 19 mm in 12-well plates with a density of 500 000 cells/well one day before the irradiation.

24 h after seeding, cells were irradiated at SCD_A, with the setup proposed in Section 2.2 at a distance of 20.5 cm to the collimator. To enable equal irradiation in the valley for the given configurations, calibration curves were established for each mini-beam collimator configuration. Therefore, the applied dose is considered as the one obtained with the ionization chamber at SCD_A and the measured dose as the dose acquired from EBT-XD films using each mini-beam collimator configuration. To acquire these dose-response curves, EBT-XD films were irradiated with the mini-beam collimator for {1; 3; 5; 7; 10} min, and afterward, each peak and valley dose was quantified separately. Next, linear fits were computed for the valley dose values and the peak dose values using Prism 8 (GraphPad, USA) setting the intercept to the origin. Therewith, irradiation times for equal valley doses were calculated (Figure S6). For each mini-beam collimator configuration including 1/1 T, 2/2 T, 0.5/1 T, and 0.5/2 T, the valley dose was set to 4 Gy. Therefore, irradiation times were adjusted to {600; 635; 952; 1268} s, respectively.

Cell samples were fixed 30 min after irradiation with 0.5 mL 4% para-formaldehyde (PFA, 28908, Thermo Fisher Scientific, USA) for 15 min at room temperature (RT) and washed twice with PBS. Next, cells were

treated with 500 μL 0.25% TritonX in PBS solution for 10 min and blocked with 4% bovine serum albumin (BSA, A6003-25G, Sigma Aldrich, USA) in PBS for 1 h. Afterward, cells were stained with a rabbit γH2AX antibody (ab2893, Abcam, UK) in 1% BSA solution (1:1000) and incubated in a wet chamber overnight at 4°C. The next day, cells were washed three times with PBS, and the secondary anti-rabbit antibody (ab150077, Abcam, UK) coupled to Alexa 488 and dissolved in 1% BSA (1:1000) was applied for 60 min at RT in the dark. Then cells were washed twice with PBS and incubated with 4',6-Diamidino-2-phenylindol (DAPI, D9542, Sigma-Aldrich, USA) dissolved in PBS (1:1000) for 15 min. Subsequently, two washing steps with PBS were performed. Cells were imaged using a Zeiss Eclipse Ti2 Microscope (Zeiss, Germany) with a 10x/0.45 objective. Images for γH2AX and DAPI were taken over the entire cover glass using a stitching algorithm with an exposure time of 800 and 400 ms, respectively. Since DAPI was only used to find the right layer for fluorescence imaging, DAPI results were not included in the analysis.

After the acquisition of three independent coverslips for each configuration, images were analyzed regarding their fluorescence intensity profiles using an in-house written MATLAB script. Due to the non-homogeneous nature of cells on a coverslip, intensity profiles were smoothed with local regression weighted linear least squares to obtain the geometrical parameters FWHM and ctc. For the in vitro results, instead of reporting a PVDR, a peak-to-valley intensity ratio (PVIR) was calculated by dividing the fluorescence peak intensities by the valley intensities.

2.5 | Overview of experiments and irradiation conditions

In this study, a large variety of mini-beam collimator configurations and irradiation settings were used, and they are summarized in Table 2.

3 | RESULTS

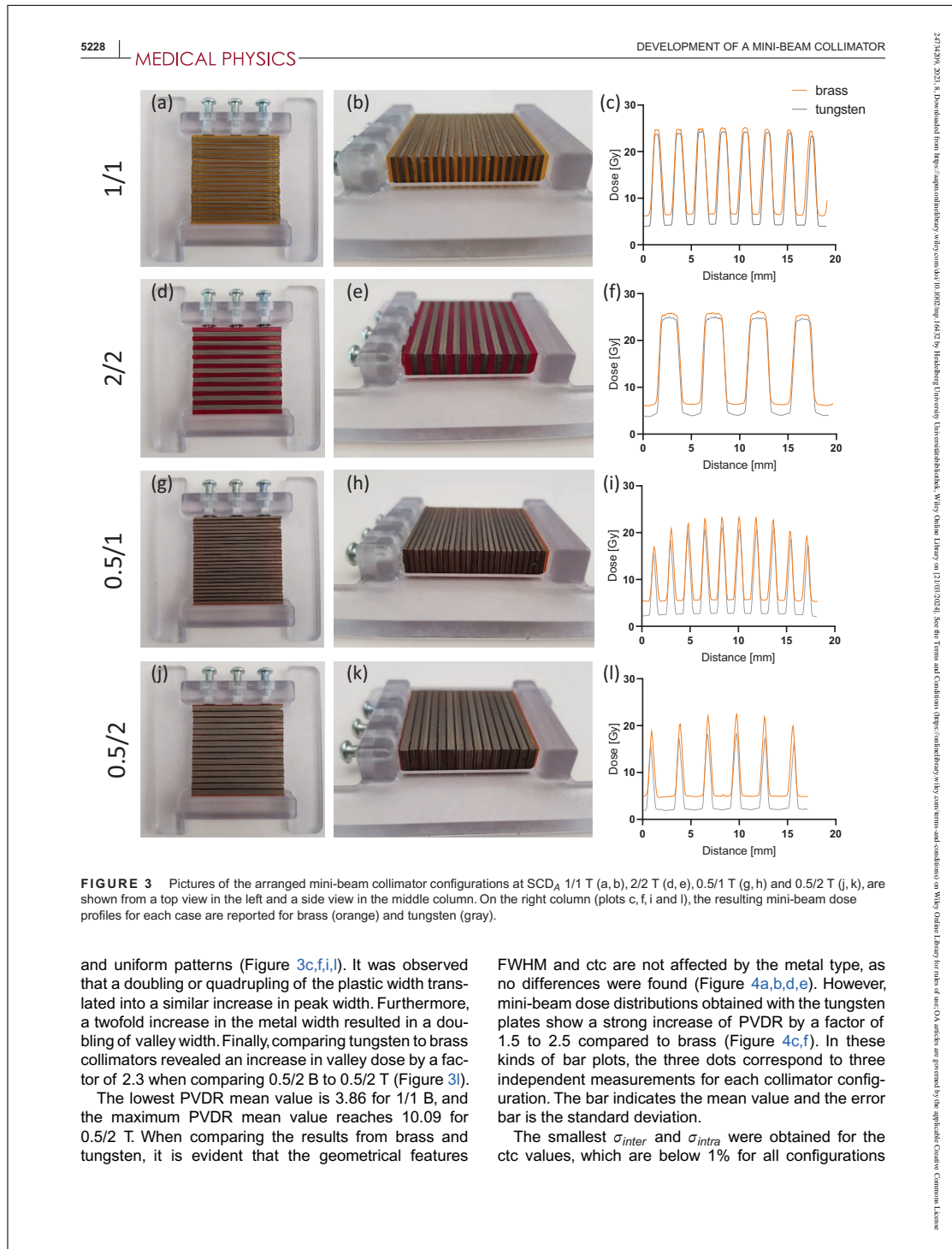
3.1 | Mini-beam collimator performance

To assess the performance of the designed mini-beam collimator with plastic plate widths from 0.5 to 2 mm and metal plate width of 1 or 2 mm (photos shown in Figure 3), the different mini-beam collimator configurations were positioned at SCD_A. The dosimetric parameters FWHM, ctc and PVDR of the resulting spatially fractionated dose distributions were evaluated from three independent EBT-XD film measurements. As an illustration, raw data is shown in Figure S5. The resulting dose profiles correlated with the given parameters of the mini-beam collimator configurations and indicated repetitive

TABLE 2 Overview of experiments and irradiation conditions of this study, presented according to each specific aim. The column "Divergence considered" states whether the X-ray beam divergence was considered in the mini-beam collimator design or not. The column "Quantification distance" indicates the distance from the mini-beam collimator to the quantification surface, either for film measurements or in vitro studies. For simplicity in summarizing the key parameters involved in each irradiation condition, the uncertainty of the dose rate value is not reported here; the reader is referred to Section 2.3 for these values. The section in which the results of each experiment are presented is reported in the last column.

Aim of the experiment	Mini-beam collimator IDs used	Divergence considered	Source-to-collimator distance (SCD)	X-ray source configuration	Dose rate	Quantified variables	Quantification distance	Results in section
General performance of the mini-beam collimator	1/1 T 2/2 T 0.5/1 T 0.5/2 T 1/1 B 2/2 B 0.5/1 B 0.5/2 B	no	SCD _A = 25.0 cm	200 kV; Copper filter	$\dot{D}_A = 4.217$ Gy/min	FWHM; ctc; PVDR; in-depth trend*	20.5 and *10; 2; 4; 10; 20) mm	3.1 Mini-beam collimator performance
Accounting for the X-ray divergence	1/1 T 2/2 T	yes	SCD _B = 9.6 cm	200 kV; Copper filter	$\dot{D}_B = 17.74$ Gy/min	FWHM; ctc; PVDR; in-depth trend*	2 and *10; 2; 4; 10; 20) mm	3.2 Mini-beam collimator accounting for beam divergence
Ultra-high dose rate compatibility	1/1 T 2/2 T	yes	SCD _C = 4.9 cm	225 kV; no filter	$\dot{D}_C = 44.3$ Gy/s	FWHM; ctc; PVDR	2 mm	3.3 Mini-beam collimator for ultra-high dose rate
In vitro feasibility	1/1 T 2/2 T 0.5/1 T 0.5/2 T	no	SCD _A = 25.0 cm	200 kV; Copper filter	$\dot{D}_A = 4.217$ Gy/min	Cell response; FWHM; ctc; PVIR	20.5 mm	3.4 In vitro response to mini-beam irradiation

Abbreviations: ctc, center-to-center distance; FWHM, full width at half maximum; PVDR, peak-to-valley dose ratio; SCD, source-to-collimator distance.



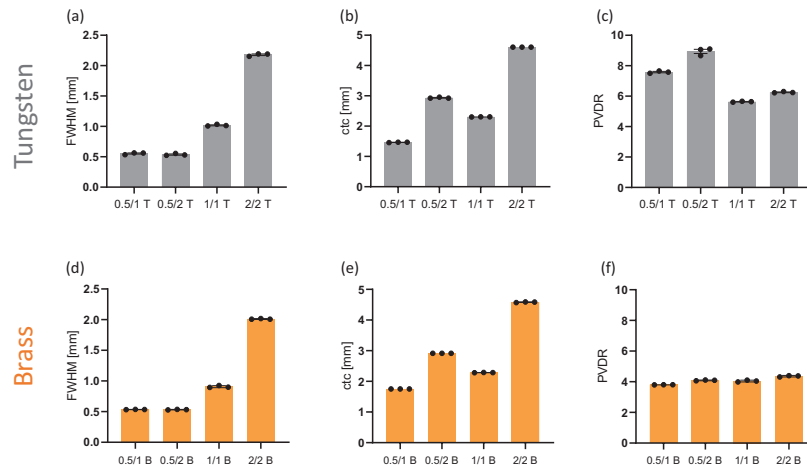


FIGURE 4 Dosimetric parameters obtained for the studied mini-beam collimator configurations. For tungsten (gray) and brass (orange), FWHM (a, d), ctc (b, e) and PVDR (c, f) were evaluated at SCD_A showing no difference in the first two parameters, but indicating an increase in PVDR using the tungsten collimator configurations. ctc, center-to-center distance; FWHM, full width at half maximum; PVDR, peak-to-valley dose ratio; SCD, source-to-collimator distance.

TABLE 3 Mean value of the dosimetric parameters FWHM, ctc and PVDR for all mini-beam collimator configurations. The σ_{inter} and σ_{intra} are reported.

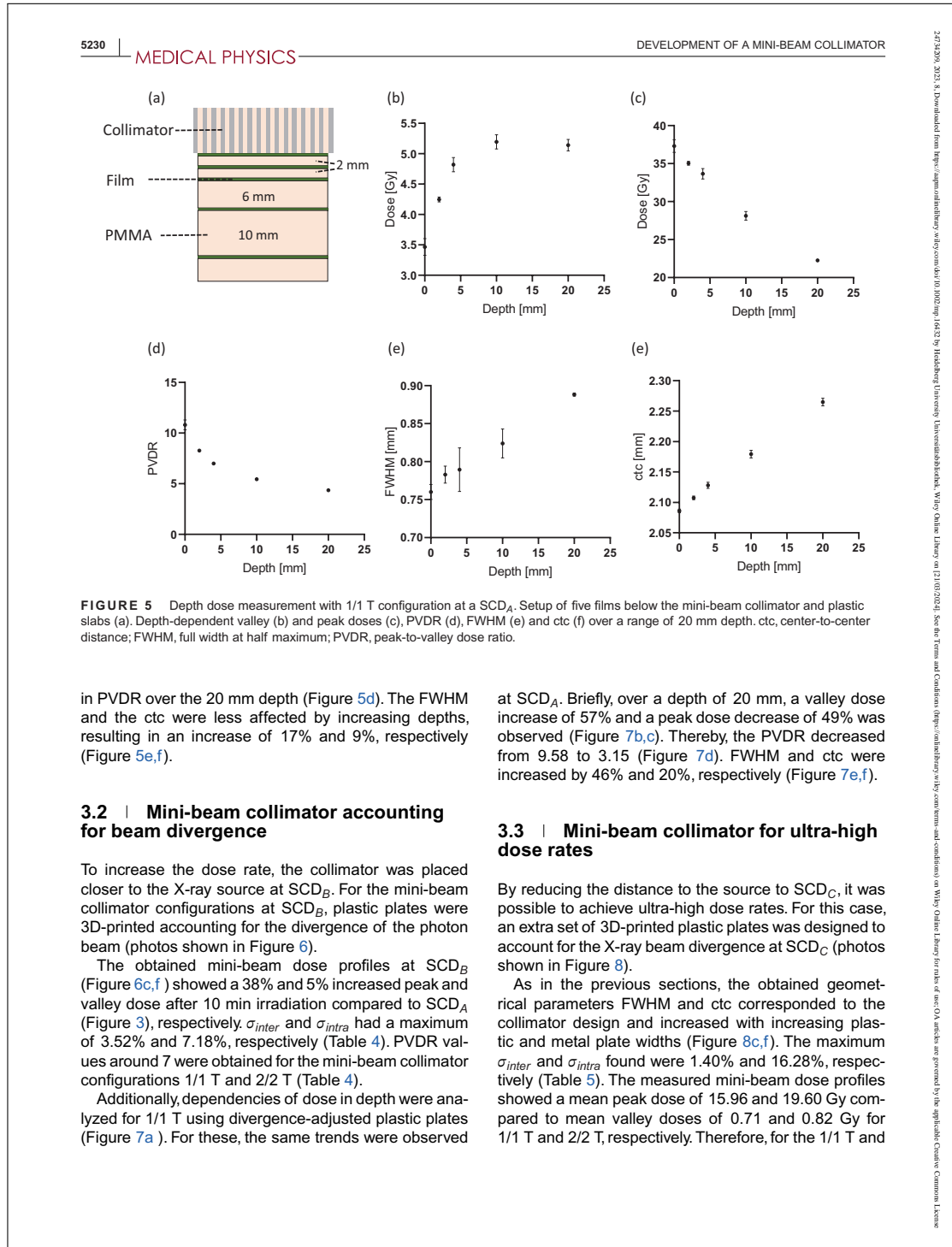
Mini-beam collimator ID	FWHM			ctc			PVDR		
	Mean [mm]	σ_{inter} [%]	σ_{intra} [%]	Mean [mm]	σ_{inter} [%]	σ_{intra} [%]	Mean	σ_{inter} [%]	σ_{intra} [%]
1/1 T	0.98	1.47	8.54	2.30	0.11	0.46	6.38	1.13	2.68
1/1 B	1.02	0.80	8.76	2.28	0.22	0.51	3.86	0.21	1.17
2/2 T	2.11	0.89	4.16	4.61	0.04	0.46	7.03	2.38	2.20
2/2 B	2.13	0.31	4.47	4.58	0.01	0.26	4.16	0.72	2.72
0.5/1 T	0.53	1.39	8.98	1.77	0.20	0.49	8.66	2.62	8.20
0.5/1 B	0.55	0.19	6.65	1.75	0.03	0.63	3.89	0.16	7.45
0.5/2 T	0.52	3.25	8.28	2.93	0.68	0.54	10.09	2.74	10.32
0.5/2 B	0.54	0.53	6.11	2.92	0.02	0.55	4.27	0.14	8.67

Abbreviations: ctc, center-to-center distance; FWHM, full width at half maximum; PVDR, peak-to-valley dose ratio.

including tungsten and brass (Table 3). The FWHM and the PVDR, however, show higher variations, since the σ_{intra} for the 0.5/2 T mini-beam collimator are 8.28% and 10.32%, respectively. On average, σ_{inter} are smaller than σ_{intra} . Nevertheless, both types of variations are not larger than 11% (Table 3), indicating that the designed mini-beam collimator is capable of generating proper mini-beam dose distributions while making the selection of the desired dosimetric parameters, such as FWHM, ctc and PVDR, possible according to the user's needs. These results show that higher PVDR values can be achieved with tungsten while maintaining the same geo-

metrical properties. Therefore, in the following sections, the mini-beam collimator was always assembled with the tungsten plates.

Dosimetric parameters were evaluated at several depths, aiming at further characterizing the performance of the mini-beam collimator. For this, the 1/1 T mini-beam collimator was used and dosimetric films were positioned in between PMMA slabs at several depths (Figure 5a). Thereby, an increase in valley dose and a decrease in peak dose of 33% and 40% were found, respectively, comparing a depth of 0 mm with a depth of 20 mm (Figure 5b,c). This resulted in a reduction of 60%



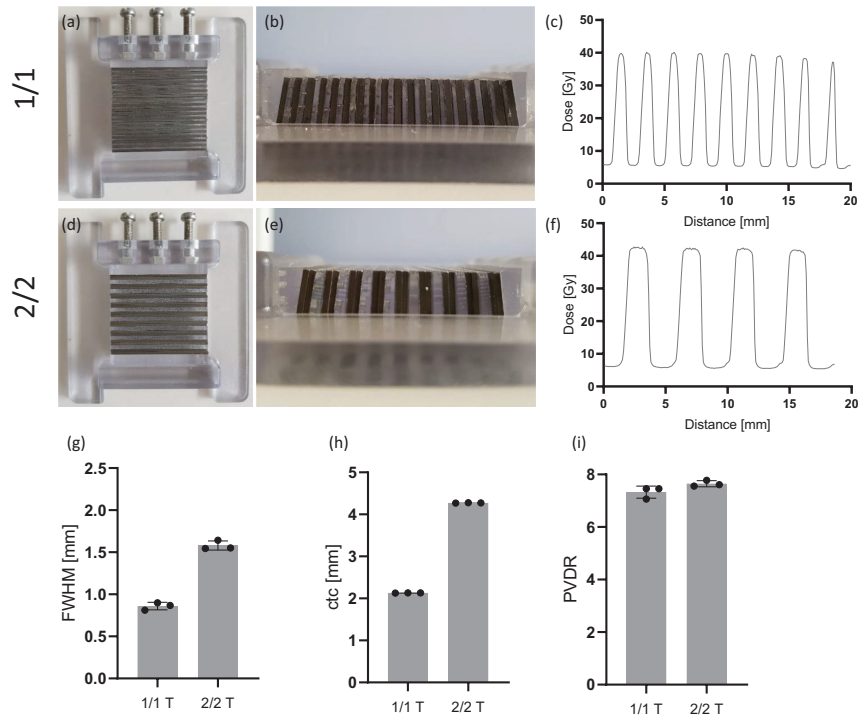


FIGURE 6 Pictures of the assembled mini-beam collimator for irradiations at SCD_B including configurations 1/1 T (a, b) and 2/2 T (d, e), are shown from a top view on the left column and a side view in the middle column. On the right, the exemplary resulting mini-beam dose profiles for each case are reported (c, f). From these, dosimetric parameters FWHM (g), ctc (h), and PVDR (i) were calculated. ctc, center-to-center distance; FWHM, full width at half maximum; PVDR, peak-to-valley dose ratio; SCD, source-to-collimator distance.

2/2 T mini-beam collimator configurations, mean PVDR values of 22.58 and 24.26 were found, respectively.

3.4 | In vitro response to mini-beam irradiation

The spatially fractionated irradiation generated with the mini-beam collimator caused a successive pattern of low (valley) and high (peak) γ H2AX fluorescence intensities indicating DNA damage. The intensity of the profiles in the valley regions presented maximum deviations of less than 7.1% from the mean value when comparing all the mini-beam collimator configurations, as intended when estimating the same valley dose of 4 Gy for each configuration. The characteristic mini-beam patterns were obtained, depicting a geometrical agreement with each mini-beam collimator configura-

tion (Figure 9a–d), and can also be interfered from the intensity profiles achieved from the fluorescence images (Figure 9e–h).

To further quantify the obtained results, FWHM and ctc were evaluated, revealing FWHM mean values from 0.66 mm to 2.35 mm, and ctc mean values from 1.75 mm to 4.60 mm (Figure 9i–j). The σ_{inter} uncertainties for both geometrical parameters are lower than 6% (Table 6). Since the mini-beam profiles correspond to the γ H2AX fluorescence intensities, larger standard deviations of 13% were obtained for the PVIR (Figure 9k), as compared to the PVDR values obtained with EBT-XD for the same mini-beam collimator configurations. Nevertheless, a maximum PVIR mean value of 1.68 was achieved for 1/1 T. As shown, different mini-beam dose distributions were successfully quantified in vitro. These results support the capabilities of the developed mini-beam collimator for in vitro studies.

TABLE 4 Mean value of the dosimetric parameters FWHM, ctc and PVDR for the mini-beam collimator configurations accounting for the X-ray beam divergence at a SCD_B. For each parameter the σ_{inter} and σ_{intra} are shown.

Mini-beam collimator ID	FWHM			ctc			PVDR		
	Mean [mm]	σ_{inter} [%]	σ_{intra} [%]	Mean [mm]	σ_{inter} [%]	σ_{intra} [%]	Mean	σ_{inter} [%]	σ_{intra} [%]
1/1 T	0.89	3.52	3.16	2.13	0.05	2.46	7.33	3.10	3.38
2/2 T	1.58	3.46	7.18	4.27	0.07	0.20	7.65	1.51	1.99

Abbreviations: ctc, center-to-center distance; FWHM, full width at half maximum; PVDR, peak-to-valley dose ratio; SCD, source-to-collimator distance.

4 | DISCUSSION

Most mini-beam collimators found in the literature are rigid and inflexible, in terms of FWHM, ctc, PVDR, and divergence compensation, making it demanding to adapt the setup to variable needs.^{10,17} Therefore, during this pre-clinical study, a simple and affordable flexible mini-beam collimator was developed by combining rectangular metal plates with 3D printing. This mini-beam collimator can be easily adapted to any setup and SCD, by adjusting the mini-beam delivery for different FWHM, ctc, and PVDR, while accounting for the beam divergence.

For building the mini-beam collimator, two main materials were used, namely rectangular-shaped metal plates and 3D-printed plastic plates. The rectangular-shaped metal plates create the valley region in the mini-beam dose profile. Due to their form, the production is easier and cheaper, compared to wire eroding, a method often used to manufacture thin slits for mini-beam collimators.⁹ Furthermore, this geometry also allows fast exchange of different metal types to be used for the mini-beam collimator. The 3D-printed plastic plates enable the peak dose in the mini-beam dose profile. Thanks to the fast prototyping of the 3D-printing technology,^{22–24} it was not only possible to create several plastic plates with different thicknesses and angles to change FWHM and ctc as well as compensate for beam divergence but also to design mounting setups for reproducible positioning of the mini-beam collimator in the MultiRad. The relevance of aligning the mini-beam collimator properly in the center of the X-ray radiation field is illustrated in Figure S7.

FWHM and ctc were quantified as dosimetric parameters to characterize the mini-beam collimator. These two parameters are necessary to understand the geometrical composition of the mini-beam pattern, as they are directly correlated to the peak and valley width. It was possible to change the nominal FWHM in the mini-beam collimator design by changing the plastic plates' width, whereas the ctc was determined by the sum of plastic and metal plates. Thereby, a large set of different FWHMs and ctc was covered, with mean values within 0.52 to 2.13 mm for the FWHM, and from 1.75 up to 4.61 mm for the ctc (Figure 4, Table 3).

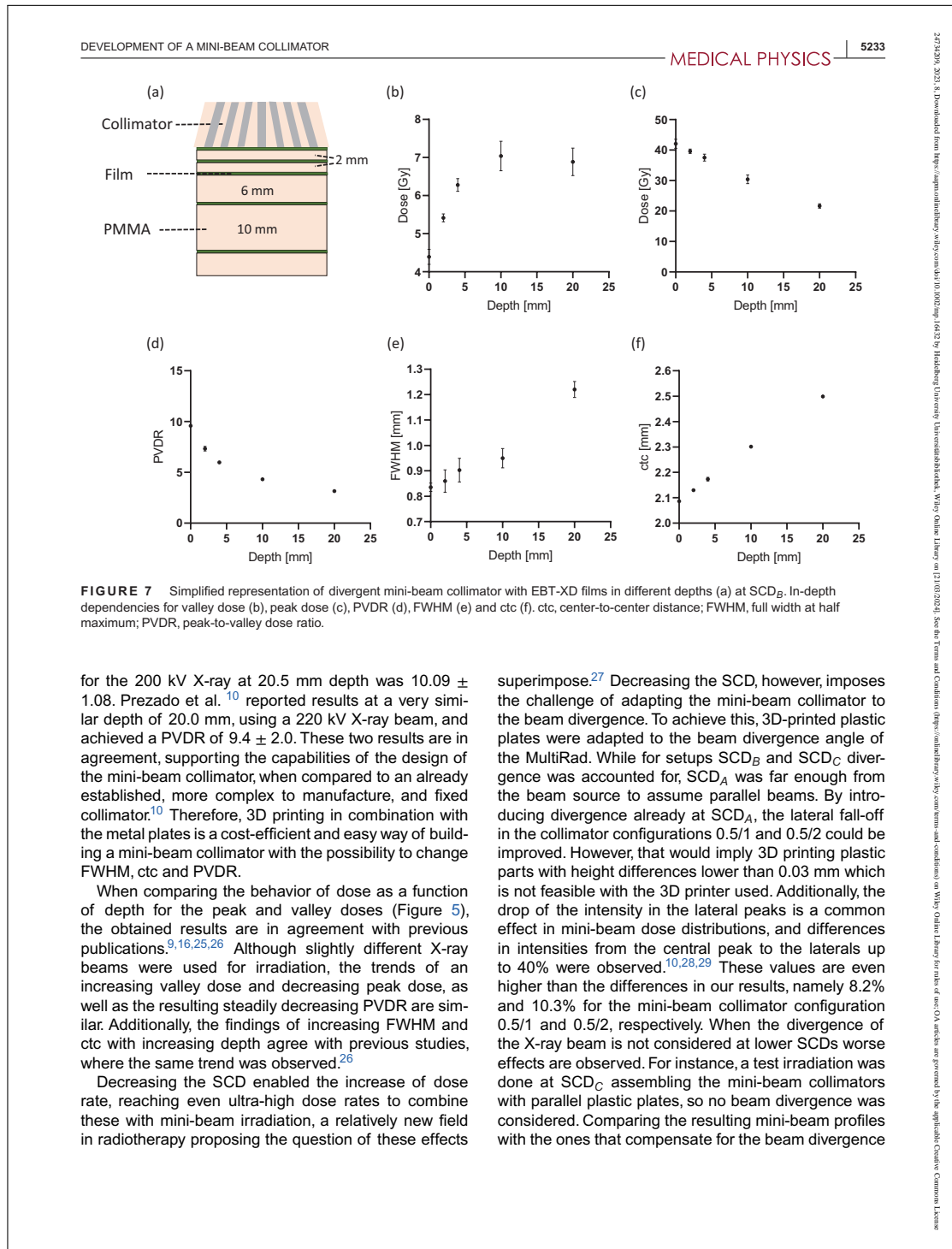
Different FWHM and ctc may be easily achieved by implementing relatively small changes in the mini-

beam collimator design. Furthermore, the change in metal type for the collimator did not affect these geometrical parameters and yielded changes in the PVDR values. For each parameter, σ_{intra} and σ_{inter} were calculated to give a more in-depth analysis of the dose profiles. Therefore, it was possible to measure differences between independent irradiations to evaluate the reproducibility, and additionally to compare each peak intensity within the same mini-beam dose profile to acquire knowledge on the beam divergence compensation.

The different FWHM and ctc values were achieved by varying the widths of the 3D-printed plastic plates with nominal thicknesses of 0.5, 1.0 and 2.0 mm. Nevertheless, 3D printing also has some limitations including its resolution of 0.05 mm for the used geometries. This could be improved in the future with the newly emerging high-performance laser lithography systems for 3D printing,² that can resolve smaller than 200 nm and would enable a FWHM below 0.5 mm. Designing the plastic plates with a specific angle according to the radiation source, which is greatly feasible with 3D printing, allows the adaption of the mini-beam collimator to any divergence (Figure 6 and Figure 8). Additionally, VeroClear has the same density as PMMA and a 10 mm thick plate does only attenuate 13.2% and 12.6% of a mono-energetic photon beam with an energy of 200 keV and 225 keV, respectively.¹⁹ Therefore, with these plastic plates it is possible to compensate for the X-ray beam divergence with a minor impact on the transmitted beam within the peak areas.

Valley regions were created in the mini-beam pattern using two different metals including tungsten and brass with a height of 10 mm. Thereby, almost 100% of irradiation is absorbed for energies of 200 and 225 keV for tungsten, while brass enables attenuation of 75% at these energies (Figure S1). The exchange of the material enabled the alteration of the PVDR values. Using other metals with different mass attenuation coefficients would enable even finer graduation of the PVDR values. For example, it could be worth considering aluminum and iron for further studies. However, to achieve PVDR values higher than 10, other properties must be changed such as the beam source. The highest PVDR value

² https://www.kit.edu/kit/english/pi_2013_12589.php, accessed on 20 February 2023.



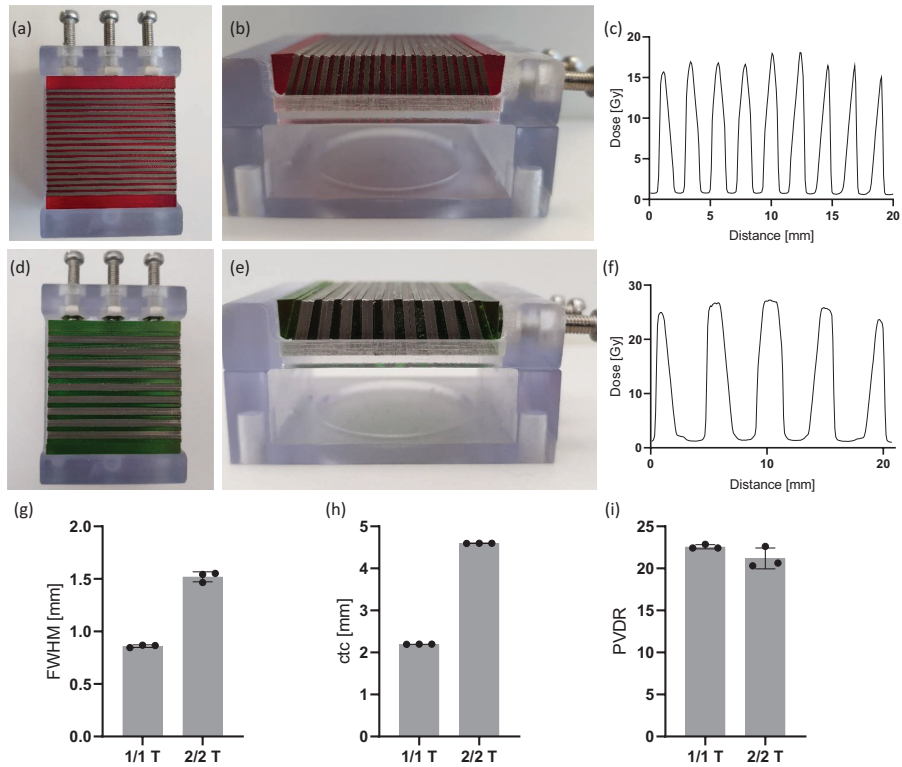


FIGURE 8 Mini-beam collimator for ultra-high dose rates at SCD_C from top (a, d), side view (b, e) and resulting dose profile for 1/1 T and 2/2 T (c, f), respectively. Dosimetric parameters including FWHM (g), ctc (h) and PVDR (i) were analyzed. ctc, center-to-center distance; FWHM, full width at half maximum; PVDR, peak-to-valley dose ratio.

TABLE 5 Mean value of the dosimetric parameters FWHM, ctc and PVDR for the mini-beam collimator configurations 1/1 T and 2/2 T at SCD_C for ultra-high dose rates irradiation conditions. For each parameter, σ_{inter} and σ_{intra} are reported.

Mini-beam collimator ID	FWHM			ctc			PVDR		
	Mean [mm]	σ_{inter} [%]	σ_{intra} [%]	Mean [mm]	σ_{inter} [%]	σ_{intra} [%]	Mean	σ_{inter} [%]	σ_{intra} [%]
1/1 T	0.86	1.40	13.93	2.20	0.09	1.27	22.58	1.14	8.57
2/2 T	1.64	1.14	16.28	4.42	0.21	0.99	24.26	6.30	4.80

Abbreviations: ctc, center-to-center distance; FWHM, full width at half maximum; PVDR, peak-to-valley dose ratio; SCD, source-to-collimator distance.

(Figure S8), only 6 peaks are observed instead of 9. The drop in intensity of the lateral peaks is evident, with less than 31% of the intensity of the central peaks. Therefore, it is essential to compensate for divergence at lower SCDs.

In this study, EBT-XD films were used as dosimeters, also for UHDR irradiations at SCD_C . Although there

are not many dedicated studies about the response of EBT-XD films in UHDR for photon beams, a dose overestimation of 3% – 5% for a dose rate of over 40 Gy/s was reported for protons.^{30–32} The dose overestimation trends to increase with increasing dose rate, for instance, 12% overestimation was reported for dose rates of 7500 Gy/s.³⁰ Other studies have reported

TABLE 6 Mean value of FWHM, ctc, and PVIR for the tungsten mini-beam collimator configurations in vitro, calculated from fluorescence intensity. For each parameter, σ_{inter} and σ_{intra} are reported.

Mini-beam collimator ID	FWHM			ctc			PVIR		
	Mean [mm]	σ_{inter} [%]	σ_{intra} [%]	Mean [mm]	σ_{inter} [%]	σ_{intra} [%]	Mean	σ_{inter} [%]	σ_{intra} [%]
1/1 T	1.18	5.58	6.47	2.29	0.44	1.28	1.68	13.17	3.78
2/2 T	2.35	2.68	6.88	4.60	1.22	3.56	1.56	3.40	5.89
0.5/1 T	0.69	2.20	10.99	1.75	0.39	2.07	1.57	5.69	4.91
0.5/2 T	0.66	2.54	16.70	2.87	3.83	2.82	1.64	13.65	4.30

Abbreviations: ctc, center-to-center distance; FWHM, full width at half maximum; PVIR, peak-to-valley intensity ratio.

differences below 2% or even less for dose rates up to 20 000 Gy/s.^{33–35} The results obtained from the films irradiated at SCD_C might be affected by this overestimation effect. While this has probably no quantifiable impact on the geometrical parameters, the PVDR values might be overestimated by at most 5%, since the used UHDR is in the lower limit of the discussed ranges.

In addition to the characterization of the mini-beam collimator with EBT-XD films, in vitro studies were carried out. Thereby, it was shown that the developed mini-beam collimator is capable to induce successive peak and valley patterns with the desired geometrical

outcome, showing a similar trend for FWHM and ctc compared to film dosimetry (Figure 9). DNA damage, visualized indirectly with γ H2AX, could be detected in areas of peak regions, while valley regions were less affected and therefore show less γ H2AX fluorescence intensity. Furthermore, our results match similar experiments that have been conducted before in which the peak regions could be clearly distinguished from valley regions.¹⁶ To enable the analysis of the large area of the coverslip, a tile scan was acquired, resulting in small artifacts of black dots in the corners of every single image. To overcome these issues when computing

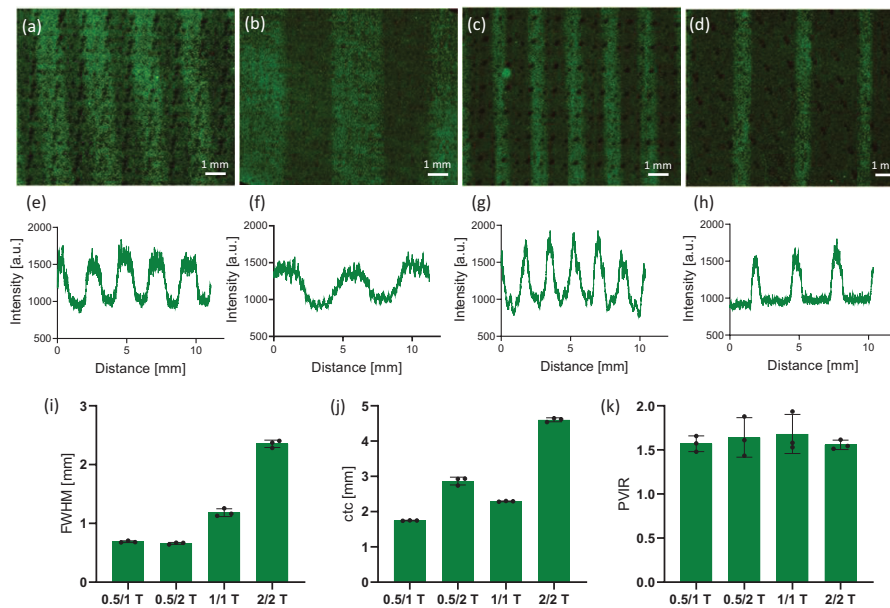


FIGURE 9 Microscopy images of H460 cells for the mini-beam collimator configurations 1/1 T (a), 2/2 T (b), 0.5/1 T (c) and 0.5/2 T (d), along with their intensity profiles (e–h). Fixed cells were stained with γ H2AX and imaged with a 10x objective. Contrast and brightness were adjusted for better visualization. The parameters FWHM (i), ctc (j), and PVDR (k) derived from the intensity profiles of microscopy images were calculated. ctc, center-to-center distance; FWHM, full width at half maximum; PVDR, peak-to-valley dose ratio.

FWHM and ctc, each tile scan was averaged, and the resulting intensity profiles were smoothed. The calculated PVIR was lower compared to the PVDR measured with films. This can be explained by the signal acquisition of both methods. The intensity of the γ H2AX staining can not be directly compared to the dose measurements of a dosimetric film. Furthermore, mini-beam irradiation seems to induce a non-linear dose response using γ H2AX staining.^{36,37} Despite this, the in vitro cell response showed a good agreement with film measurements in terms of the geometrical parameters FWHM and ctc (Figure S9), as it can be observed when comparing the results reported in Table 3 to the ones reported in Table 6 (Table S3 for a direct comparison of the value).

In the future, in vivo studies could also be performed with the developed mini-beam collimator, to further characterize the mini-beam irradiation effect. Especially, translational research can benefit therefrom as more evidencing data is needed to confidently start patient mini-beam treatment. Furthermore, treatment with protons and also heavier ions in combination with mini-beam irradiation will be the next step that needs to be studied with the proposed mini-beam collimator as promising results have been published in this growing field.^{2,38,39}

5 | CONCLUSION

A new, variable mini-beam collimator was developed for pre-clinical photon beam irradiation that enables the selection of FWHM, ctc, PVDR, and divergence for an arbitrary desired setup. Herewith, a versatile tool for spatially fractionated dose delivery was created, that can be fitted to any irradiation device using 3D printing. The simplicity of this approach gives access to a low-cost mini-beam collimator. The FWHM and ctc of the mini-beam dose distribution were easily adapted by positioning 3D-printed plastic plates of several sizes, and increasing or decreasing the number of metal plates. The divergence of the X-ray beam was properly accounted for by dedicated designs of the plastic plates, providing the additional opportunity of changing the SCD. Furthermore, by exchanging brass with tungsten, different PVDR values were achieved. The mentioned dosimetric parameters were quantified using film dosimetry at three different SCD, and mean PVDR values from 3.86 up to 24.26 were obtained. Additionally, cell experiments were carried out confirming the mini-beam dose patterns in vitro.

AUTHOR CONTRIBUTIONS

Christina Stengl: Conceptualization, data curation, formal analysis, investigation, methodology, project administration, software, visualization, Writing - original draft preparation, writing - review and editing. **Eric Arbes:**

Data curation, software, investigation, writing - review and editing **Long-Yang Jan Thai:** Data curation, investigation, writing - review and editing **Gernot Echner:** Conceptualization, resources, writing - reviewing and editing. **José Vedelago:** Conceptualization, writing - original draft preparation, writing - reviewing and editing. **Jeannette Jansen:** Conceptualization, writing - reviewing and editing. **Oliver Jäkel:** Funding acquisition, project administration, resources, supervision, writing - review and editing. **Joao Seco:** Funding acquisition, project administration, resources, supervision, writing - review and editing.

ACKNOWLEDGEMENTS

The authors would like to express their very great gratitude to the Division of Radiooncology/Radiobiology for providing the lab infrastructure and access to the Zeiss Eclipse Ti2 Microscope. The authors are grateful to the members of the mechanical workshop of the DKFZ for providing the brass plates and to the company Schmitz CNC Präzisionsfertigung GmbH & Co. KG for providing the tungsten plates. Additionally, C.S. wants to acknowledge the funding from the Helmholtz graduate school for cancer research of the DKFZ, within their PhD program. Open Access funding enabled and organized by Projekt DEAL.

CONFLICT OF INTEREST STATEMENT

The authors have no conflicts to disclose.

REFERENCES

1. Regnard P, Le Duc G, Bräuer-Krisch E, et al. Irradiation of intracerebral 9L gliosarcoma by a single array of microplanar x-ray beams from a synchrotron: balance between curing and sparing. *Phys Med Biol*. 2008;53:861-878.
2. Girst S, Greubel C, Reindl J, et al. Proton minibeam radiation therapy reduces side effects in an in vivo mouse ear model. *IJROBP*. 2016;95:234-241.
3. Slatkin DN, Spanne P, Dilmanian FA, Gebbers JO, Laissue JA. Subacute neuropathological effects of microplanar beams of x-rays from a synchrotron wiggler. *PNAS*. 1995;92:8783-8787.
4. Kundapur V, Mayer M, Auer RN, et al. Is mini beam ready for human trials? Results of randomized study of treating de-novo brain tumors in canines using linear accelerator generated mini beams. *Radiat Res*. 2022;198:162-171.
5. Dilmanian FA, Button TM, Le Duc G, et al. Response of rat intracranial 9L gliosarcoma to microbeam radiation therapy. *Neuro Oncol*. 2002;4:26-38.
6. Griffin RJ, Ahmed MM, Amendola B, et al. Understanding high-dose, ultra-high dose rate, and spatially fractionated radiation therapy. *IJROBP*. 2020;107:766-778.
7. Moghaddasi L, Reid P, Bezak E, Marcu LG. Radiobiological and treatment-related aspects of spatially fractionated radiotherapy. *Int J Mol Sci*. 2022;23. <https://doi.org/10.3390/ijms23063366>
8. Bazzyar S, Inscoc CR, O'Brian ET, Zhou O, Lee YZ. Minibeam radiotherapy with small animal irradiators: in vitro and in vivo feasibility studies. *Phys Med Biol*. 2017;62:8924-8942.
9. Treibel F, Nguyen M, Ahmed M, et al. Establishment of microbeam radiation therapy at a small-animal irradiator. *Int J Radiat Oncol Biol Phys*. 2021;109:626-636.

10. Prezado Y, Dos Santos M, Gonzalez W, et al. Transfer of Minibeam Radiation Therapy into a cost-effective equipment for radiobiological studies: a proof of concept. *Sci Rep.* 2017;7:17295.
11. Sammer M, Teiluf K, Girst S, et al. Beam size limit for pencil minibeam radiotherapy determined from side effects in an in-vivo mouse ear model. *PLoS One.* 2019;14:e0221454.
12. Ahmed M, Bicher S, Stewart RD, et al. Dosimetric quantities and cell survival for spatially fractionated radiation therapy. *Front Phys.* 2023;10. <https://doi.org/10.3389/fphy.2022.1064860>
13. Prezado Y, Thengumpallil S, Renier M, Bravin A. X-ray energy optimization in minibeam radiation therapy. *Med Phys.* 2009;36:4897-4902.
14. Dilmanian FA, Zhong Z, Bacarian T, et al. Interlaced x-ray microplanar beams: a radiosurgery approach with clinical potential. *PNAS.* 2006;103:9709-9714.
15. Sotiropoulos M, Brisebard E, Le Dudal M, et al. X-rays minibeam radiation therapy at a conventional irradiator: Pilot evaluation in F98-glioma bearing rats and dose calculations in a human phantom. *Clin Transl Radiat Oncol.* 2021;27:44-49.
16. Bartzsch S, Cummings C, Eismann S, Oelfke U. A preclinical microbeam facility with a conventional x-ray tube. *Med Phys.* 2016;43:6301.
17. Kim M, Hwang U-J, Park K, et al. Dose profile modulation of proton minibeam for clinical application. *Cancers.* 2022;14:2888. <https://doi.org/10.3390/cancers14122888>
18. Schneider T, de Marzi L, Patriarca A, Prezado Y. Monte Carlo comparison of proton and helium-ion minibeam generation techniques. *Front Phys.* 2021;9:595721. <https://doi.org/10.3389/fphy.2021.595721>
19. Hubbell J, Seltzer S. X-Ray mass attenuation coefficients. NIST standard reference database 126. 2004. <https://doi.org/10.18434/T4D01F>
20. Jansen J, Knoll J, Beyreuther E, et al. Does FLASH deplete oxygen? Experimental evaluation for photons, protons, and carbon ions. *Med Phys.* 2021;48:3982-3990.
21. Niroomand-Rad A, Chiu-Tsao S-T, Grams MP, et al. Report of AAPM Task Group 235 radiochromic film dosimetry: an update to TG-55. *Med Phys.* 2020;47:5986-6025.
22. Wang X, Wang X, Xiang Z, et al. The clinical application of 3D-printed boluses in superficial tumor radiotherapy. *Front Oncol.* 2021;11:698773.
23. Haefner MF, Giesel FL, Matke M, et al. 3D-printed masks as a new approach for immobilization in radiotherapy - a study of positioning accuracy. *Oncotarget.* 2018;9:6490-6498.
24. Meyer T, Quirk S, D'Souza M, Spencer D, Roumeliotis M. A framework for clinical commissioning of 3D-printed patient support or immobilization devices in photon radiotherapy. *J Appl Clin Med Phys.* 2018;19:499-505.
25. Lee E, Meyer J, Sandison G. Collimator design for spatially-fractionated proton beams for radiobiology research. *Phys Med Biol.* 2016;61:5378-5389.
26. Johnson TR, Bassil AM, Williams NT, et al. An investigation of kV mini-GRID spatially fractionated radiation therapy: dosimetry and preclinical trial. *Phys Med Biol.* 2022;67:045017.
27. Reindl J, Girst S. pMB FLASH - status and perspectives of combining proton minibeam with FLASH radiotherapy. *J Cancer Immunol.* 2019;1:14-23.
28. Dilmanian FA, Krishnan S, McLaughlin WE, et al. Merging orthovoltage X-Ray Minibeams spare the proximal tissues while producing a solid beam at the target. *Sci Rep.* 2019;9:1198.
29. Babcock K, Sidhu N, Kundapur V, Ali K. Collimator design for experimental minibeam radiation therapy. *Med Phys.* 2011;38:2192-2197.
30. Villoing D, Koumeir C, Bongrand A, et al. Technical note: proton beam dosimetry at ultra-high dose rates (FLASH): evaluation of GAFchromic™ (EBT3, EBT-XD) and OrthoChromic (OC-1) film performances. *Med Phys.* 2022;49:2732-2745.
31. Charyyev S, Chang C-W, Zhu M, Lin L, Langen K, Dhabaan A. Characterization of 250 MeV protons from the Varian ProBeam PBS system for FLASH radiation therapy. *Int J Part Ther.* 2023. <https://doi.org/10.14338/IJPT-22-00027.1>
32. Guan F, Wang X, Yang M, et al. Dosimetric response of Gafchromic™ EBT-XD film to therapeutic protons. *Precis Radiat Oncol.* 2023;7:15-26.
33. Szpala S, Huang V, Zhao Y, et al. Dosimetry with a clinical linac adapted to FLASH electron beams. *J Appl Clin Med Phys.* 2021;22:50-59.
34. Borowicz DM, Kruszyna-Mochalska M, Shipulin K, Molokanov A, Mytsin G, Malicki J. Comparison of dose-response curves between EBT-XD and EBT3 radiochromic films at high dose range (2000-4500 cGy) for a 175 MeV proton beam. *Phys Part Nuclei Lett.* 2021;18:691-699.
35. Yang M, Wang X, Guan F, et al. Adaptation and dosimetric commissioning of a synchrotron-based proton beamline for FLASH experiments. *Phys Med Biol.* 2022;67:165002. <https://doi.org/10.1088/1361-6560/ac8269>
36. Fernandez-Palomo C, Mothersill C, Bräuer-Krisch E, Laissee J, Seymour C, Schülke E. γ -H2AX as a marker for dose deposition in the brain of wistar rats after synchrotron microbeam radiation. *PLoS One.* 2015;10:e0119924.
37. Ventura JA, Donoghue JF, Nowell CJ, et al. The γ H2AX DSB marker may not be a suitable biodosimeter to measure the biological MRT valley dose. *Int J Radiat Biol.* 2021;97:642-656.
38. Dilmanian FA, Eley JG, Rusek A, Krishnan S. Charged particle therapy with mini-segmented beams. *Front Oncol.* 2015;5:269.
39. Sammer M, Girst S, Dollinger G. Optimizing proton minibeam radiotherapy by interlacing and heterogeneous tumor dose on the basis of calculated clonogenic cell survival. *Sci Rep.* 2021;11:3533.

SUPPORTING INFORMATION

Additional supporting information can be found online in the Supporting Information section at the end of this article.

How to cite this article: Stengl C, Arbes E, Thai L-YJ, et al. Development and characterization of a versatile mini-beam collimator for pre-clinical photon beam irradiation. *Med Phys.* 2023;50:5222-5237. <https://doi.org/10.1002/mp.16432>

2.3 Paper III

Dosimetric study for breathing-induced motion effects in an abdominal pancreas phantom for carbon ion mini-beam radiotherapy

Authors: Christina Stengl*, Ivan D. Munoz, Eric Arbes, Evelyn Rauth, Jeppe B. Christensen, José Vedelago, Armin Runz, Oliver Jäkel, Joao Seco

*Corresponding author.

Journal reference: Med. Phys., 2024

DOI: 10.1002/mp.17077

Journal Impact Factor: 3.8

Source: <https://aapm.onlinelibrary.wiley.com/journal/24734209/journal-metrics>, accessed on 24 May 2024.



Received: 30 November 2023 | Revised: 14 March 2024 | Accepted: 2 April 2024

DOI: 10.1002/mp.17077

RESEARCH ARTICLE

MEDICAL PHYSICS

Dosimetric study for breathing-induced motion effects in an abdominal pancreas phantom for carbon ion mini-beam radiotherapy

Christina Stengl^{1,2,3} | Iván D. Muñoz^{2,3,4} | Eric Arbes^{4,5} | Evelyn Rauth^{4,5} |
Jeppe B. Christensen⁶ | José Vedelago^{2,3,7} | Armin Runz^{2,3} |
Oliver Jäkel^{2,3,8} | Joao Seco^{4,5}

¹Medical Faculty Heidelberg, Heidelberg University, Heidelberg, Germany

²Division of Medical Physics in Radiation Oncology, German Cancer Research Center (DKFZ), Heidelberg, Germany

³Heidelberg Institute for Radiation Oncology (HIRO), National Center for Radiation Research in Oncology (NCRO), Heidelberg, Germany

⁴Department for Physics and Astronomy, Heidelberg University, Heidelberg, Germany

⁵Biomedical Physics in Radiation Oncology, German Cancer Research Center (DKFZ), Heidelberg, Germany

⁶Department of Radiation Safety and Security, Paul Scherrer Institute (PSI), Villigen, Switzerland

⁷Department of Radiation Oncology, Heidelberg University Hospital (UKHD), Heidelberg, Germany

⁸Heidelberg Ion Beam Therapy Center (HIT), Department of Radiation Oncology, Heidelberg University Hospital (UKHD), Heidelberg, Germany

Correspondence

Christina Stengl, Medical Faculty Heidelberg, Heidelberg University, Im Neuenheimer Feld 672, Heidelberg D-69120, Germany.
Email: christina.stengl@dkfz.de

Oliver Jäkel and Joao Seco share the last authorship

Funding information

Helmholtz Association; Deutscher Akademischer Austauschdienst, Grant/Award Number: 57440921

Abstract

Background: Particle mini-beam therapy exhibits promise in sparing healthy tissue through spatial fractionation, particularly notable for heavy ions, further enhancing the already favorable differential biological effectiveness at both target and entrance regions. However, breathing-induced organ motion affects particle mini-beam irradiation schemes since the organ displacements exceed the mini-beam structure dimensions, decreasing the advantages of spatial fractionation.

Purpose: In this study, the impact of breathing-induced organ motion on the dose distribution was examined at the target and organs at risk (OARs) during carbon ion mini-beam irradiation for pancreatic cancer.

Methods: As a first step, the carbon ion mini-beam pattern was characterized with Monte Carlo simulations. To analyze the impact of breathing-induced organ motion on the dose distribution of a virtual pancreas tumor as target and related OARs, the anthropomorphic Pancreas Phantom for Ion beam Therapy (PPIeT) was irradiated with carbon ions. A mini-beam collimator was used to deliver a spatially fractionated dose distribution. During irradiation, varying breathing motion amplitudes were induced, ranging from 5 to 15 mm. Post-irradiation, the 2D dose pattern was analyzed, focusing on the full width at half maximum (FWHM), center-to-center distance (ctc), and the peak-to-valley dose ratio (PVDR).

Results: The mini-beam pattern was visible within OARs, while in the virtual pancreas tumor a more homogeneous dose distribution was achieved. Applied

This is an open access article under the terms of the [Creative Commons Attribution-NonCommercial](https://creativecommons.org/licenses/by-nc/4.0/) License, which permits use, distribution and reproduction in any medium, provided the original work is properly cited and is not used for commercial purposes.

© 2024 The Authors. *Medical Physics* published by Wiley Periodicals LLC on behalf of American Association of Physicists in Medicine.

Med Phys. 2024;1–14.

wileyonlinelibrary.com/journal/mp | 1

motion affected the mini-beam pattern within the kidney, one of the OARs, reducing the PVDR from 3.78 ± 0.12 to 1.478 ± 0.070 for the 15 mm motion amplitude. In the immobile OARs including the spine and the skin at the back, the PVDR did not change within 3.4% comparing reference and motion conditions.

Conclusions: This study provides an initial understanding of how breathing-induced organ motion affects spatial fractionation during carbon ion irradiation, using an anthropomorphic phantom. A decrease in the PVDR was observed in the right kidney when breathing-induced motion was applied, potentially increasing the risk of damage to OARs. Therefore, further studies are needed to explore the clinical viability of mini-beam radiotherapy with carbon ions when irradiating abdominal regions.

KEYWORDS

breathing-induced motion, mini-beam irradiation, pancreas phantom, spatial fractionation

1 | INTRODUCTION

Carbon ion radiotherapy (CIRT) has attracted increasing interest due to its unique physical and radiobiological characteristics during the last decade.^{1,2} In comparison to conventional photon radiotherapy, CIRT demonstrates increased dose conformity and enhanced relative biological effectiveness (RBE).^{3,4} Abdominal tumors, such as pancreatic cancer, have shown improved radio-oncological outcomes with CIRT, as demonstrated by a Japanese multi-institutional study indicating a substantial increase in median overall survival from around 1 to 2 years.⁵ Due to the absence of standardized beam configurations for pancreatic cancer treatment with carbon ions, various plans have been implemented across different centers. These plans may include two, three, or even four beams, based on the experience and RBE models used.^{6–11}

However, carbon ion irradiation can result in higher damage to normal tissue, particularly in the entrance region of the beam when compared to lighter ions. This could potentially elevate the risk of secondary cancer.^{12–14} New technologies such as mini-beam radiotherapy (MBRT) aim for reduced normal tissue damage in the entrance channel. Hence, integrating MBRT with CIRT presents a promising prospect, combining the advantages of both techniques.^{13,14}

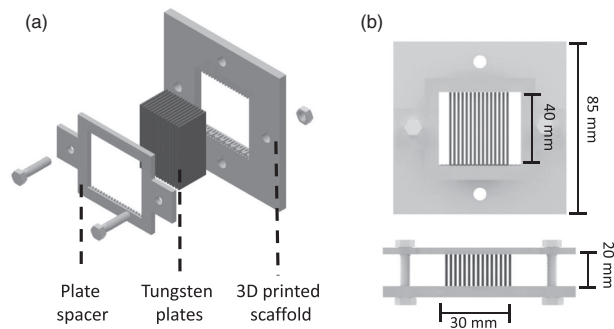
MBRT is a novel treatment modality based on the creation of a distinctive dose profile consisting of neighboring peak and valley regions characterized by high and low doses, respectively.^{15,16} This allows not only tumor control but also a high level of normal tissue preservation. Usually, the mini-beam pattern can be achieved by a mini-beam collimator. Hence, metal structures ranging from 1 to 4 mm form the valley and are separated by air with a thickness of 0.2 to 1 mm to create the peak.^{17–19} The important geometrical parameters used to describe the mini-beam pattern are the full width at half maximum (FWHM), representing the width of individual beams, and the center-to-center distance

(ctc), representing the distance between successive peaks. The peak-to-valley dose ratio (PVDR) serves as an important biologically relevant parameter, with a higher PVDR favoring the sparing of normal tissue.²⁰

Both, MBRT and CIRT techniques, offer potential advantages over conventional photon radiotherapy. Preclinical studies on MBRT using protons have demonstrated a reduction in side effects in normal tissue while effectively controlling the tumor.^{12,21,22} Additionally, CIRT has shown superior cancer outcomes in phase 1 and 2 human trials across various malignancies, including head and neck tumors, non-small cell lung cancer, and prostate carcinoma.^{23,24} The combination of CIRT and MBRT, termed ion mini-beam radiation therapy (iMBRT), was initially explored by Dilmanian et al.²⁵ Their study, conducted on rabbit brains, reported no cognitive damage following iMBRT treatment, suggesting the potential for healthy tissue sparing.

Nevertheless, the scope of preclinical testing of MBRT and iMBRT has been primarily confined to cranial anatomical regions of animal models, resulting in limited knowledge concerning the treatment of moving volumes in humans, especially when dealing with organs like the liver and pancreas.^{12,22,25,26} Although efforts have been made to simulate mini-beam radiation on a non-deformable and anthropomorphic phantom to evaluate lung tumor treatments,²⁷ the data on motion effects remains limited. This limitation exists despite the recognized susceptibility of both MBRT and CIRT to errors induced by motion, leading to uncertainties in dose delivery.^{2,28,29} Although it has been already demonstrated that the mini-beam pattern does not blur within the murine brain due to heartbeat and breathing motion,¹⁷ the excess of tumor and OAR motion in the abdomen of humans with significantly larger dimensions have not been studied yet. In humans, the lengths of the breathing-induced organ motion can easily exceed the FWHM and ctc of the mini-beams,^{30–33} directly affecting the dose delivery and potentially reducing the iMBRT advantages.

FIGURE 1 Exploded-view rendering of the collimator with a 3D-printed scaffold to position the tungsten plates 1 mm apart from each other and the plate spacer to guarantee correct plate positioning (a). Rendering of the collimator from top and side views with dimensions (b).



To assess the effects of motion, anthropomorphic phantoms are a valuable tool for conducting tests without subjecting patients or animals to harm during treatment. Numerous breathing motion phantoms with varying degrees of anthropomorphism have been developed thus far.^{34–37} Only recently, an anthropomorphic abdomen phantom with a breathing motion feature was developed which enables the measurement of simultaneous effects within the target and the OARs.³⁷

This work aims to investigate the impact of breathing-induced motion on the mini-beam pattern when treating a virtual pancreas tumor with carbon iMBRT. The previously mentioned anthropomorphic abdominal phantom was used to reproduce breathing-induced organ motions from 5 to 15 mm during irradiation. The mini-beam pattern was quantified using FWHM, etc, and PVDR in the virtual pancreas tumor and its OARs, namely skin, kidney, and spine.

2 | METHODS

2.1 | Mini-beam collimator for carbon iMBRT

To investigate carbon iMBRT it is necessary to use a suitable mini-beam collimator. In this study, the mini-beam collimator consisted of 15 tungsten plates with a size of $(40 \times 20 \times 1) \text{ mm}^3$ that were positioned parallel to each other in a 3D-printed scaffold, with a 1 mm gap of air in between them (Figure 1). A similar design was presented in a previous publication³⁸ but the mini-beam collimator was adapted for carbon ions. One of the major changes was adjusting the height of the tungsten plates from 10 to 20 mm. For this, the maximum energy previously used in the pancreatic cancer treatment plan,³⁷ namely carbon ions with 291.34 MeV/u, was considered as the maximum energy that needs to be attenuated by the mini-beam collimator to theoretically

achieve no radiation in the valleys. Carbon ions with that energy have a range of approximately 16 mm in tungsten.³⁹ As a conservative size, the mini-beam collimator was constructed using tungsten plates with a height of 20 mm. This ensures that the primary carbon ions are fully attenuated in the tungsten plates, leading to the valley regions. The dose in the peak regions is generated by the primary carbon ions traveling through the air gaps in between the tungsten plates. To ensure the 1 mm distance between the tungsten plates, a 3D-printed plate spacer was attached to the collimator, holding the plates precisely aligned in parallel with each other.

2.2 | Anthropomorphic phantom PPIeT

The Pancreas Phantom for Ion beam Therapy (PPIeT), designed to evaluate dose distribution in the pancreas and related OARs, was used to resemble the human abdomen during carbon iMBRT.³⁷ PPIeT is equipped with 3D-printed organs, each capable of hosting a 3D-printed insert that holds up to 4 EBT3 films. The film insert within the pancreas serves as the “virtual pancreas tumor” in this setup, with a volume of 22.4 cm^3 . For this study, 4 EBT3 dosimetric films were inserted in each organ insert, with a size of $(34 \times 23) \text{ mm}^2$ for the pancreas, $(37 \times 18) \text{ mm}^2$ for the kidney and $(29 \times 11) \text{ mm}^2$ for the spine.

The films were consecutively labeled as Film 1 to Film 4, with Film 1 positioned proximal to the beam entrance and Film 4 positioned distally. In addition, a $(30 \times 30) \text{ mm}^2$ film was attached to the skin in the position of the beam entrance. For the application of breathing motion, a Nema 23 stepper motor (EC Motion GmbH, Germany) and a linear stage (igus GmbH, Germany) were coupled to a 3D-printed actuator to press on the flexible diaphragm to induce motion into the internal organs. The system was controlled by Twincat version 3 using a PLC CX5020 (Beckhoff Information

TABLE 1 Main irradiation parameters used for carbon iMBRT in the treatment plan for PPIeT.

Parameter	Beam 1	Beam 2
Step size (mm)	3.6 (hexagonal)	3.6 (hexagonal)
Focus (mm)	from 10.0 to 10.3	from 10.0 to 10.2
Energy (MeV/u)	from 226.05 to 278.29	from 229.76 to 291.34
Energy step (mm)	3.1	3.1
Number energy layers	16	19

Abbreviations: iMBRT, ion mini-beam radiation therapy; PPIeT, pancreas phantom for ion beam therapy.

Systems, Germany) and sinusoidal breathing motions were applied with different input motion amplitudes. The resulting breathing-induced organ motion had motion amplitudes of 5, 10, and 15 mm as described in a previous study.³⁷ In the present study, the static condition where no motion was applied is called the “reference” condition.

2.3 | Carbon iMBRT for PPIeT

Carbon iMBRT was performed at the Heidelberg Ion Therapy Center with a scanned carbon ion beam (HIT; Heidelberg, Germany).^{40–42} A treatment plan for the virtual pancreas tumor was calculated in RayStation 11B, version 12.0.0.932 (RaySearch Laboratories, Sweden). The plan prescribed a consistent dose of 4.00 Gy (RBE), equivalent to 1.37 Gy physical dose, within the planning target volume (PTV), represented by the virtual pancreas tumor.³⁷ The dose grid was defined with a 2 mm isotropic spacing, utilizing a 3.6 mm hexagonal spot spacing, and maintaining a 3.1 mm spacing between energy layers. The plan included two beams from two angles, namely at 250° (Beam 1) and at 290° (Beam 2), to resemble an actual patient treatment plan for carbon ion pancreas irradiation. PPIeT was irradiated on a rotation table with the mini-beam collimator positioned 50 mm apart from the phantom’s surface (Figure 2a). The main parameters for both beams are summarized in Table 1 and further information is given in Tables S1 and S2. For Beam 1, the skin, the kidney, and the pancreas were at depths of 0, 45, and 120 mm from the entrance, respectively. For Beam 2, the spine and pancreas were at depths of 40 and 120 mm from the beam entrance, respectively (Figure 2b). Films inside the dosimetric inserts within each of the organs were always irradiated with the complete plan, including the two beams. Measurements were conducted three times independently with the setup shown in Figure 2c,d, and the mean as well as the standard deviation were calculated for each condition.

To compare the results obtained with PPIeT, mini-beam dose profiles were measured in a simplified and geometrical phantom. For this, a (300 × 300 ×

150) mm³ RW3 phantom (PTW, Germany) was irradiated with the mini-beam collimator 50 mm apart from the RW3 plates. Films were placed within this phantom at depths of {0; 40; 45; 120} mm, representing the position of the skin, the spine, the right kidney, and the pancreas of PPIeT, respectively.

2.4 | Film dosimetry for carbon ions

To analyze the dose distribution induced by the mini-beam collimator in carbon iMBRT, EBT3 radiochromic films (Ashland, USA) were used in PPIeT within the skin, the spine, the right kidney, and the virtual pancreas tumor. To perform film dosimetry, a calibration curve was acquired for each of the four measurement depths using the RW3 phantom. A detailed description of the methodology used for the calibration of the films is included in Section S.II. “Film calibration for carbon ion beam dosimetry” and Table S3.

The films were read out 24 h after irradiation⁴³ using an Epson scanner 10 000 (Epson, Japan) in landscape mode with 300 dpi after scanner warm-up for 1 h. No color corrections were applied during the scan. The optical density (OD) values were calculated from the red channel of each film. For each depth, namely {0; 40; 45; 120} mm, the corresponding calibration curve was used to calculate the dose from the OD values for each organ (Figure S1).

For the mini-beam pattern analysis, the mean of 20 pixels in the direction perpendicular to the carbon iMBRT structure was used to compute a mean dose profile. Afterwards, the mini-beam parameters, FWHM, ctc, and PVDR, were calculated for each mini-beam profile.

2.5 | Monte Carlo simulations

To further characterize the mini-beam dose pattern in depth and compare it with the mini-beam parameters achieved experimentally, Monte Carlo (MC) simulations were done with the MC particle transport toolkit TOPAS. The dose and linear energy transfer (LET) distributions were computed with TOPAS. The simulation parameters are detailed in Table S4 following the American Association of Physicists in Medicine (AAPM) recommendations.⁴⁴ Previously, the TOPAS model of the beam nozzle as well as the scoring of dose and LET underwent experimental validations against ionization chamber measurements.⁴⁵ The simulations were run with and without the mini-beam collimator placed in front of the phantom. The dose-averaged LET (LET_d) was calculated following the averaging approach defined in Method C.⁴⁶ Electrons and particles heavier than the primary particle were excluded from the LET averaging.

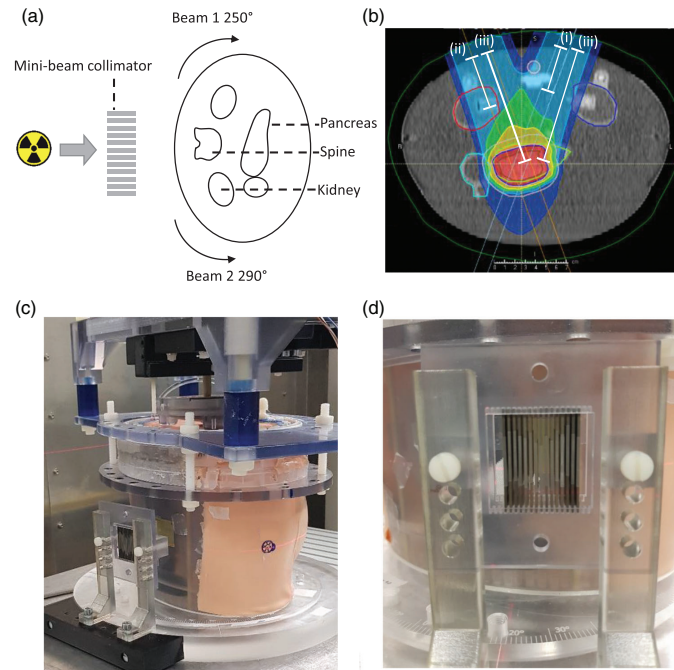


FIGURE 2 Setup for carbon iMBRT in PPIeT. PPIeT is rotated to 250° or 290° for Beam 1 and Beam 2, respectively (a). Treatment plan for PPIeT in the axial plane, showing the pancreas as target, the right kidney (red outline), left kidney (blue outline), spinal cord (orange outline), and the duodenum (light blue outline). The white lines indicate the distance from the beam entrance into PPIeT to the examined organs including the spine ((i): 40 mm), the right kidney ((ii): 45 mm), and the pancreas ((iii): 120 mm) for each beam (b). Experimental setup with PPIeT and the mini-beam collimator in front of the back (c). Detailed close-up view of the mini-beam collimator in front of the phantom (d). iMBRT, ion mini-beam radiation therapy; PPIeT, pancreas phantom for ion beam therapy.

3 | RESULTS

3.1 | Monte Carlo simulation for carbon iMBRT

To compare the mini-beam parameters FWHM, etc, and PVDR, obtained from the film measurements in PPIeT, MC simulations for carbon iMBRT were conducted. The dose distributions were simulated at the four depths in the RW3 phantom, namely at 0, 40, 45, and 120 mm corresponding to the skin, the spine, the kidney, and the pancreas positions in PPIeT, respectively (Figure 3).

As illustrated in Figure 3a, the broadening of the mini-beams is visible starting from approximately 100 mm depth. By analyzing the profiles, a distinct mini-beam pattern was achieved for Beam 1, Beam 2, and the sum of the two of them. The mini-beam profiles at each depth reflect the spatial fractionated dose distribution,

with similar values for the profiles at 0 and 45 mm corresponding to Beam 1, and the profile at 45 mm for Beam 2. The profile at 120 mm presented overall higher values, with peak dose values roughly two times larger than those of the other profiles (Figure 3b).

In addition, the LET_d was computed to support the film calibrations at each depth. For the three shallower film calibration depths, namely 0, 40, and 45 mm, the variation of the calculated LET_d was found to be below 10.8% (Figure S2). The LET_d increased towards the end of the SOBP. At a depth of 120 mm, it has a mean value 76.2% higher than at the three shallower depths. This trend agrees with the experimentally obtained calibration curves of the films since almost the same dose responses were found for the three shallower depths but a reduced response was observed for 120 mm (Figure S1). Moreover, the consistent trend in the LET_d supports the use of the calibration curves

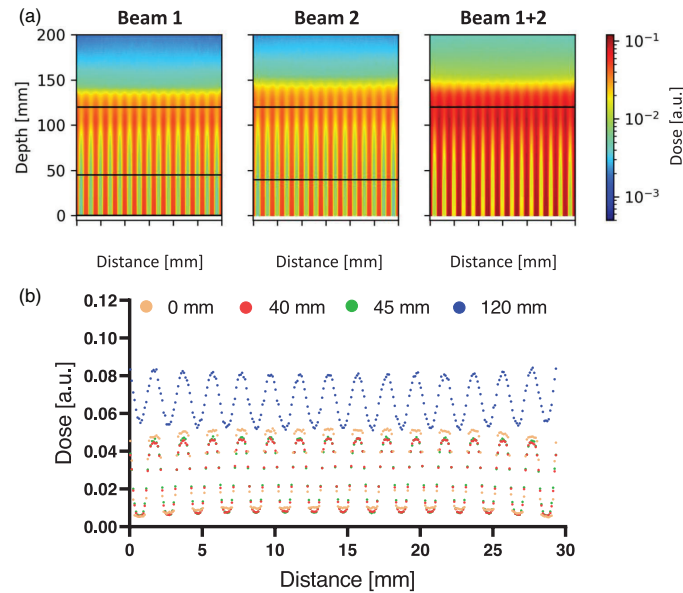


FIGURE 3 2D mini-beam pattern obtained with the MC simulations for Beam 1, Beam 2 and the sum of the two of them (a). Mini-beam dose profiles at depths of 0 mm (orange), 40 mm (red), 45 mm (green), and 120 mm (blue) (b). The horizontal black lines in (a) indicate the profiles for each depth plotted in (b).

conducted at each depth, accounting for the quenching in the response of the films. Consequently, the results of the film measurements done in PPIeT are reported in absolute dose values.

3.2 | Mini-beam dose profiles within the organs of PPIeT

To assess the uniformity of the mini-beam profiles within the spine, kidney, and pancreas in PPIeT, four films with increasing distance to the phantom surface were analyzed (Figure 4). In the spine, there was no significant difference in the PVDR between Film 1, Film 2, and Film 3. A significant decrease in the PVDR of 9.21% was observed from Film 1 to Film 4 ($p = 0.0034$, one-way ANOVA) (Figure 4a). Within the kidney, the mini-beam pattern is also visible in the four films with no significant variations of the PVDR values over depth (Figure 4b).

The peak and valley structure of the mini-beam pattern in the virtual pancreas tumor is less prominent in Film 1 compared with the pattern of the OARs, and it broadens with increased distance to the phantom surface from Film 2 to Film 4 (Figure 4c), aligning with the intended outcome for carbon iMBRT. The PVDR

was only calculated for Film 1 yielding a value of (1.084 ± 0.039) . The average peak dose for Film 1, measuring (0.841 ± 0.085) Gy, constitutes 61.4% of the intended physical dose of 1.37 Gy for the virtual pancreas tumor. This aligns with the results from MC simulations, showing that the mean peak dose is 61.3% of the mean dose without the mini-beam collimator (Figure S3).

Comparing the mini-beam parameters FWHM, ctc, and PVDR for the measurements in PPIeT with the MC simulation and independent film measurements done in the RW3 phantom, a general alignment in the trends for all the mentioned parameters was observed (Figure 5). The FWHM showed a slight increase from 0 to 120 mm depth but consistently remained around the expected 1 mm. The ctc consistently measured around 2 mm, in line with the mini-beam collimator geometry expectations. For the PVDR, the MC simulations indicated an increased PVDR for each depth, but comparable to the experimental values, whereas no differences were found between the measurements done in the RW3 phantom and the organs of PPIeT. Overall, these findings support the experimental estimation of the mini-beam parameters using the film dosimetry in PPIeT for assessing the impact of breathing-induced organ motion in the FWHM, ctc, and PVDR.

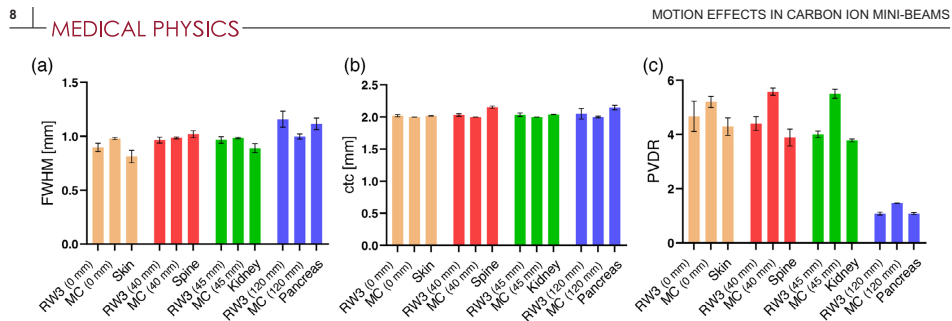


FIGURE 5 Comparison of mini-beam parameters for the measurement in the RW3 phantom, the MC simulations and the measurement done in PPlEt, including FWHM (a), ctc (b), and PVDR (c). ctc, center-to-center distance; PPlEt, pancreas phantom for ion beam therapy; FWHM, full width at half maximum; PVDR, peak-to-valley dose ratio.

3.3 | Breathing-induced organ motion impact on the mini-beam pattern

The impact of breathing-induced organ motion on the mini-beam pattern within the organs was assessed with films by varying the motion amplitudes, and the results were compared to the reference condition where no motion was applied (Figure S4). Within the film positioned at the skin on the surface of the PPlEt, the peak and valley areas can be distinguished showing a reproducible pattern (Figure 6a). The FWHM mean value of (0.813 ± 0.058) mm and the ctc mean value of (2.0176 ± 0.0018) mm for reference condition aligned with the mini-beam collimator design. With increasing motion amplitude, these parameters remained stable, exhibiting differences lower than 5.2% and 0.3%, respectively. The mean PVDR in the reference condition was (4.29 ± 0.32) and remained consistent within a margin of 3.2% when motion was applied (Figure 6b).

Similar to the skin, the spine is an immobile organ, and therefore, breathing-induced motion has almost no impact on the mini-beam pattern (Figure 6c). The FWHM in the reference condition measured (1.020 ± 0.032) mm and remained unaffected by motion, with differences below 2.8%. Similarly, the ctc with a value of (2.154 ± 0.018) Gy for the reference condition, did not exhibit changes with varying motion amplitudes, staying within differences below 0.4%. The PVDR measured (3.89 ± 0.31) for the reference condition and did not change significantly during motion application (Figure 6d).

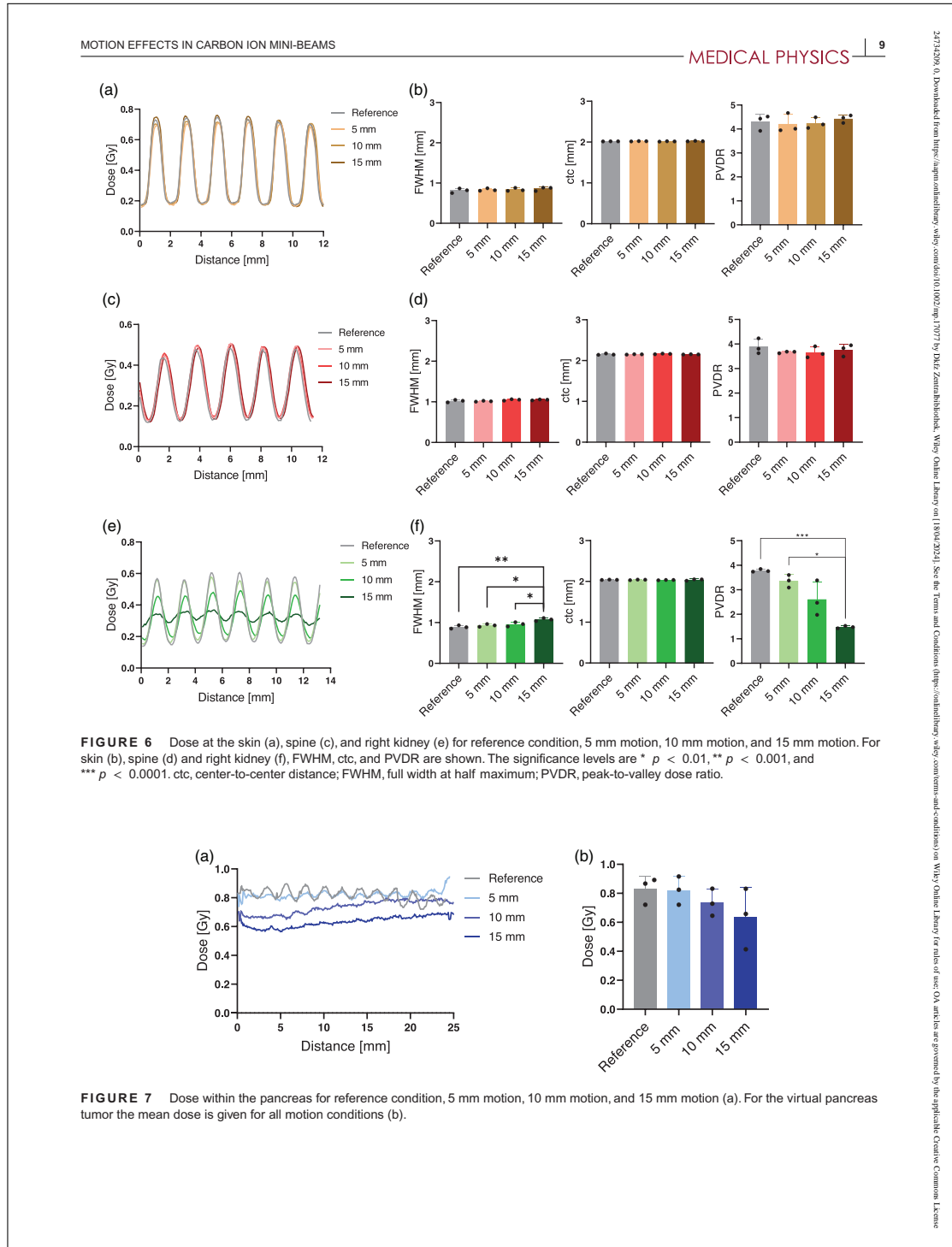
In contrast, the kidney is a mobile organ where breathing-induced motion has a greater impact on the mini-beam pattern (Figure 6e). Within the mini-beam pattern of the kidney films, the mean FWHM was (0.899 ± 0.041) mm, (0.930 ± 0.034) mm, (0.960 ± 0.056) mm, and (1.06 ± 0.11) mm for reference condition, 5 mm motion, 10 mm motion, and 15 mm motion, respectively. Therefore, the FWHM increased

significantly from the reference condition to the 15 mm motion by 19.4% ($p = 0.0029$, one-way ANOVA), indicating the broadening and blurring of the mini-beam pattern. The ctc matched the given mini-beam collimator structure and did not change within 1.4%. The PVDR decreased with increasing motion amplitude resulting in (3.783 ± 0.056) , (3.36 ± 0.26) , (2.61 ± 0.71) , and (1.478 ± 0.051) for reference condition, 5 mm motion, 10 mm motion, and 15 mm motion, respectively. Notably, a significant difference of 60.9% was observed between the reference condition and the 15 mm motion condition ($p = 0.0011$, one-way ANOVA) (Figure 6f).

In the pancreas, the mini-beam pattern exhibited increasing blurring with motion, while the mean dose decreased. For the reference condition, a FWHM of (1.115 ± 0.054) mm, a ctc of (2.149 ± 0.035) mm, a PVDR of (1.084 ± 0.039) and a mean dose of (0.827 ± 0.092) Gy was measured. For the motion conditions, no clear mini-beam pattern was observed, therefore it was not possible to quantify the FWHM, ctc, and PVDR. The mean dose decreased by 2.4%, 12.6%, and 24.6%, for 5 mm motion, 10 mm motion, and 15 mm motion, respectively (Figure 7).

4 | DISCUSSION

The exploration of proton and carbon iMBRT in pre-clinical animal studies has shown promising results.^{12,21,22} However, these experiments were mainly focused on the brain, neglecting the challenges posed by patient-specific respiratory-induced motion, which is larger in humans compared with rodents. To address these challenges, our study investigated the effects of breathing-induced organ motion during carbon-ion mini-beam irradiation. To the best of the authors' knowledge, this is the first study to apply a pancreatic cancer treatment plan for carbon ions on an anthropomorphic phantom with a breathing feature using a mini-beam collimator.



24713296, 0, Downloaded from https://onlinelibrary.wiley.com/doi/10.1002/hip.14771 by DKU Zentrallibrary, Wiley Online Library on [18/04/2024]. See the Terms and Conditions (https://onlinelibrary.wiley.com/terms-and-conditions) on Wiley Online Library for rules of use; OA articles are governed by the applicable Creative Commons License

4.1 | Mini-beam collimator for carbon iMBRT

The mini-beam collimator employed in this study is a versatile and cost-effective tool for spatial fractionation. Its composition of 3D printing and rectangular tungsten plates allows for easy adaptation to various experimental setups, making it resource- and time-efficient. Previously, components of this collimator were used in a recently published study, focusing on the variation of ctc and FWHM within the collimator itself by testing different collimator configurations.³⁸ For the adaptation of the presented collimator for carbon iMBRT, a new 3D-printed scaffold was designed, while tungsten plates maintained the same.

In this study, one mini-beam collimator configuration was used with tungsten plates of 1 mm width spaced by 1 mm air, serving as a proof-of-concept study. In future studies, other configurations can be examined, such as 2 mm tungsten spaced by 0.5 mm air. This exploration aims to understand the interplay of motion when using various collimator setups. Such investigations are essential when seeking agreement on standardized parameters for mini-beam irradiation to achieve successful treatment outcomes. This can also involve considering factors like beam size, collimator size, dose rate, and beam current to achieve the desired mini-beam effect.²⁶

Another possibility to change the mini-beam collimator is to replace the tungsten plates with brass, which might reduce the secondary neutron generation.⁴⁷ Secondary neutrons could be further decreased by magnetically focusing the carbon ion beam to shape the mini-beam pattern without a collimator, which is nowadays used for protons.^{14,48} However, in the current state, clinical beamlines are not capable of magnetically focused carbon ion beams specifically designed for mini-beam irradiation. Consequently, the only available option for generating mini-beam carbon ions is using a mini-beam collimator.¹⁴

4.2 | Carbon iMBRT quantification

Ionization chambers can provide precise absolute dosimetric measurements for carbon ions but are usually limited to one dimension.⁴⁹ 2D ion chamber arrays, like the OCTAVIUS (PTW, Freiburg, Germany)¹, are suitable for two-dimensional dose measurements, however, the spatial resolution of 2.5 mm is not enough for the used mini-beam collimator setup with 1 mm beam width.

Therefore, the mini-beam pattern was evaluated using EBT3 films, chosen based on their capability to

display two-dimensional distributions with high spatial resolution. However, the films used for carbon beam irradiation also have limitations, mainly the LET dependence of their response, leading to quenching of up to 60% in the Bragg peak region.^{50–52} While the LET change within the entrance region of the beam is negligible, it increases sharply towards the distal edge (Figure S2), leading to an under-response of the films. To address the quenching effect, particularly within the virtual pancreas tumor, calibration curves were established for the films at the specific depths (Figure S1), matching the depth of the organs inside PPIeT. In line with the MC simulations, the experimentally obtained dose calibration curve showed reduced sensitivity in the Bragg peak region, where the LET is higher (Figure S2). Despite this, the mean peak dose within the virtual pancreas tumor only represents 61.4% of the planned dose. This reduction is attributed to the mini-beam collimator, as confirmed by MC simulations, which consistently showed the same reduction in the presence of the collimator compared to the configuration without it (Figure S3).

An independent experimental validation of the film dosimetry was done with optically stimulated luminescent dosimeters (OSLDs)⁴⁵ within PPIeT, as explained in Section S.V. The OSLDs are capable of determining the dose and LET_d simultaneously.^{45,53} The agreement between the dosimetry with radiochromic films and OSLDs validates the mean peak dose values measured in the kidney and the spine (Figure S5). Corrected by the effect of having the mini-beam collimator, the mean peak dose value measured with the films matches the OSLD measurement and the previously reported measurement with a pinpoint ionization chamber.³⁷

4.3 | In-depth mini-beam parameters

FWHM, ctc, and PVDR were assessed numerically with the MC simulations and experimentally with the film measurements. For the measurements done with the RW3 phantom, the MC simulation, and the anthropomorphic phantom, a trend of increasing FWHM was observed for increasing depths. At the same time, the ctc remained constant and the PVDR decreased (Figure 5). The obtained results are in agreement with two previous studies.^{13,54} When comparing the values of the PVDR, the MC simulation demonstrated increased PVDRs compared to the experimentally obtained ones. This difference can be explained by the absence of angular spreading in the source particles of the simulations, which would decrease the primary particles reaching the peak and increase the number in the valley, hence decreasing the PVDR. Nonetheless, the consistent trend observed in the mini-beam parameter results underscores the feasibility of employing films in PPIeT to

¹ <https://www.ptwdosimetry.com/en/products/octavius-4d-qa-phantom>, accessed on 28 February 2024.

investigate the influence of organ motion caused by breathing on the mini-beam pattern.

In-depth measurements were not only conducted throughout the entire phantom but also within each specific organ. A trend of decreasing PVDR with increasing distance between the surface of the phantom and the position within the spine was found. A significant change in PVDR is observed from Film 1 to Film 4, which are 9 mm apart (Figure 4). In contrast, the mini-beam pattern within the kidney shows no significant change over a distance of 7 mm. These results indicate that the size of the volume to be treated has a direct impact on the mini-beam pattern within such a volume.

4.4 | Impact of motion on the mini-beam pattern

In general, it is important to consider the amplitude of the motion compared to the width of the peak and the valley when assessing the motion effect. Breathing-induced motion in animals, such as mice, is typically only a few millimeters for a tumor within the lung and even less in the brain.^{55,56} While mini-beam irradiation of the brain showed no significant impact due to breathing motion,¹⁷ micro-beam irradiation resulted in a 50% reduction in the PVDR.⁵⁷ In contrast, in humans, lung motion can reach up to 45.5 mm⁵⁸ and pancreas motion can be as high as 27.3 mm.^{30–33} When applying grid therapy to lung tumors with beam sizes of 10 mm, it becomes necessary to consider the motion of abdominal tumors in humans.⁵⁹ Therefore, even with smaller beam sizes, such as in mini-beams, the breathing motion of humans must be taken into consideration.

The present study with PPlE_T showed that immobilized organs resulted in no significant differences during the motion conditions. Instead, within the kidney the blurring of the mini-beam pattern was evident, as reported in the dose profiles for 15 mm motion (Figure 6). The resulting decreased PVDR could potentially reduce the effectiveness of the mini-beam irradiation.^{20,60–62} Also within the pancreas, the motion-induced blurring effect is visible with a low offset of only 5 mm organ motion. Within the target, the increased homogeneous tumor coverage might be beneficial for the tumor treatment.^{63,64}

One approach to mitigate the motion effect is using motion management systems, such as gating, already available in clinical settings. With this technique, the beam is delivered only within a specified breathing cycle amplitude window. Studies involving micro-beams and rodents have demonstrated that gating could significantly reduce blurring.⁵⁷ However, it is worth noting that this method

requires more treatment time compared to standard irradiation.⁶⁵

4.5 | Significance of iMBRT for the clinic

So far, MBRT and iMBRT, remain in the pre-clinical testing phase.⁶⁶ However, when comparing iMBRT with CIRT notable advantages emerge, particularly in terms of reduced radiation impact on the OARs. This reduction in radiation dose could potentially lead to either a decreased number of treatment fractions or an increase in the prescribed target dose without compromising the OARs.²⁵ A first randomized dog trial demonstrated that MBRT was superior to traditional fractionated photon treatment in terms of both tumor control and normal structure preservation.⁶⁷ Noteworthy these tests were conducted on immobilized organs, such as the brain, thus leaving the impact of motion unexplored.

The evaluation of the potential for a first clinical trial in humans was recently reported, where treatment plans for irradiation of metastases using proton mini-beams were studied.²⁸ Initial results are promising, as the integration of mini-beams into the treatment planning system indicates a reduction in the biologically effective dose of OARs, coupled with the simultaneous achievement of superior target coverage. However, Ortiz et al.²⁸ did not account for organ motion, which significantly increases the complexity of the problem. Employing an anthropomorphic phantom in combination with a mini-beam collimator, as done in this study with PPlE_T, has the potential to enhance research in this domain, providing a more comprehensive perspective on the impact of motion.

5 | CONCLUSION

This is the first anthropomorphic phantom study to evaluate motion effects for carbon iMBRT. These findings are more closely applicable to human breathing compared to mini-beam patterns in animal measurements. The observed mini-beam patterns under reference conditions revealed a homogeneous dose distribution in the virtual pancreas tumor and a well-defined mini-beam pattern in the OARs, showing the potential to successfully cover the tumor while sparing healthy tissue.

The mini-beam pattern in the immobilized organs was not affected by the 15 mm amplitude breathing-induced motion, since the mini-beam parameters FWHM, etc. and PVDR remained constant within the immobilized organs. However, the mini-beam pattern is altered within the moving organs, as evidenced by a decrease in the PVDR by up to 60.9%, particularly in

the kidney. The decreased PVDR suggests a potential increase in damage to the OARs.

This research highlights the value of employing an anthropomorphic phantom as a necessary tool for evaluating how breathing-induced organ motion affects the mini-beam pattern across diverse organs, including the tumor site and OARs. To achieve a more comprehensive understanding of the mini-beam effect during motion, further studies are needed, including experiments with different mini-beam configurations to assess potential dependencies.

ACKNOWLEDGMENTS

The authors would like to express their gratitude to Stephan Brons and Alexander Neuholz from HIT for their help with the irradiation. Additionally, C.S. acknowledges the funding from the Helmholtz graduate school for cancer research of the DKFZ, within their PhD program. I.D.M. acknowledges funding from DAAD (Research Grants-Doctoral Programs in Germany, program number: 57440921).

CONFLICT OF INTEREST STATEMENT

The authors have no conflicts to disclose.

ORCID

Christina Stengl 

<https://orcid.org/0000-0003-0273-0878>

Iván D. Muñoz 

<https://orcid.org/0000-0001-5183-3705>

Eric Arbes  <https://orcid.org/0000-0001-8498-2600>

Evelyn Rauth 

<https://orcid.org/0009-0004-0239-4725>

Jeppe B. Christensen 

<https://orcid.org/0000-0002-6894-381X>

José Vedelago 

<https://orcid.org/0000-0001-5510-9749>

Oliver Jäkel  <https://orcid.org/0000-0002-6056-9747>

REFERENCES

- Tinganelli W, Durante M. Carbon ion radiobiology. *Cancers*. 2020;12:3022.
- Malouff TD, Mahajan A, Krishnan S, Beltran C, Seneviratne DS, Trifiletti DM. Carbon ion therapy: a modern review of an emerging technology. *Front Oncol*. 2020;10:82.
- Weyrather WK, Kraft G. RBE of carbon ions: experimental data and the strategy of RBE calculation for treatment planning. *Radiother Oncol*. 2004;73:S161-S169.
- Karger CP, Peschke P. RBE and related modeling in carbon-ion therapy. *Phys Med Biol*. 2017;63:01TR02.
- Kawashiro S, Yamada S, Okamoto M, et al. Multi-institutional study of carbon-ion radiotherapy for locally advanced pancreatic cancer: Japan carbon-ion radiation oncology study group (J-CROS) study 1403 pancreas. *Int J Radiat Oncol Biol Phys*. 2018;101:1212-1221.
- Hagiwara Y, Bhattacharyya T, Matsufuji N, et al. Influence of dose-averaged linear energy transfer on tumour control after carbon-ion radiation therapy for pancreatic cancer. *Clin Transl Radiat Oncol*. 2019;21:19-24.
- Liermann J, Naumann P, Weykamp F, Hoegen P, Debus J, Herfarth K. Effectiveness of carbon ion radiation in locally advanced pancreatic cancer. *Front Oncol*. 2021;11:708884.
- Liermann J, Ben-Josef E, Syed M, Debus J, Herfarth K, Naumann P. Carbon ion radiotherapy as definitive treatment in locally recurrent pancreatic cancer. *Strahlenther Onkol*. 2022;198:378-387.
- Baltazar F, Tessonnier T, Haberer T, et al. Carbon-ion radiotherapy (CIRT) as treatment of pancreatic cancer at HIT: initial radiation plan analysis of the prospective phase II PACK-study. *Radiother and Oncol*. 2023;188:109872.
- Okamoto M, Shiba S, Kobayashi D, et al. Carbon-ion radiotherapy combined with concurrent chemotherapy for locally advanced pancreatic cancer: a retrospective case series analysis. *Cancers*. 2023;15:2857.
- Wang W, Sun J, Zhao J, Cheng J, Jiang GL, Wang Z. Up modulation of dose-averaged linear energy transfer by simultaneous integrated boost in carbon-ion radiotherapy for pancreatic carcinoma. *J Appl Clin Med Phys*. 2024;e14279. doi:10.1002/acm2.14279
- Girst S, Greubel C, Reindl J, et al. Proton minibeam radiation therapy reduces side effects in an in vivo mouse ear model. *Int J Radiat Oncol Biol Phys*. 2016;95:234-241.
- Martinez-Rovira I, González W, Brons S, Prezado Y. Carbon and oxygen minibeam radiation therapy: an experimental dosimetric evaluation. *Med Phys*. 2017;44:4223-4229.
- Volz L, Reidel CA, Durante M, et al. Investigating slit-collimator-produced carbon ion minibeam with high-resolution CMOS sensors. *Instruments*. 2023;7:18.
- Dilmanian FA, Eley JG, Krishnan S. Minibeam therapy with protons and light ions: physical feasibility and potential to reduce radiation side effects and to facilitate hypofractionation. *Int J Radiat Oncol Biol Phys*. 2015;92:469-474.
- Schneider T. Technical aspects of proton minibeam radiation therapy: minibeam generation and delivery. *Physica Med*. 2022;100:64-71.
- Bazyar S, Inscoe CR, O'Brian ET, Zhou O, Lee YZ. Minibeam radiotherapy with small animal irradiators: in vitro and in vivo feasibility studies. *Phys Med Biol*. 2017;62:8924.
- Treibel F, Nguyen M, Ahmed M, et al. Establishment of microbeam radiation therapy at a small-animal irradiator. *Int J Radiat Oncol Biol Phys*. 2021;109:626-636.
- Prezado Y, Dos Santos M, Gonzalez W, et al. Transfer of minibeam radiation therapy into a cost-effective equipment for radiobiological studies: a proof of concept. *Sci Rep*. 2017;7:17295.
- Dilmanian FA, Button TM, Le Duc G, et al. Response of rat intracranial 9L gliosarcoma to microbeam radiation therapy. *Neuro-Oncol*. 2002;4:26-38.
- Prezado Y, Jouvion G, Patriarca A, et al. Proton minibeam radiation therapy widens the therapeutic index for high-grade gliomas. *Sci Rep*. 2018;8:16479.
- Bertho A, Ortiz R, Juchaux M, et al. First evaluation of temporal and spatial fractionation in proton minibeam radiation therapy of glioma-bearing rats. *Cancers*. 2021;13:4865.
- Lazar AA, Schulte R, Faddegon B, Blakely EA, Roach M. Clinical trials involving carbon ion radiation therapy and the path forward. *Cancer*. 2018;124:4467-4476.
- Tsuji H, Mizoe JE, Kamada T, et al. Overview of clinical experiences on carbon ion radiotherapy at NIRS. *Radiother Oncol*. 2004;73 (Suppl 2):S41-S49.
- Dilmanian FA, Eley JG, Rusek A, Krishnan S. Charged particle therapy with mini-segmented beams. *Front Oncol*. 2015;5:269.
- Datzmann G, Sammer M, Girst S, Mayerhofer M, Dollinger G, Reindl J. Preclinical challenges in proton minibeam radiotherapy: physics and biomedical aspects. *Front Phys*. 2020;8:568206.

27. Zeinali-Rafsanjani B, Mosleh-Shirazi MA, Haghghatafshar M, Jalli R, Saeedi-Moghadam M. Assessment of the dose distribution of minibeam radiotherapy for lung tumors in an anthropomorphic phantom: a feasibility study. *Technol Health Care*. 2017;25:683-692.
28. Ortiz R, Belshi R, De Marzi L, Prezado Y. Proton minibeam radiation therapy for treating metastases: a treatment plan study. *Med Phys*. 2023;50:2463-2473.
29. Mazal A, Prezado Y, Ares C, et al. FLASH and minibeam radiation therapy: the effect of microstructures on time and space and their potential application to proton therapy. *Br J Radiol*. 2020;93:20190807.
30. Bhasin DK, Rana SS, Jahagirdar S, Nagi B. Does the pancreas move with respiration? *J Gastroenterol Hepatol*. 2006;21:1424-1427.
31. Knybel L, Cvek J, Otahal B, et al. The analysis of respiration-induced pancreatic tumor motion based on reference measurement. *Radiat Oncol*. 2014;9:192.
32. Dolde K, Dávid C, Echner G, et al. 4DMRI-based analysis of inter- and intrafractional pancreas motion and deformation with different immobilization devices. *Biomed Phys Eng Express*. 2019;5:025012.
33. Jing S, Jiang C, Ji X, et al. Study on motion management of pancreatic cancer treated by CyberKnife. *Front Oncol*. 2021;11:767832.
34. Dunn L, Kron T, Johnston PN, et al. A programmable motion phantom for quality assurance of motion management in radiotherapy. *Australas Phys Eng Sci Med*. 2012;35:93-100.
35. Kim J, Lee Y, Shin H, et al. Development of deformable moving lung phantom to simulate respiratory motion in radiotherapy. *Med Dosim*. 2016;41:113-117.
36. Weidner A, Stengl C, Dinkel F, et al. An abdominal phantom with anthropomorphic organ motion and multimodal imaging contrast for MR-guided radiotherapy. *Phys Med Biol*. 2022;67:045009.
37. Stengl C, Panow K, Arbes E, et al. A phantom to simulate organ motion and its effect on dose distribution in carbon ion therapy for pancreatic cancer. *Phys Med Biol*. 2023;68:245013.
38. Stengl C, Arbes E, Thai LYJ, et al. Development and characterization of a versatile mini-beam collimator for pre-clinical photon beam irradiation. *Med Phys*. 2023;50:5222-5237.
39. Lühr A, Toftegaard J, Kantemiris I, Hansen DC, Bassler N. Stopping power for particle therapy: the generic library libdEdx and clinically relevant stopping-power ratios for light ions. *Int J Radiat Biol*. 2012;88(1-2):209-212.
40. Haberer T, Becher W, Scharf D, Kraft G. Magnetic scanning system for heavy ion therapy. *Nucl Instrum Methods Phys Res, Sect A*. 1993;330:296-305.
41. Haberer T, Debus J, Eickhoff H, Jäkel O, Schulz-Ertner D, Weber U. The heidelberg ion therapy center. *Radiat Oncol*. 2004;73:S186-S190.
42. Jäkel O, Kraft G, Karger CP. The history of ion beam therapy in Germany. *Z Med Phys*. 2022;32:6-22.
43. Niroomand-Rad A, Chiu-Tsao ST, Grams MP, et al. Report of AAPM task group 235 radiochromic film dosimetry: an update to TG-55. *Med Phys*. 2020;47:5986-6025.
44. Sechopoulos I, Rogers DWO, Bazalova-Carter M, et al. RECORDS: improved reporting of Monte Carlo radiation transport studies: report of the AAPM research committee task group 268. *Med Phys*. 2018;45:e1-e5.
45. Christensen JB, Muñoz ID, Bassler N, et al. Optically stimulated luminescence detectors for dosimetry and LET measurements in light ion beams. *Phys Med Biol*. 2023;68:155001.
46. Cortés-Giraldo MA, Carabe A. A critical study of different Monte Carlo scoring methods of dose average linear-energy-transfer maps calculated in voxelized geometries irradiated with clinical proton beams. *Phys Med Biol*. 2015;60:2645-2669.
47. Guardiola C, Peucelle C, Prezado Y. Optimization of the mechanical collimation for minibeam generation in proton minibeam radiation therapy. *Med Phys*. 2017;44:1470-1478.
48. Schneider T, De Marzi L, Patriarca A, Prezado Y. Advancing proton minibeam radiation therapy: magnetically focussed proton minibeam at a clinical centre. *Sci Rep*. 2020;10:1384.
49. Vedelago J, Karger CP, Jäkel O. A review on reference dosimetry in radiation therapy with proton and light ion beams: status and impact of new developments. *Radiation Measurements*. 2022;157:106844.
50. Castriconi R, Ciocca M, Mirandola A, et al. Dose-response of EBT3 radiochromic films to proton and carbon ion clinical beams. *Phys Med Biol*. 2017;62:377-393.
51. Martisková M, Jäkel O. Dosimetric properties of Gafchromic EBT films in monoenergetic medical ion beams. *Phys Med Biol*. 2010;55:3741-3751.
52. Yonai S, Arai C, Shimoyama K, Fournier-Bidoz N. Experimental evaluation of dosimetric characterization of gafchromic ebt3 and ebt-xd films for clinical carbon ion beams. *Radiat Prot Dosim*. 2018;180(1-4):314-318.
53. Christensen JB, Togno M, Bossin L, Pakari OV, Safai S, Yukihiro EG. Improved simultaneous LET and dose measurements in proton therapy. *Sci Rep*. 2022;12:8262.
54. González W, Peucelle C, Prezado Y. Theoretical dosimetric evaluation of carbon and oxygen minibeam radiation therapy. *Med Phys*. 2017;44:1921-1929.
55. Heyden B, Hoof SJ, Schyns LEJR, Verhaegen F. The influence of respiratory motion on dose delivery in a mouse lung tumour irradiation using the 4D MOBY phantom. *Br J Radiol*. 2017;90:20160419.
56. Hill M, Vojnovic B. Implications of respiratory motion for small animal image-guided radiotherapy. *Br J Radiol*. 2016;90:20160482.
57. Chtchevop P, Hadsell M, Burk L, et al. Physiologically gated micro-beam radiation therapy using electronically controlled field emission x-ray source array. *Proc SPIE-Int Soc Opt Eng*. 2013;8671:86711Z.
58. Kolar P, Neuwirth J, Sanda J, et al. Analysis of diaphragm movement during tidal breathing and during its activation while breath holding using MRI synchronized with spirometry. *Physiol Res*. 2009;58:383-392.
59. Naqvi SA, Mohiuddin MM, Ha JK, Regine WF. Effects of tumor motion in GRID therapy. *Med Phys*. 2008;35:4435-4442. doi:10.1118/1.2977538
60. Ortiz R, De Marzi L, Prezado Y. Preclinical dosimetry in proton minibeam radiation therapy: robustness analysis and guidelines. *Med Phys*. 2022;49:5551-5561.
61. Kim M, Hwang UJ, Park K, et al. Dose profile modulation of proton minibeam for clinical application. *Cancers*. 2022;14:2888.
62. Schneider T, Patriarca A, Prezado Y. Improving the dose distributions in minibeam radiation therapy: helium ions vs protons. *Med Phys*. 2019;46:3640-3648.
63. Kataria T, Sharma K, Subramani V, Karrthick KP, Bisht SS. Homogeneity index: an objective tool for assessment of conformal radiation treatments. *J Med Phys*. 2012;37:207-213.
64. Salimi M, Abi KST, Nedaie HA, et al. Assessment and comparison of homogeneity and conformity indexes in step-and-shoot and compensator-based intensity modulated radiation therapy (IMRT) and three-dimensional conformal radiation therapy (3D CRT) in prostate cancer. *J Med Signals Sens*. 2017;7:102-107.
65. Kini VR, Vedam SS, Keall PJ, Patil S, Chen C, Mohan R. Patient training in respiratory-gated radiotherapy. *Med Dosim*. 2003;28:7-11.
66. Mali SB. Mini review of spatially fractionated radiation therapy for cancer management. *Oral Oncology Reports*. 2024;9:100175.

67. Kundapur V, Mayer M, Auer RN, et al. Is mini beam ready for human trials? results of randomized study of treating de-novo brain tumors in canines using linear accelerator generated mini beams. *Radiat Res.* 2022;198:162-171.

SUPPORTING INFORMATION

Additional supporting information can be found online in the Supporting Information section at the end of this article.

How to cite this article: Stengl C, Muñoz ID, Arbes E, et al. Dosimetric study for breathing-induced motion effects in an abdominal pancreas phantom for carbon ion mini-beam radiotherapy. *Med Phys.* 2024;1-14. <https://doi.org/10.1002/mp.17077>

3. Discussion

In this thesis, an anthropomorphic abdomen phantom with breathing motion features for carbon ion radiotherapy of pancreatic cancer was developed. PPIeT is an in-house designed model comprising the pancreas with a virtual tumor in the pancreas head and critical OARs including the duodenum, the two kidneys, the spine and the spinal cord (**Paper I**). Additionally, a versatile mini-beam collimator was engineered for investigating various parameters in dosimetry and *in-vitro* studies including FWHM, etc and PVDR for photon irradiation (**Paper II**). Subsequently, the mini-beam collimator was adapted for CIRT, enabling the analysis of breathing-induced organ motion effects during iMBRT treatment for pancreatic cancer in PPIeT (**Paper III**).

3.1 3D printing for radiotherapy

3D printing served as a central technique in this thesis. In **Paper I**, the anthropomorphic organs of the phantom were fabricated using this technique. It allowed for the production of anatomically accurate organ shapes through computer-aided design software, making complex and customized structures feasible.

3D printing techniques

Two different 3D printing techniques were used for prototyping. First, the polyjet technique was employed, involving the layer-by-layer curing of a liquid photopolymer material using UV light, achieving high precision down to $18.75 \mu\text{m}$. This method allows for the combination of different materials within a single print, including mixtures of solid and flexible materials by using varying shore strengths. Furthermore, transparent resins like VeroClear (Stratasys, Israel) can be used to visualize the inner structures of a complex prototype³. Second, fused deposition modeling (FDM) was used, which operates by melting and depositing material through a nozzle, gradually constructing the desired shape layer by layer⁴. The materials from FDM printers are most often more durable compared to VeroClear

³<https://www.stratasys.com/en/stratasysdirect/technologies/3d-printing/polyjet/>, accessed on 20 April 2024.

⁴<https://www.stratasys.com/en/guide-to-3d-printing/technologies-and-materials/fdm-technology/>, accessed on 05 May 2024.

and offer high flexibility in available materials that differ in Hounsfield unit (HU) values. However, its applicability may be restricted for tasks demanding high spatial resolution due to the 330 μm layer thickness. With these two techniques, 3D printing offers versatility in material selection enabling the use of various printing material types with different properties within the phantom. These properties include features like different contrasts for CT and MRI and diverse flexibilities for simulating internal organ motion.

3D-printed parts for PPIeT

The pancreas and the two kidneys were printed with VeroClear using the polyjet technique (Stratasys, Israel, 3D printer J55). The majority of materials used with this technique have densities similar to PMMA, leading to comparable HU values like water. As a result, they do not provide different contrast for imaging purposes (Gear et al. 2016). One approach to introduce varying HU values for CT imaging and different T1 and T2 times for MR imaging of different organs is to print a shell of the organ or the tumor and fill it with tissue equivalent agarose mixtures (Niebuhr et al. 2019). This method allows for achieving a realistic, human-like anatomical shape while simultaneously adjusting the imaging contrast individually. This technique was used for the pancreas and the two kidneys, which were filled with a nickel-diethylenetriaminepentaacetic acid (NiDTPA)-doped agarose gel, closely matching human tissue imaging properties (Elter et al. 2021, Weidner et al. 2021) (**Paper I**). This approach was not feasible for the spine, as each vertebra was too small to be printed hollow, filled with a NiDTPA-agarose mixture and fit a dosimeter insert. Another method to achieve different HU values is the use of material from the FDM printer. Therefore, the spine of PPIeT was printed with Diran 410MF07 (Stratasys, Israel, 3D printer Stratasys F370) to achieve higher HU values comparable to the spine of a human (**Paper I**). The duodenum was 3D-printed with the polyjet technique again, however, using a flexible 3D printing material, allowing for organ deformation based on gas-filling or liquid-filling conditions. This flexibility facilitated changes in the duodenum's shape and simultaneously its positioning relative to the pancreas. Consequently, 3D printing proved to be a versatile tool in the development of PPIeT.

Medical imaging with 3D printing

Already in previous studies on phantom development, 3D printing has been extensively used to create various in-house developed phantoms allowing for the customization of parts through rapid prototyping at low cost (Filippou et al. 2018, Cloonan et al. 2014, Okkalidis 2022). Exploring materials from different printing technologies allows for the assessment of HU values, as well as other relevant parameters for ultrasound or MR imaging such as T1 and T2 times. Gear et al. (2016) developed a 3D-printed liver phantom using VeroClear, VeroWhite and TangoBlack Plus (Stratasys, Israel). This approach enabled the adaptation of

the liver geometry to match that of a selected patient, allowing for customized imaging contrasts using CT and SPECT modalities (Gear et al. 2016). With the same 3D printing technique Leng et al. (2016) 3D-printed a realistic liver phantom that incorporated anatomical structures such as lesions and vessels (Leng et al. 2016) and Woliner van der Weg et al. (2016) designed a pancreas and kidney phantom for single photon emission computed tomography (SPECT)/CT reconstruction optimization (Woliner-van der Weg et al. 2016). Bücking et al. (2017) employed the FDM printing technique, using polylactic acid (PLA) with different infill densities to create realistic ultrasound images of the ribcage, liver, and lung (Bücking et al. 2017). The use of PLA resulted in realistic shadowing similar to real ultrasound imaging. Also, Robinson et al. (2016) made use of the FDM printing technique and printed kidneys and livers of varying sizes with acrylonitrile butadiene styrene (ABS) to investigate size effects on SPECT imaging (Robinson et al. 2019).

3D printing for radiotherapy

It is important to highlight that 3D printing has not only been described for generating phantoms for medical imaging but also for radiotherapy applications. For instance, a patient-specific 3D chest phantom was developed using PLA and was equipped with radiochromic EBT3 films to measure dose during intraoperative radiation therapy (Choi et al. 2021). In this study, gypsum was employed for bone representation for the 3D-printed pelvis to enhance imaging contrast. Unfortunately, gypsum could not be used for the bone representation in PPIeT as it reacted with the superabsorber-water mixture, which was used as the matrix in the phantom and the chemical reaction led to an altered matrix consistency (**Paper I**). Additionally, encasing the 3D-printed spine in gypsum would hinder the insertion of holes required for the radiochromic film inserts in each vertebra.

In future, the 3D printing approach holds the potential to achieve an optimal scenario in which each organ is replicated using a material that accurately mimics human tissue properties across various imaging modalities and for different radiation therapy regimes. Ultimately, this could enable the 3D printing of whole-body phantoms based on the CT or MRI of a patient in a single print, achieving human-like imaging contrast and stopping power ratios for ion therapy.

3D printing for collimator development

In addition to the use of 3D printing for phantom construction, 3D printing is also highly valuable in various prototyping applications. In this thesis, 3D printing was used to develop a versatile mini-beam collimator, as outlined in **Paper II**, and to adapt it for carbon ion irradiation, as described in **Paper III**. In **Paper II**, 3D printing enabled the production of 40 mm x 10 mm plastic plates with different thicknesses and angles to achieve various ctc's and to compensate for the X-ray

beam divergence at different source-to-collimator distances (SCDs). In between the plastic plates, metal plates of either tungsten or brass were positioned, by using a 3D-printed scaffold. For **Paper III**, the scaffold design was adapted to eliminate the need for plastic plates as a parallel beam was assumed. Without the plastic plates, the primary carbon ions were not attenuated in the peak regions leading to a sharper mini-beam pattern. Therefore, 1 mm cavities were designed to position the metal plates spaced by 1 mm air gaps. While a similar scaffold design was initially tested for photon irradiation, it encountered two main challenges. First, during the testing of smaller SCDs, which required greater adaptation for X-ray beam divergence, the precise angular positioning of the metal plates became crucial to achieve a sharp peak. However, employing an undercut design for the 3D-printed scaffold required additional supporting material from the 3D printer. Unfortunately, this support material couldn't be fully removed without leaving residues, resulting in openings too small to fit the metal plates. Conversely, setting tolerances too high in the 3D-printed scaffold to accommodate the metal plates led to difficulties in achieving reproducible positioning.

In general, 3D printing is increasingly acknowledged as a rapidly advancing technology and its ability to manufacture customized objects tailored to diverse requirements in radiotherapy. Patient-specific and individualized solutions are particularly notable, reflecting the potential for enhanced precision and efficacy in cancer treatment. In the studies described in **Paper I**, **Paper II** and **Paper III**, advanced 3D printing techniques were employed to create an anthropomorphic phantom, using a variety of materials and a versatile mini-beam collimator for both, X-ray and CIRT.

3.2 Anthropomorphic phantoms

The ultimate objective of radiotherapy is to achieve more effective treatment outcomes by ensuring precise radiation dosage to target the tumor while safeguarding the functionality of healthy tissues. Phantoms, whether produced through 3D printing or other manufacturing techniques, play a key role in achieving this goal. They are employed for quality assurance purposes of the treatment plans, encompassing both quantitative and qualitative measurements, as well as for investigating new research inquiries without posing risks to patients (Tajik et al. 2022, Wegner et al. 2023). Given the high complexity of anthropomorphic phantoms and the growing demand for phantoms tailored to specific research inquiries, there is an increased need for in-house developed anthropomorphic phantoms that are specifically designed to address these requirements.

Development of PPIeT

Within this thesis, the anthropomorphic phantom PPIeT was specifically developed to address the research question regarding the treatment of pancreatic tumors with carbon ion beams (**Paper I, Paper III**). For this, it was necessary to assess the radiation dose during breathing-induced motion within the target and the OARs. A simple geometric phantom, however, could not simulate the complexity of the organ shape and positioning representing a realistic model of the human body, and simultaneously allowing the study of the interplay during motion. Thus, PPIeT encompasses the anthropomorphic shape and position of the organs in the abdominal region as well as imaging tissue equivalent materials for each of the considered organs. Moreover, the size of each organ matches real human proportions and their shape mimics those found in humans.

End-to-end test with PPIeT

This facilitates the examination of the multi-step process of radiotherapy, also known as end-to-end test, where each step of the radiotherapy chain is evaluated. Shortly, an end-to-end test would start with imaging using either CT or MRI, followed by the treatment planning, and lastly the verification of the delivered dose. For PPIeT, an end-to-end test is feasible. First of all, the phantom includes human equivalent CT and MRI contrast, which was achieved by dedicated mixtures of NiDTPA-doped agarose gel for each organ (Elter et al. 2021). The 3D-printed shells surrounding the mixture for organs like the pancreas and the kidneys ensure long-term stability by preventing material exchange with the environment (Weidner et al. 2022). The next step of the end-to-end test is the contouring of the organs and structures to be considered in the treatment planning, where the target and the OARs are delineated. However, contouring introduces potential errors, not only within the phantom but especially within the patients due to subjective physician interpretation. For example, Lappas et al. (2022) reported a displacement of the center of mass from (0.08 ± 0.04) mm for the lungs to (0.5 ± 0.3) mm for the spinal cord for two different examiners (Lappas et al. 2022). The enhanced visibility of contours in PPIeT compared to patients suggests that uncertainties are likely smaller. Next, the treatment plan for PPIeT was computed following the procedure used for patients. Raystation (Version 11B (12.0.0.932), RaySearch Laboratories, USA) was used for this, which allows for quasi-automatic treatment plan calculation. The phantom was then positioned in the HIT experimental room mimicking patient positioning, and dose delivery was evaluated using various detectors such as IC and radiochromic films. Custom-made inserts in each organ allowed for the interchange of dosimeters to measure doses with different detectors, similar to other phantoms like the ARDOS phantom, for which an IC, radiochromic films or TLDs can be inserted (Kostiukhina et al. 2017). In comparison, PPIeT distinguishes itself by enabling dose measurements within OARs and the target simultaneously during CIRT, a capability not present in previous phantoms. With this feature, it is possible

to understand the dose distribution in both, target and OARs for the same motion pattern.

Advances and challenges in phantom development

The dose measurement simultaneously at the target and OARs during motion within a realistic human geometry is primarily feasible because PPIeT exhibits a high degree of anthropomorphism, with organs closely mimicking their real-life counterparts in shape and image contrast. While further refining anthropomorphism by incorporating additional organs, such as the stomach, intestine and spleen, and structural tissues like muscle and fat was considered, it complicates the swift exchange of dosimetric inserts needed for dose measurements under varying conditions while ensuring reproducibility. To mitigate these limitations, the superabsorber-water mixture, denser than water yet flexible, was chosen as the internal matrix of the phantom housing the organs over introducing additional structural tissue. This viscose matrix allows organs to be positioned without hindering the process of motion or insert exchange. The chosen superabsorber-water mixture remains stable throughout the irradiation process during the motion application as well as the detector exchange. Compared to other phantoms this is a main advantage as e.g. agarose matrices can rupture during motion application, compromising reproducibility and image quality due to water infiltration in the cracks of the agarose matrix, leading to imaging contrast differences (Weidner et al. 2022).

Moreover, a potential improvement could involve the integration of living materials such as cell lines or organoids into the phantom. This might include introducing cell lines that correspond to the organ or tumor type, facilitating the simultaneous irradiation of various cell types. With this, it would be possible to understand not only the exact physical effect of the absorbed dose but also the biological effect of CIRT within the different organs. This could provide a deeper understanding of the RBE models, which can not be determined with physical dose measurements alone, thus being an important factor since one of the main advantages of CIRT is the increased biological effect compared to photon radiotherapy (Clausen et al. 2019). Although studies have already reported irradiation of cells within a phantom, these mostly comprise a geometrical phantom environment (Altman et al. 2009, Clausen et al. 2019). For example, Clausen et al. (2019) developed a block-shaped PMMA phantom capable of hosting 16 cell culture flasks, each containing a mono-layer of cells (Clausen et al. 2019). This setup enabled the irradiation of cells at different depths of the beam, facilitating the investigation of depth dose effects in proton irradiation. However, including cells in a more anthropomorphic environment would enable the examination of parameters beyond RBE, such as the exact influence of radiation scattering and breathing-induced motion. In **Paper II**, initial *in vitro* studies for spatially fractionated doses are detailed, focusing on exploring the DNA damage effects at the valley and peak regions. As this was a feasibility test, these

studies were conducted in 12-well plates rather than using an anthropomorphic phantom. Future experiments could involve integrating cells into PPIeT using biocompatible 3D printing materials (MED610, MED625FLX, Stratasys, Israel) that support cell growth. Given the convenient design of inserts for each organ within PPIeT, positioning cells within specific organs would be straightforward to implement.

Another aspect that could be explored in phantom development is the investigation of variations according to age, gender and body mass index (BMI) as the tumor might respond differently to irradiation (Medeiros Oliveira Ramos 2017). While the anatomy in the abdomen tends to remain relatively consistent across genders, an increasing BMI can influence the amount of fat tissue around the organs and thus impact the treatment planning and scattering within the body, impacting the dose deposition in the body. Similarly, ageing brings about changes in pancreas anatomy, including volume, dimensions, contour, and increased intra-pancreatic fat deposition (Sato et al. 2012, Möller et al. 2023). Since PPIeT represents a woman with an average BMI, radiotherapy treatment planning and dose application changes due to the mentioned factors are not considered in PPIeT. One potential approach to personalize this process could involve replacing the pancreas and other organs of PPIeT with those reproducing the size and shape of each patient, eventually also adjusting the size of the whole container. Nonetheless, it's important to recognize that these suggestions may result in the development of more complex and challenging phantoms, that could pose difficulties in clinical environments (Medeiros Oliveira Ramos 2017).

3.3 Carbon ion therapy

As highlighted, radiotherapy is one of the primary applications of phantoms and phantom design becomes especially interesting in a field where the expertise is limited or controversial, like pancreatic cancer treatment with carbon ions. Recent studies showed improved oncological outcomes for CIRT compared to photon irradiation (Kawashiro et al. 2018, Baltazar et al. 2023). However, drawing definitive conclusions is challenging due to the use of a variety of energy spectra, beam depths and RBE models across different facilities and countries. Also, the applied concomitant chemotherapy of the different studies leads to challenges in comparison, necessitating further studies to confirm both efficacy and safety (Liermann et al. 2020a).

CIRT for pancreatic cancer at HIT

At HIT pancreatic cancer treatment is currently offered to a rather small group of patients, resulting in a limited dataset. Therefore, PPIeT was specifically designed

to enable measurements with CIRT for pancreatic cancer patients. Typically, pancreas patients at HIT receive treatment with two beams from the back at angles of 250° and 290° (Liermann et al. 2020a). This setup is designed to allow the beams to traverse between the kidneys and the spine to reach the pancreas. Interestingly, within other centers, different beam configurations are employed ranging from one to four angles in a star configuration (Mori et al. 2014, Batista et al. 2017). The choice of two beams from the back is possible because at HIT a gantry is available, enabling rotational movement of the beam around the patient. Since the gantry is not available for experimental settings, irradiations were performed in the experimental room with a horizontal beam line. To allow the same beam geometry for PPIeT as for pancreas patients at HIT, a rotation table was designed to enable the reproducible positioning of PPIeT at both angles (**Paper I**).

A comparable challenge arises for facilities without access to a gantry, which is frequently the case. One alternative that is currently being explored at HIT is the use of a capsule that facilitates patient rotation instead of beam rotation (Dietrich et al. 2024). Furthermore, upright positioning is under assessment, as it may facilitate the convenient and cost-effective irradiation of specific body parts with beam configurations that might be impractical with a horizontal beam line if the patient was in a supine position (Volz et al. 2022, Boisbouvier et al. 2022, Hegarty et al. 2022).

CIRT comparability across facilities

Additionally to the beam configuration, each irradiation facility uses its specific treatment planning system, leading to variations in dose calculation models that affect the accurate calculation of dose considering the RBE. Currently, three models for calculating RBE are used, with the local effect model (LEM) employed in Europe, and the Microdosimetric Kinetic Model and Mixed-Beam Model used in Japan (Malouff et al. 2020). At HIT, RayStation (RaySearch Laboratories, USA) and the “Syngo RT Planning” (Siemens, Erlangen, Germany) are applied, which employ the LEM I (Kramer et al. 2000, Dreher et al. 2017). In this model, the RBE of carbon ions relies on factors such as the α/β ratio, serving as input for the LEM and subsequent dose calculations. Conversely, at Chiba (Heavy Ion Medical Accelerator, HIMAC), the RBE is assumed to have an average value of 3.0 in the SOBP region (Mori et al. 2014, Dreher et al. 2017). As a result, there are no established standard protocols for CIRT and comparing studies from different centers becomes challenging. PPIeT could potentially aid in refining RBE models through *in vitro* studies in future research by measuring cell response at different facilities. Nevertheless, it is important to note that the versatility of PPIeT extends beyond CIRT, as the materials used have also been validated for use with photons or positron emission tomography (PET) in other phantom studies (Mayer et al. 2015, Kim et al. 2017, Gillmann et al. 2021). For photon irradiation, also radiochromic films and ICs could be used to measure the dose during motion in the different

organs and for PET, specific inserts could be 3D-printed to insert the radioactive isotopes in the organs.

Addressing LET challenges in CIRT

Another challenge that needs to be addressed is the variation of LET within the tissues of the pancreas and the OARs (Baltazar et al. 2023). Therefore, the dosimeters used to measure the physical dose corresponding to the RBE-optimized plan can lead to misinterpretation. It is well known that the dose-response of radiochromic films is LET-dependent as a quenching effect for high LET carbon ions can lead to dose underestimations of up to 30 % to 40 % in the Bragg peak, depending on the initial energy of the carbon ions (Martisikova et al. 2010, Castriconi et al. 2017, Yonai et al. 2018). For this reason, **Paper I** only reports optical density (OD) differences instead of dose values. Nevertheless, the dose in the pancreas was verified with a pinpoint IC, showing variation in the static setup from the planned dose of less than 1 %. Due to the constraint space lateral to the kidneys and the spine, it was not feasible to insert an IC within the OARs. Therefore, only passive detectors were used, such as radiochromic films, but also LET independent detectors such as optically stimulated luminescence detectors (OSLDs) (**Paper III**). In summary, PPIeT successfully allowed for carbon ion dose measurements using various detectors in different organs simultaneously. This capability also allows testing other irradiation schemes such as SFRT and thereby provides valuable insights into the dosimetric behavior within specific anatomical structures.

3.4 Spatial fractionation in radiotherapy

While CIRT has become established in clinical practice, SFRT, particularly mini-beam irradiation, remains in the preclinical stage. There is no reported reason for this, especially considering that newer modalities like FLASH have swiftly advanced into clinical application (Daugherty et al. 2023, Kinj et al. 2024). According to the International Commission on Radiation Units and Measurements (ICRU) reports, prescribed doses are typically constrained within a narrow range, typically from 95 % and 107 % (ICRU report, 2010). Therefore, physicians continue to follow the predominant paradigm of delivering a homogeneous dose to the entire tumor, while the preclinical evidence concerning mini-beam irradiation remains inconclusive.

Dosimetry of SFRT

One potential reason for the relative delay in the implementation of mini-beams for therapy might be that, in contrast to conventional radiotherapy, the dosimetry for SFRT is more complex. Determining the appropriate dose and comparing between studies poses significant challenges, resulting in a range of incomparable data. This is not only true for photons, where the mini-beam pattern dominates throughout the

depth but also for protons and carbon ions. While the mini-beam pattern diminishes over depth for protons and to a lesser extent for carbon ions, the dosimetric challenge is even more pronounced in these cases and yet there are no guidelines. In **Paper II**, dosimetry for X-ray mini-beam irradiation was performed with radiochromic films, measuring the dose at the x-y plane of the cell layer. To convert the OD values of the radiochromic film into dose values, a calibration curve was implemented and doses were correlated using an IC. For the obtained mini-beam pattern several parameters were calculated such as peak dose, valley dose, FWHM, etc and PVDR.

The impact of key parameters in SFRT

Unfortunately, the relevance of each parameter in SFRT for clinical outcome remains uncertain, requiring further investigations to achieve optimal tumor control and minimize toxicity (Fernandez Palomo et al. 2022). It was observed that the valley dose demonstrates a strong association with tumor treatment response. Conversely, the peak dose exhibits the weakest correlation with the tumor treatment response (Rivera et al. 2020a, Rivera et al. 2020b, Fernandez Palomo et al. 2020). However, this leads to another problem, as most publications do not provide a clear definition of peak and valley doses, nor are there established guidelines. In **Paper II**, for instance, the highest and lowest dose values respectively for the peak and valley doses were considered and the mean of each peak and valley in a mini-beam pattern was calculated. A more robust definition could be the calculation of a certain region around the peaks and valleys, for example considering the 5 % to 10 % of the highest and lowest dose values to define the peak and valley doses. With this approach, outliers could have a less pronounced impact. Another approach to reduce outliers would be the smoothing of the mini-beam pattern. However, the criteria for smoothing must be carefully considered, as it would impact the resulting peak and valley values. These considerations highlight the need to address these questions before SFRT can advance further.

Another parameter in close correlation to the peak and valley doses is the PVDR, which is widely used in the mini-beam and micro-beam community within simulations and experiments (Dilmanian et al. 2002). However, as the valley dose approaches zero, the PVDR tends to infinity, making it difficult to interpret the PVDR value alone (Reaz et al. 2023). Tsubouchi et al. (2018) introduced a new parameter, known as the valley-to-peak dose ratio (VPDR), which avoids the issue of division by a number approaching zero (Tsubouchi et al. 2018). Given that the valley dose is an important parameter, this new concept could be considered in future. Yet, the widespread adoption of this parameter across the research community presents its challenges, which is why **Paper II** and **Paper III** report the PVDR value instead of the VPDR.

Additionally to the dose-related parameter, the geometrical setup of the collimator, which determines the FWHM and the etc, must be considered. For **Paper II**,

the FWHM was tested from 0.5 mm to 2.0 mm and the ctc from 1.0 mm to 2.0 mm, allowing for doubling or quadrupling of the spacing between two peaks. This geometry aligns with previous research indicating improved outcomes when the ctc was increased to double or four times the FWHM (Prezado et al. 2017b). In **Paper III**, however, the FWHM and the ctc were both set at 1.0 mm to simplify the collimator design and conduct a proof-of-concept irradiation of the pancreas virtual target of PPIeT with iMBRT.

Mini-beam collimator design

In general, the mini-beam collimator presented was developed to facilitate testing of each of these parameters for MBRT. This device can simplify the establishment of standardized parameters such as FWHM, ctc and PVDR to achieve the desired mini-beam effect and clinical outcome. The mini-beam collimator offers the flexibility to easily adapt to various experimental setups, enabling *in vitro* testing and potentially facilitating future *in vivo* studies. Other available mini-beam collimators are mostly rigid and lack flexibility in parameter adjustment. These mini-beam collimators are typically manufactured through wire-eroding, an expensive process that consumes a lot of material (Prezado et al. 2017a, Kim et al. 2022). For the mini-beam collimator developed in this study, the same tungsten plates were used in both **Paper II** and **Paper III**, with only adjustments made to the 3D-printed scaffold. This approach saves time, materials and costs since the same mini-beam collimator components can be reconfigured.

3.5 Phantom irradiation with iMBRT

The adaption of the mini-beam collimator for carbon ions made it possible to irradiate PPIeT with iMBRT (**Paper III**) by using the very same treatment plan geometry previously used (**Paper I**). The mini-beam pattern was successfully quantified in the OARs and a rather homogeneous pattern was observed at the pancreas (**Paper III**).

Treatment planning for iMBRT

As a general point when considering the translation of iMBRT to patients, it is worth considering that there is currently no commercial treatment planning system available for this. The only mini-beam treatment plans available are in-house programmed treatment plans with Monte Carlo (MC) for proton beams, where the RBE is considered constant, simplifying the calculations (Lansonneur et al. 2020, Ortiz et al. 2023). These MC codes optimize both PVDR and dose objectives concurrently, aiming to achieve a maximal PVDR (Lin et al. 2023).

As presented in **Paper III**, the treatment plan was applied in one fraction with

a peak dose of 4 Gy (RBE) as a proof-of-concept study. For *in vivo* studies, the dose is usually also applied in one fraction but escalated to peak doses of several 100 Gy and valley doses of around 10 Gy (Fernandez-Palomo et al. 2022). This would result in an increased irradiation time compared to the 4 minutes used in **Paper III**, potentially leading to more pronounced motion-induced mini-beam pattern blurring. To address this issue, MBRT could be implemented using ultra-high dose rates. However, this capability is not commonly accessible in all radiation facilities, and if available, it typically involves proton beams rather than carbon ions (Reindl et al. 2019, Schneider et al. 2022). Therefore, another option would be to apply mini-beams via multiple fractions as done in conventional radiotherapy. However, with several fractions, sub-millimeter precision in positioning the mini-beams across multiple irradiation sessions would be necessary to always irradiate the same tissue point with either peak or valley. This requires technical resources and is mainly challenged by organ motion, potentially reducing the mini-beam effect (Sammer et al. 2021a). A study on fractionation with SFRT observed increased toxicity in the ears of mice when different positions for the peak and valley regions were chosen for each fraction (Sammer et al. 2021b). Hence, in the abdominal region where precise positioning of internal organs on a sub-millimeter level is not feasible, the implementation of SFRT within a single fraction should be considered.

Dosimetry for iMBRT

Although single-fractionated MBRT would simplify dosimetry, dosimetry for iMBRT remains challenging. For **Paper III** the dose could not be verified with a pinpoint IC due to the inhomogeneous dose distribution of the mini-beam pattern. Instead, a calibration curve for each depth of the different organs including 0 mm for the skin, 40 mm for the spine, 45 mm for the right kidney and 120 mm for the pancreas was established with radiochromic films to quantify the dose distribution in each organ. As radiochromic films are LET dependent iMBRT poses an additional challenge due to the high and low doses subsequently to each other theoretically also the LET changes within the pattern. However, it was shown that these LET changes are neglectable (Gonzalez et al. 2017). To gain a deeper understanding of the irradiation in various depths during iMBRT, the beamline at HIT and the mini-beam collimator were modeled, and the mini-beam pattern was simulated in depth using MC simulations. This analysis revealed a similar broadening of the beam at the target compared to experimental results observed in PPIeT, as well as a distinct mini-beam pattern within other organs. However, the PVDR obtained from the MC simulation was higher compared to the experimental data. This observed difference can primarily be attributed to the radiochromic film not being perfectly positioned perpendicular to the beam direction within PPIeT. In contrast, for MC simulations, a simplified geometry was implemented, with the beam always perpendicular to the radiochromic film. In the future, a CT of PPIeT can be imported into the MC code and simulations with the anthropomorphic geometry could be implemented to

allow for exact scattering, beam direction contribution and organ densities when calculating the mini-beam pattern.

Comparing peak doses of the mini-beam pattern with doses measured with OSLDs showed good agreement, except in the pancreas. Here, the radiochromic film dose was significantly lower compared to the OSLD-measured dose and the planned dose. This can be explained by MC simulation, which revealed a 61.3 % reduction in the target region if the collimator was present compared to homogeneous irradiation without a collimator. Applying this correction factor to the radiochromic film dose in the target region aligned it with both the OSLD-measured and planned doses.

3.6 Organ motion during radiotherapy

The concern about organ motion during radiotherapy is about balancing the delivery of a high dose to the target while minimizing exposure to surrounding tissues to optimize the therapeutic outcomes (Korreman et al. 2012). To quantify the impact of organ motion effect during pancreatic cancer CIRT, **Paper I** reports the construction of a pancreas phantom for CIRT with breathing-induced organ motion and GI motion. Pancreas motion of about 20 mm led to a significant reduction in the target dose within the virtual pancreas tumor and also increased the variability of dose for each treatment plan application. A similar result was reported by Lebbink et al. (2022), where a motion of 20 mm reduced the dose significantly and deviations of up to 14 % were found in the ARDOS phantom measured with an IC (Lebbink et al. 2022). Taking into account that pancreas patient motion was found to be 1.0 mm up to 27.3 mm, there will likely be a subset of patients with even greater motion, necessitating appropriate consideration of motion management (Bhasin et al. 2006, Knybel et al. 2014, Dolde et al. 2019, Jing et al. 2021).

Motion challenges in radiotherapy

Especially the Bragg peak and sharp lateral penumbra characteristic of CIRT render it more sensitive to intrafractional motion compared to photon irradiation (Malouff et al. 2020). However, this problem is multifaceted, as other parameters like the scanning mode of the beam delivery might also play a crucial role when considering organ motion. Due to the scan direction of the beam, interplay effects can appear, and this is highly dependent on the characteristics of the beamline, spot sizes, the direction of the scanning and the time needed to switch the energy layer, in an active beam delivery system (Lambert et al. 2005).

When combining MBRT and CIRT, the motion of the organs becomes an even more critical problem, as the mini-beam dose pattern can be blurred, potentially leading to worsened patient treatment outcomes. One first step to reduce undesired effects caused by organ motion is to position the mini-beam collimator with the slits parallel to the main direction of the organ motion, the cranial-caudal (CC)

direction, as done in **Paper III**. Theoretically, the motion effect in this direction could be omitted. Nevertheless, the human breathing-induced organ motion does not only extend in one direction but in all three dimensions, presenting also minor components in the right-left (RL) and anterior-posterior (AP) directions (Fukada et al. 2015, Fontana et al. 2016). For PPIeT, mainly the CC direction of the organs' motion was simulated, but there is slight motion in the other directions similar to humans. Therefore, the mini-beam pattern within the kidney was significantly reduced by motion, while the non-moving organs were not affected.

Patient-specific motion simulation with PPIeT

Another aspect that needs to be accounted for is the unexpected motions of the patient, such as coughing, sneezing or yawning (Brandner et al. 2017). This can not be predicted and poses a potential risk which is hard to account for. PPIeT's breathing motion was simulated with an amplitude from 5 mm to 20 mm with a squared cosine function, thus resulting in a regular breathing pattern and consequently in an induced organ motion following the same temporal pattern (**Paper I**). Nevertheless, the versatility of PPIeT and its motion system allows the use of any arbitrary patient-specific breathing motion pattern, including irregularities like coughing or breath hold. In the future, this feature could be used to evaluate novel techniques aimed at predicting or adapting irradiation to motion in real time.

Gastrointestinal motion simulation with PPIeT

Beyond respiratory motion, PPIeT can also account for GI motion. This is particularly significant due to the proximity of the duodenum to the pancreas, where GI motion can dynamically change the distance between the pancreas and the duodenum. This variability in the distance upon the filling state of the duodenum was shown by Mostafaei et al. (2018), where changes in distance between the duodenum and the pancreas from 13.0 mm up to 18.5 mm were found. With distance changes of 14 mm, PPIeT could mimic the duodenal motion as reported in **Paper I**, underscoring the complex interplay between organs during radiotherapy treatment delivery. Although the feasibility of GI motion was tested without CIRT, future studies could explore this aspect further by coupling breathing-induced organ motion with GI motion during CIRT. Another aspect of GI motion is not only the motion of the organ itself but also the gas motion within the bowel. If gases are present in the charged particle beam path but are not accounted for in the treatment plan, it can significantly affect the range of the particles, potentially failing to accurately target the intended area (Kumagai et al. 2009).

Motion mitigation strategies

To mitigate motion, various strategies have been implemented in radiotherapy to address breathing-induced tumor and organ motions, such as rescanning, abdominal compression, deep inspiration breath hold (DIBH), or respiratory gating (RG). Each technique offers distinct trade-offs among ease of implementation, patient comfort, and effectiveness in motion reduction (Zeng et al. 2020). Rescanning reduces the interplay effect of carbon ions with motion as investigated by Lebbink et al. (2022), observing a reduced dose distortion if layer-rescanning was applied with the ARDOS phantom (Lebbink et al. 2022). However, improvements for motion mitigation were predominantly found in plans with a limited number of fields and when field directions were nearly orthogonal to the direction of motion (Knopf et al. 2011). Abdominal compression showed effective motion mitigation of CC motion. However, AP and RL motions were increased slightly (Daly et al. 2022). DIBH is a motion mitigation technique that implies the irradiation only if the patients hold their breath, reducing the dose to the heart and lungs. However, it necessitates patient cooperation and requires additional time and effort from the staff (Zeng et al. 2020). Additionally, even with DIBH, significant motion of the pancreas was observed (Lens et al. 2016). The most effective motion mitigation strategy was RG for motion in all directions (Campbell et al. 2017). While the effectiveness of RG for pancreatic cancer treatment has been demonstrated for protons, leading to a noticeable improvement in dose homogeneity within the target, the evaluation of RG for carbon ions remains largely unexplored (Dolde et al. 2019).

In summary, the major novelty of this work is the simultaneous measurement of the dose at the target and the OARs during breathing-induced motion. Previous studies have mainly focused on the dose in the target during organ motion, but there is no quantification of the impact of motion on the dose distribution in the OARs. In future studies, PPIeT could be used to test motion mitigation strategies for carbon ions while simultaneously measuring the dose at the target and the OARs. Ultimately, the results obtained from such studies could improve pancreatic cancer treatment outcomes, increasing the survival time of patients.

4. Conclusion

This cumulative thesis presents three original studies evaluating carbon ion radiotherapy combined with mini-beam irradiation to perform dose measurement within an anthropomorphic phantom with motion features.

The developed abdominal phantom PPIeT offers human-like motion features and tissue-equivalent CT and MRI contrast for precise dose assessment during carbon ion radiotherapy. Furthermore, PPIeT proved useful for simultaneous dose measurement at the target and the OARs. During breathing-induced organ motion, a dose decrease of 21 % was found in the virtual pancreas tumor compared to the treatment plan. Significant dose variations were also found in the OARs, particularly in the right kidney. These findings highlight the importance of considering organ motion for carbon ion irradiation.

Additionally, this thesis presents the development of a versatile and low-cost mini-beam collimator that enables the adjustment of various mini-beam parameters. This was achieved by arranging metal and plastic plates of different sizes within a 3D-printed plastic scaffold. Experimental validations and *in vitro* studies confirmed the collimator's efficacy in achieving the desired mini-beam patterns. For the mini-beam collimator configuration with 1 mm metal and 1 mm plastic plates, a maximum deviation of 2 % was found for the FWHM compared to the expected value according to the mini-beam collimator design.

Combining these two studies, the mini-beam collimator was adapted for carbon ion radiotherapy and used for irradiating PPIeT. This was the first analysis of the impact of breathing-induced organ motion during carbon ion mini-beam therapy for pancreatic cancer. The breathing-induced motion led to a 61 % decrease in PVDR of the mini-beam pattern within the kidney, potentially leading to increased OAR damage during treatment. This provides pioneering insights into how the mini-beam pattern changes under different motion conditions.

The scientific outcomes of this thesis provide three original advancements to the field: the anthropomorphic abdominal phantom with breathing motion feature, the versatile mini-beam collimator and the findings on the organ motion impact on tumor and OARs during carbon ion mini-beam radiotherapy. These developments and findings offer opportunities for dose measurements across different radiation therapy methods, ultimately contributing to advancing patient treatment outcomes.

5. Summary

Pancreatic cancer is an aggressive tumor, with approximately 50 % of cases diagnosed at an advanced and metastasized stage and a five-year survival rate ranging only from 5 % to 10 %. Conventional therapies for this type of cancer encounter significant challenges due to pancreatic tumor resistance to radiation and complications arising from organ motion. To overcome these obstacles, this thesis proposes the combination of carbon ion radiotherapy (CIRT) and mini-beam radiotherapy (MBRT). However, both methods are susceptible to organ motion, therefore it is essential to investigate its impact on dose distribution, simultaneously considering the target and the organs at risk (OARs).

An anthropomorphic abdominal Pancreas Phantom for Ion beam Therapy (PPIeT) was developed aiming at investigating the organ motion impact. Constructed from 3D-printed anatomical structures with realistic imaging contrasts for CT and MRI, PPIeT can simulate breathing-induced organ motion and gastrointestinal movement. Different dosimeters, including ionization chambers and radiochromic films, were employed to measure doses within the pancreatic tumor and OARs, including the duodenum, kidneys, spine, and spinal cord. In parallel, an affordable and versatile mini-beam collimator was constructed using a 3D-printed scaffold to position metal plates for various configurations. The performance of the mini-beam collimator was validated during *in vitro* studies with x-ray irradiations. Subsequent irradiations of PPIeT involved conventional and spatially fractionated CIRT during different breathing-induced organ motion conditions.

For conventional irradiation of PPIeT with CIRT a significant under-dosage of the tumor was observed when breathing was applied, while dose fluctuations in the OARs varied. When using the mini-beam collimator, precise mini-beam pattern generation was achieved, with an accuracy higher than 98 % for the 1 mm peak and 1 mm valley configuration. This configuration was selected for irradiating PPIeT with carbon ions, leading to uniform irradiation of the tumor even during organ motion. However, organ motion blurred mini-beam patterns within the kidneys, potentially compromising the tissue-sparing mini-beam effect. This research contributes to advance carbon ion-based cancer treatments, highlighting the need for tailored strategies considering motion-induced risks in pancreatic cancer radiotherapy.

6. Zusammenfassung

Bauchspeicheldrüsenkrebs wird in etwa 50 % der Fälle in einem fortgeschrittenen und metastasierten Stadium diagnostiziert und die Fünfjahresüberlebensrate beträgt nur 5 bis 10 %. Konventionelle Bestrahlung stößt auf erhebliche Probleme aufgrund von Strahlenresistenz und Komplikationen durch die atembedingte Organbewegung. Aus diesem Grund wird in dieser Arbeit eine Kombination aus Kohlenstoff-Ionen-Therapie (CIRT) und Minibeam-Bestrahlung (MBRT) vorgeschlagen, um die Wirksamkeit der Behandlung zu erhöhen und gleichzeitig die Schädigung kritischer Risikoorgane zu minimieren. Beide Methoden sind jedoch anfällig für Organbewegungen.

Um diesen Effekt zu untersuchen, wurde ein anthropomorphes abdominales Pankreas-Phantom für die Ionenstrahltherapie (PPIeT) entwickelt. PPIeT wurde aus 3D-gedruckten anatomischen Strukturen mit realistischen CT- und MRT-Kontrasten konstruiert und simuliert atembedingte Organbewegungen und gastrointestinale Bewegungen. Die Dosis wurde mit einer Ionisationskammer und radiochromen Filmen innerhalb des Pankreastumors und der Risikoorgane, wie dem Zwölffingerdarm, der Nieren, der Wirbelsäule und dem Rückenmark, gemessen. Zudem wurde ein kostengünstiger und adaptierbarer Minibeam Kollimator entwickelt, um verschiedene Minibeam Kollimator Konfigurationen zu erzeugen. Primäre Tests mit Röntgenstrahlung wurden durchgeführt, um die Leistung des Kollimators zu validieren. Nachfolgende Bestrahlungen von PPIeT umfassten homogene und räumlich fraktionierte CIRT unter Verwendung verschiedener atmungsinduzierter Bewegungsamplituden.

Bei der homogenen Bestrahlung von PPIeT mit CIRT wurde eine signifikante Unterdosierung des Tumors beobachtet, während die Dosisschwankungen in den Risikoorganen je nach Organ variierten. Mit der Minibeam Kollimator Konfiguration von 1 mm Peak- und 1 mm Valley-Breite konnte eine Genauigkeit von über 98 % erreicht werden. Diese Konfiguration wurde für die Bestrahlung von PPIeT ausgewählt, was unter statischen Bedingungen zu der Erzeugung eines präzisen Minibeammusters führte. Durch atembedingte Organbewegung kam es jedoch zu unscharfen Minibeammustern in der Niere was den gewebeschonenden Minibeam-Effekt beeinträchtigen könnte. Somit unterstreicht diese Forschung die Notwendigkeit maßgeschneiderter Strategien, die die durch Bewegung induzierten Risiken in der Strahlentherapie bei Bauchspeicheldrüsenkrebs berücksichtigen.

7. References

- Abou Khouzam, R., Lehn, J.M., Mayr, H., Clavien, P.A., Wallace, M.B., Ducreux, M., Limani, P., Chouaib, S., 2023. Hypoxia, a Targetable Culprit to Counter Pancreatic Cancer Resistance to Therapy. *Cancers* **15**, 1235. doi:10.3390/cancers15041235.
- Altman, M.B., Vesper, B.J., Smith, B.D., Stinauer, M.A., Pelizzari, C.A., Aydogan, B., Reft, C.S., Radosevich, J.A., Chmura, S.J., Roeske, J.C., 2009. Characterization of a novel phantom for three-dimensional in vitro cell experiments. *Physics in Medicine & Biology* **54**, N75. doi:10.1088/0031-9155/54/5/N02.
- Anderson, E.M., Thomassian, S., Gong, J., Hendifar, A., Osipov, A., 2021. Advances in Pancreatic Ductal Adenocarcinoma Treatment. *Cancers* **13**, 5510. doi:10.3390/cancers13215510.
- Asur, R.S., Sharma, S., Chang, C.W., Penagaricano, J., Kommuru, I.M., Moros, E.G., Corry, P.M., Griffin, R.J., 2012. Spatially Fractionated Radiation Induces Cytotoxicity and Changes in Gene Expression in Bystander and Radiation Adjacent Murine Carcinoma Cells. *Radiation Research* **177**, 751–765. doi:10.1667/rr2780.1.
- Baltazar, F., Tessonier, T., Haberer, T., Debus, J., Herfarth, K., Tawk, B., Knoll, M., Abdollahi, A., Liermann, J., Mairani, A., 2023. Carbon-ion radiotherapy (CIRT) as treatment of pancreatic cancer at HIT: initial radiation plan analysis of the prospective phase II PACK-study. *Radiotherapy and Oncology* **188**, 109872. doi:10.1016/j.radonc.2023.109872.
- Batista, V., Richter, D., Combs, S.E., Jäkel, O., 2017. Planning strategies for inter-fractional robustness in pancreatic patients treated with scanned carbon therapy. *Radiation Oncology (London, England)* **12**, 94. doi:10.1186/s13014-017-0832-x.
- Bazyar, S., Inscoc, C.R., O'Brian, E.T., Zhou, O., Lee, Y.Z., 2017. Minibeam radiotherapy with small animal irradiators; in vitro and in vivo feasibility studies. *Physics in Medicine and Biology* **62**, 8924–8942. doi:10.1088/1361-6560/aa926b.
- Bert, C., Durante, M., 2011. Motion in radiotherapy: particle therapy. *Physics in Medicine & Biology* **56**, R113. doi:10.1088/0031-9155/56/16/R01.
- Bertho, A., Iturri, L., Brisebard, E., Juchaux, M., Gilbert, C., Ortiz, R., Sebrie, C., Jourdain, L., Lamirault, C., Ramasamy, G., Pouzoulet, F., Prezado, Y., 2023. Evaluation of the Role of the Immune System Response After Minibeam Radiation Therapy. *International Journal of Radiation Oncology, Biology, Physics* **115**, 426–439. doi:10.1016/j.ijrobp.2022.08.011.
- Bhasin, D.K., Rana, S.S., Jahagirdar, S., Nagi, B., 2006. Does the pancreas move with respiration? *Journal of Gastroenterology and Hepatology* **21**, 1424–1427. doi:10.1111/j.1440-1746.2006.04324.x.
- Billena, C., Khan, A.J., 2019. A Current Review of Spatial Fractionation: Back to the Future? *International journal of radiation oncology, biology, physics* **104**, 177–187. doi:10.1016/j.ijrobp.2019.01.073.

- Bittner, M.I., Grosu, A.L., Brunner, T.B., 2015. Comparison of toxicity after IMRT and 3D-conformal radiotherapy for patients with pancreatic cancer – A systematic review. *Radiotherapy and Oncology* **114**, 117–121. doi:10.1016/j.radonc.2014.11.043.
- Boisbouvier, S., Boucaud, A., Tanguy, R., Grégoire, V., 2022. Upright patient positioning for pelvic radiotherapy treatments. *Technical Innovations & Patient Support in Radiation Oncology* **24**, 124–130. doi:10.1016/j.tipsro.2022.11.003.
- Bouchart, C., Navez, J., Closset, J., Hendlisz, A., Van Gestel, D., Moretti, L., Van Laethem, J.L., 2020. Novel strategies using modern radiotherapy to improve pancreatic cancer outcomes: toward a new standard? *Therapeutic Advances in Medical Oncology* **12**, 1–26. doi:10.1177/1758835920936093.
- Brandner, E.D., Chetty, I.J., Giaddui, T.G., Xiao, Y., Huq, M.S., 2017. Motion management strategies and technical issues associated with stereotactic body radiotherapy of thoracic and upper abdominal tumors: A review from NRG oncology. *Medical Physics* **44**, 2595–2612. doi:10.1002/mp.12227.
- Brönnimann, D., Bouchet, A., Schneider, C., Potez, M., Serduc, R., Bräuer-Krisch, E., Graber, W., von Gunten, S., Laissue, J.A., Djonov, V., 2016. Synchrotron microbeam irradiation induces neutrophil infiltration, thrombocyte attachment and selective vascular damage in vivo. *Scientific Reports* **6**, 33601. doi:10.1038/srep33601.
- Busato, F., Khouzai, B.E., Mognato, M., 2022. Biological Mechanisms to Reduce Radioresistance and Increase the Efficacy of Radiotherapy: State of the Art. *International Journal of Molecular Sciences* **23**, 10211. doi:10.3390/ijms231810211.
- Bussels, B., Goethals, L., Feron, M., Bielen, D., Dymarkowski, S., Suetens, P., Haustermans, K., 2003. Respiration-induced movement of the upper abdominal organs: a pitfall for the three-dimensional conformal radiation treatment of pancreatic cancer. *Radiotherapy and Oncology: Journal of the European Society for Therapeutic Radiology and Oncology* **68**, 69–74. doi:10.1016/s0167-8140(03)00133-6.
- Bücking, T.M., Hill, E.R., Robertson, J.L., Maneas, E., Plumb, A.A., Nikitichev, D.I., 2017. From medical imaging data to 3D printed anatomical models. *PLoS ONE* **12**, e0178540. doi:10.1371/journal.pone.0178540.
- Campbell, W.G., Jones, B.L., Schefter, T., Goodman, K.A., Miften, M., 2017. An evaluation of motion mitigation techniques for pancreatic SBRT. *Radiotherapy and oncology : journal of the European Society for Therapeutic Radiology and Oncology* **124**, 168–173. doi:10.1016/j.radonc.2017.05.013.
- Castriconi, R., Ciocca, M., Mirandola, A., Sini, C., Broggi, S., Schwarz, M., Fracchiolla, F., Martišíková, M., Aricò, G., Mettivier, G., Russo, P., 2017. Dose–response of EBT3 radiochromic films to proton and carbon ion clinical beams. *Physics in Medicine and Biology* **62**, 377–393. doi:10.1088/1361-6560/aa5078.
- Chauffert, B., Mornex, F., Bonnetain, F., Rougier, P., Mariette, C., Bouché, O., Bosset, J.F., Aparicio, T., Mineur, L., Azzedine, A., Hammel, P., Butel, J., Stremsdoerfer, N., Maingon, P., Bedenne, L., 2008. Phase III trial comparing intensive induction chemoradiotherapy (60 Gy, infusional 5-FU and intermittent cisplatin) followed by maintenance gemcitabine with gemcitabine alone for locally advanced unresectable pancreatic cancer. Definitive results of the 2000-01 FFCD/SFRO study. *Annals of Oncology: Official Journal of the European Society for Medical Oncology* **19**, 1592–1599. doi:10.1093/annonc/mdn281.
- Cheung, Y., Sawant, A., 2015. An externally and internally deformable, programmable lung motion phantom. *Medical Physics* **42**, 2585–2593. doi:10.1118/1.4918581.

- Choi, Y., Lee, I.J., Park, K., Park, K.R., Cho, Y., Kim, J.W., Lee, H., 2021. Patient-Specific Quality Assurance Using a 3D-Printed Chest Phantom for Intraoperative Radiotherapy in Breast Cancer. *Frontiers in Oncology* **11**. doi:10.3389/fonc.2021.629927.
- Chtcheprov, P., Hadsell, M., Burk, L., Ger, R., Zhang, L., Yuan, H., Lee, Y.Z., Chang, S., Lu, J., Zhou, O., 2013. Physiologically gated micro-beam radiation therapy using electronically controlled field emission x-ray source array. *Proceedings of SPIE—the International Society for Optical Engineering* **8671**, 86711Z. doi:10.1117/12.2007998.
- Clausen, M., Khachonkham, S., Gruber, S., Kuess, P., Seemann, R., Knäusl, B., Mara, E., Palmans, H., Dörr, W., Georg, D., 2019. Phantom design and dosimetric characterization for multiple simultaneous cell irradiations with active pencil beam scanning. *Radiation and Environmental Biophysics* **58**, 563–573. doi:10.1007/s00411-019-00813-1.
- Cloonan, A.J., Shahmirzadi, D., Li, R.X., Doyle, B.J., Konofagou, E.E., McGloughlin, T.M., 2014. 3D-Printed Tissue-Mimicking Phantoms for Medical Imaging and Computational Validation Applications. *3D Printing and Additive Manufacturing* **1**, 14–23. doi:10.1089/3dp.2013.0010.
- Colvill, E., Krieger, M., Bosshard, P., Steinacher, P., Schmidrig, B.A.R., Parkel, T., Stergiou, I., Zhang, Y., Peroni, M., Safai, S., Weber, D.C., Lomax, A., Fattori, G., 2020. Anthropomorphic phantom for deformable lung and liver CT and MR imaging for radiotherapy. *Physics in Medicine & Biology* **65**, 07NT02. doi:10.1088/1361-6560/ab7508.
- Daly, M., McWilliam, A., Radhakrishna, G., Choudhury, A., Eccles, C.L., 2022. Radiotherapy respiratory motion management in hepatobiliary and pancreatic malignancies: a systematic review of patient factors influencing effectiveness of motion reduction with abdominal compression. *Acta Oncologica* **61**, 833–841. doi:10.1080/0284186X.2022.2073186.
- Datzmann, G., Sammer, M., Girst, S., Mayerhofer, M., Dollinger, G., Reindl, J., 2020. Preclinical Challenges in Proton Minibeam Radiotherapy: Physics and Biomedical Aspects. *Frontiers in Physics* **8**. doi:10.3389/fphy.2020.568206.
- Daugherty, E.C., Mascia, A., Zhang, Y., Lee, E., Xiao, Z., Sertorio, M., Woo, J., McCann, C., Russell, K., Levine, L., Sharma, R., Khuntia, D., Bradley, J., Simone, C.B., Perentesis, J., Breneman, J., 2023. FLASH Radiotherapy for the Treatment of Symptomatic Bone Metastases (FAST-01): Protocol for the First Prospective Feasibility Study. *JMIR research protocols* **12**, e41812. doi:10.2196/41812.
- Dertinger, H., Jung, H., (Eds.), 1970. Direct and Indirect Action of Radiation, in: *Molecular Radiation Biology: The Action of Ionizing Radiation on Elementary Biological Objects*. Springer US, New York, NY, pp. 70–90. doi:10.1007/978-1-4684-6247-0_6.
- Dewhirst, M.W., Cao, Y., Moeller, B., 2008. Cycling hypoxia and free radicals regulate angiogenesis and radiotherapy response. *Nature Reviews. Cancer* **8**, 425–437. doi:10.1038/nrc2397.
- Dietrich, K.A., Klüter, S., Dinkel, F., Echner, G., Brons, S., Orzada, S., Debus, J., Ladd, M.E., Platt, T., 2024. An essentially radiation-transparent body coil integrated with a patient rotation system for MR-guided particle therapy. *Medical Physics* **51**, 4028–4043. doi:10.1002/mp.17065.
- Dilmanian, F.A., Button, T.M., Le Duc, G., Zhong, N., Peña, L.A., Smith, J.A.L., Martinez, S.R., Bacarian, T., Tammam, J., Ren, B., Farmer, P.M., Kalef-Ezra, J., Micca, P.L., Nawrocky, M.M., Niederer, J.A., Recksiek, F.P., Fuchs, A., Rosen, E.M., 2002. Response

- of rat intracranial 9L gliosarcoma to microbeam radiation therapy. *Neuro-Oncology* **4**, 26–38. doi:10.1093/neuonc/4.1.26.
- Dilmanian, F.A., Eley, J.G., Krishnan, S., 2015. Minibeam therapy with protons and light ions: Physical feasibility and the potential to reduce radiation side effects and to facilitate hypofractionation. *International journal of radiation oncology, biology, physics* **92**, 469–474. doi:10.1016/j.ijrobp.2015.01.018.
- Dilmanian, F.A., Zhong, Z., Bacarian, T., Benveniste, H., Romanelli, P., Wang, R., Welwart, J., Yuasa, T., Rosen, E.M., Ansel, D.J., 2006. Interlaced x-ray microplanar beams: a radiosurgery approach with clinical potential. *Proceedings of the National Academy of Sciences of the United States of America* **103**, 9709–9714. doi:10.1073/pnas.0603567103.
- Dolde, K., Naumann, P., Dávid, C., Kachelriess, M., Lomax, A.J., Weber, D.C., Saito, N., Burigo, L.N., Pfaffenberger, A., Zhang, Y., 2019. Comparing the effectiveness and efficiency of various gating approaches for PBS proton therapy of pancreatic cancer using 4D-MRI datasets. *Physics in Medicine and Biology* **64**, 085011. doi:10.1088/1361-6560/ab1175.
- Dreher, C., Habermehl, D., Jäkel, O., Combs, S.E., 2017. Effective radiotherapeutic treatment intensification in patients with pancreatic cancer: higher doses alone, higher RBE or both? *Radiation Oncology (London, England)* **12**, 203. doi:10.1186/s13014-017-0945-2.
- Durante, M., Debus, J., Loeffler, J.S., 2021. Physics and biomedical challenges of cancer therapy with accelerated heavy ions. *Nature Reviews Physics* **3**, 777–790. doi:10.1038/s42254-021-00368-5.
- Ehrbar, S., Jöhl, A., Kühni, M., Meboldt, M., Ozkan Elsen, E., Tanner, C., Goksel, O., Klöck, S., Unkelbach, J., Guckenberger, M., Tanadini-Lang, S., 2019. ELPHA: Dynamically deformable liver phantom for real-time motion-adaptive radiotherapy treatments. *Medical Physics* **46**, 839–850. doi:10.1002/mp.13359.
- Elter, A., Hellwich, E., Dorsch, S., Schäfer, M., Runz, A., Klüter, S., Ackermann, B., Brons, S., Karger, C.P., Mann, P., 2021. Development of phantom materials with independently adjustable CT- and MR-contrast at 0.35, 1.5 and 3 T. *Physics in Medicine and Biology* **66**, 045013. doi:10.1088/1361-6560/abd4b9.
- Falco, M., Masojć, B., Sulikowski, T., 2023. Radiotherapy in Pancreatic Cancer: To Whom, When, and How? *Cancers* **15**, 3382. doi:10.3390/cancers15133382.
- Fernandez-Palomo, C., Chang, S., Prezado, Y., 2022. Should Peak Dose Be Used to Prescribe Spatially Fractionated Radiation Therapy?—A Review of Preclinical Studies. *Cancers* **14**, 3625. doi:10.3390/cancers14153625.
- Filippou, V., Tsoumpas, C., 2018. Recent advances on the development of phantoms using 3D printing for imaging with CT, MRI, PET, SPECT, and ultrasound. *Medical Physics* **45**, e740–e760. doi:10.1002/mp.13058.
- Fontana, G., Riboldi, M., Gianoli, C., Chirvase, C.I., Villa, G., Paganelli, C., Summers, P.E., Tagaste, B., Pella, A., Fossati, P., Ciocca, M., Baroni, G., Valvo, F., Orecchia, R., 2016. MRI quantification of pancreas motion as a function of patient setup for particle therapy —a preliminary study. *Journal of Applied Clinical Medical Physics* **17**, 60–75. doi:10.1120/jacmp.v17i5.6236.
- Fukada, J., Kitago, M., Sutani, S., Itano, O., Hanada, T., Kitagawa, Y., Shigematsu, N., 2015. Quantification of Interfraction and Intrafraction Pancreas Motion Using Pancreatic Stent. *International Journal of Radiation Oncology, Biology, Physics* **93**, E178–E179. doi:10.1016/j.ijrobp.2015.07.1005.

- Garajová, I., Peroni, M., Gelsomino, F., Leonardi, F., 2023. A Simple Overview of Pancreatic Cancer Treatment for Clinical Oncologists. *Current Oncology* **30**, 9587–9601. doi:10.3390/curroncol30110694.
- Gear, J.I., Cummings, C., Craig, A.J., Divoli, A., Long, C.D.C., Tapner, M., Flux, G.D., 2016. Abdo-Man: a 3D-printed anthropomorphic phantom for validating quantitative SIRT. *EJNMMI Physics* **3**, 17. doi:10.1186/s40658-016-0151-6.
- Gillmann, C., Homolka, N., Johnen, W., Runz, A., Echner, G., Pfaffenberger, A., Mann, P., Schneider, V., Hoffmann, A.L., Troost, E.G.C., Koerber, S.A., Kotzerke, J., Beuthien-Baumann, B., 2021. Technical Note: ADAM PETer - An anthropomorphic, deformable and multimodality pelvis phantom with positron emission tomography extension for radiotherapy. *Medical Physics* **48**, 1624–1632. doi:10.1002/mp.14597.
- Girst, S., Greubel, C., Reindl, J., Siebenwirth, C., Zlobinskaya, O., Walsh, D.W.M., Ilicic, K., Aichler, M., Walch, A., Wilkens, J.J., Multhoff, G., Dollinger, G., Schmid, T.E., 2016. Proton Minibeam Radiation Therapy Reduces Side Effects in an In Vivo Mouse Ear Model. *International Journal of Radiation Oncology, Biology, Physics* **95**, 234–241. doi:10.1016/j.ijrobp.2015.10.020.
- Glowa, C., Peschke, P., Brons, S., Neels, O.C., Kopka, K., Debus, J., Karger, C.P., 2017. Carbon ion radiotherapy: impact of tumor differentiation on local control in experimental prostate carcinomas. *Radiation Oncology* **12**, 174. doi:10.1186/s13014-017-0914-9.
- González, W., Peucelle, C., Prezado, Y., 2017. Theoretical dosimetric evaluation of carbon and oxygen minibeam radiation therapy. *Medical Physics* **44**, 1921–1929. doi:10.1002/mp.12175.
- Graham, K., Unger, E., 2018. Overcoming tumor hypoxia as a barrier to radiotherapy, chemotherapy and immunotherapy in cancer treatment. *International Journal of Nanomedicine* **13**, 6049–6058. doi:10.2147/IJN.S140462.
- Grimbergen, G., Eijkelenkamp, H., Heerkens, H.D., Raaymakers, B.W., Intven, M.P., Meijer, G.J., 2021. Intrafraction pancreatic tumor motion patterns during ungated magnetic resonance guided radiotherapy with an abdominal corset. *Physics and Imaging in Radiation Oncology* **21**, 1–5. doi:10.1016/j.phro.2021.12.001.
- Hegarty, S., Hardcastle, N., Korte, J., Kron, T., Everitt, S., Rahim, S., Hegi-Johnson, F., Franich, R., 2022. Please Place Your Seat in the Full Upright Position: A Technical Framework for Landing Upright Radiation Therapy in the 21st Century. *Frontiers in Oncology* **12**. doi:10.3389/fonc.2022.821887.
- Hirayama, R., Ito, A., Tomita, M., Tsukada, T., Yatagai, F., Noguchi, M., Matsumoto, Y., Kase, Y., Ando, K., Okayasu, R., Furusawa, Y., 2009. Contributions of direct and indirect actions in cell killing by high-LET radiations. *Radiation Research* **171**, 212–218. doi:10.1667/RR1490.1.
- Huang, Y., Huang, Q., Zhao, J., Dong, Y., Zhang, L., Fang, X., Sun, P., Kong, L., Lu, J.J., 2020. The Impacts of Different Types of Radiation on the CRT and PDL1 Expression in Tumor Cells Under Normoxia and Hypoxia. *Frontiers in Oncology* **10**, 1610. doi:10.3389/fonc.2020.01610.
- ICRU Report 83: Prescribing, Recording, and Reporting Photon-Beam Intensity-Modulated Radiation Therapy (IMRT). 2010. *Journal of the ICRU* **10**, pp. 1-106. doi:10.1093/jicru_ndq008.
- Jan, I.S., Ch'ang, H.J., 2023. Selection of patients with pancreatic adenocarcinoma who may benefit from radiotherapy. *Radiation Oncology* **18**, 137. doi:10.1186/s13014-023-02328-y.

- Jing, S., Jiang, C., Ji, X., Qiu, X., Li, J., Sun, X., Zhu, X., 2021. Study on Motion Management of Pancreatic Cancer Treated by CyberKnife. *Frontiers in Oncology* **11**, 767832. doi:10.3389/fonc.2021.767832.
- Jäkel, O., 2020. Physical advantages of particles: protons and light ions. *The British Journal of Radiology* **93**, 20190428. doi:10.1259/bjr.20190428.
- Kadoya, N., Sakulsingharoj, S., Kron, T., Yao, A., Hardcastle, N., Bergman, A., Okamoto, H., Mukumoto, N., Nakajima, Y., Jingu, K., Nakamura, M., 2021. Development of a physical geometric phantom for deformable image registration credentialing of radiotherapy centers for a clinical trial. *Journal of Applied Clinical Medical Physics* **22**, 255–265. doi:10.1002/acm2.13319.
- Kalantzopoulos, C., Meschini, G., Paganelli, C., Fontana, G., Vai, A., Preda, L., Vitolo, V., Valvo, F., Baroni, G., 2020. Organ motion quantification and margins evaluation in carbon ion therapy of abdominal lesions. *Physica Medica* **75**, 33–39. doi:10.1016/j.ejmp.2020.05.014.
- van de Kamp, G., Heemskerk, T., Kanaar, R., Essers, J., 2021. DNA Double Strand Break Repair Pathways in Response to Different Types of Ionizing Radiation. *Frontiers in Genetics* **12**. doi:10.3389/fgene.2021.738230.
- Kawashiro, S., Yamada, S., Okamoto, M., Ohno, T., Nakano, T., Shinoto, M., Shioyama, Y., Nemoto, K., Isozaki, Y., Tsuji, H., Kamada, T., 2018. Multi-institutional Study of Carbon-ion Radiotherapy for Locally Advanced Pancreatic Cancer: Japan Carbon-ion Radiation Oncology Study Group (J-CROS) Study 1403 Pancreas. *International Journal of Radiation Oncology, Biology, Physics* **101**, 1212–1221. doi:10.1016/j.ijrobp.2018.04.057.
- Kim, J.i., Park, J.M., Wu, H.G., 2020. Carbon Ion Therapy: A Review of an Advanced Technology. *Progress in Medical Physics* **31**, 71–80. doi:10.14316/pmp.2020.31.3.71.
- Kim, M., Hwang, U.J., Park, K., Kim, D., Kim, H.S., Choi, S.H., Jeong, J.H., Shin, D., Lee, S.B., Kim, J.Y., Kim, T.H., Baek, H.J., Kim, H., Kim, K., Kim, S.S., Lim, Y.K., 2022. Dose Profile Modulation of Proton Minibeam for Clinical Application. *Cancers* **14**, 2888. doi:10.3390/cancers14122888.
- Kim, M.J., Lee, S.R., Lee, M.Y., Sohn, J.W., Yun, H.G., Choi, J.Y., Jeon, S.W., Suh, T.S., 2017. Characterization of 3D printing techniques: Toward patient specific quality assurance spine-shaped phantom for stereotactic body radiation therapy. *PLoS ONE* **12**, e0176227. doi:10.1371/journal.pone.0176227.
- Kinj, R., Gaide, O., Jeanneret-Sozzi, W., Dafni, U., Vignat-Carrin, S., Sagittario, E., Kyriotou, M., Chenal, J., Duclos, F., Hebeisen, M., Falco, T., Geyer, R., Gonçalves Jorge, P., Moeckli, R., Bourhis, J., 2024. Randomized phase II selection trial of FLASH and conventional radiotherapy for patients with localized cutaneous squamous cell carcinoma or basal cell carcinoma: A study protocol. *Clinical and Translational Radiation Oncology* **45**, 100743. doi:10.1016/j.ctro.2024.100743.
- Kiseleva, V., Gordon, K., Vishnyakova, P., Gantsova, E., Elchaninov, A., Fatkhudinov, T., 2022. Particle Therapy: Clinical Applications and Biological Effects. *Life* **12**, 2071. doi:10.3390/life12122071.
- Knopf, A.C., Hong, T.S., Lomax, A., 2011. Scanned proton radiotherapy for mobile targets—the effectiveness of re-scanning in the context of different treatment planning approaches and for different motion characteristics. *Physics in Medicine and Biology* **56**, 7257–7271. doi:10.1088/0031-9155/56/22/016.

- Knybel, L., Cvek, J., Otahal, B., Jonszta, T., Molenda, L., Czerny, D., Skacelikova, E., Rybar, M., Dvorak, P., Felzl, D., 2014. The analysis of respiration-induced pancreatic tumor motion based on reference measurement. *Radiation Oncology* **9**, 192. doi:10.1186/1748-717X-9-192.
- Kohler, A., 1909. Zur röntgentiefentherapie mit massendosen. *MMW* , 2314–2316.
- Korreman, S.S., 2012. Motion in radiotherapy: photon therapy. *Physics in Medicine & Biology* **57**, R161. doi:10.1088/0031-9155/57/23/R161.
- Kostiukhina, N., Georg, D., Rollet, S., Kuess, P., Sipaj, A., Andrzejewski, P., Furtado, H., Rausch, I., Lechner, W., Steiner, E., Kertész, H., Knäusl, B., 2017. Advanced Radiation DOSimetry phantom (ARDOS): a versatile breathing phantom for 4D radiation therapy and medical imaging. *Physics in Medicine & Biology* **62**, 8136. doi:10.1088/1361-6560/aa86ea.
- Kostiukhina, N., Palmans, H., Stock, M., Knopf, A., Georg, D., Knäusl, B., 2020. Time-resolved dosimetry for validation of 4D dose calculation in PBS proton therapy. *Physics in Medicine & Biology* **65**, 125015. doi:10.1088/1361-6560/ab8d79.
- Krämer, M., Scholz, M., 2000. Treatment planning for heavy-ion radiotherapy: calculation and optimization of biologically effective dose. *Physics in Medicine and Biology* **45**, 3319–3330. doi:10.1088/0031-9155/45/11/314.
- Kumagai, M., Hara, R., Mori, S., Yanagi, T., Asakura, H., Kishimoto, R., Kato, H., Yamada, S., Kandatsu, S., Kamada, T., 2009. Impact of Intrafractional Bowel Gas Movement on Carbon Ion Beam Dose Distribution in Pancreatic Radiotherapy. *International Journal of Radiation Oncology, Biology, Physics* **73**, 1276–1281. doi:10.1016/j.ijrobp.2008.10.055.
- Kundapur, V., Mayer, M., Auer, R.N., Alexander, A., Weibe, S., Pushie, M.J., Cranmer-Sargison, G., 2022. Is Mini Beam Ready for Human Trials? Results of Randomized Study of Treating De-Novo Brain Tumors in Canines Using Linear Accelerator Generated Mini Beams. *Radiation Research* **198**, 162–171. doi:10.1667/RADE-21-00093.1.
- Laissue, J., Blattmann, H., Slatkin, D., 2012. Alban Köhler (1874-1947): Inventor of grid therapy. *Zeitschrift für Medizinische Physik* **22**, 90–99. doi:10.1016/j.zemedi.2011.07.002.
- Lambert, J., Suchowerska, N., McKenzie, D.R., Jackson, M., 2005. Intrafractional motion during proton beam scanning. *Physics in Medicine and Biology* **50**, 4853–4862. doi:10.1088/0031-9155/50/20/008.
- Lansonneur, P., Mammar, H., Nauraye, C., Patriarca, A., Hierso, E., Dendale, R., Prezado, Y., De Marzi, L., 2020. First proton minibeam radiation therapy treatment plan evaluation. *Scientific Reports* **10**, 7025. doi:10.1038/s41598-020-63975-9.
- Lappas, G., Staut, N., Lieuwes, N.G., Biemans, R., Wolfs, C.J., van Hoof, S.J., Dubois, L.J., Verhaegen, F., 2022. Inter-observer variability of organ contouring for preclinical studies with cone beam Computed Tomography imaging. *Physics and Imaging in Radiation Oncology* **21**, 11–17. doi:10.1016/j.phro.2022.01.002.
- Lebbink, F., Stock, M., Georg, D., Knäusl, B., 2022. The Influence of Motion on the Delivery Accuracy When Comparing Actively Scanned Carbon Ions versus Protons at a Synchrotron-Based Radiotherapy Facility. *Cancers* **14**, 1788. doi:10.3390/cancers14071788.
- Leng, S., Chen, B., Vrieze, T., Kuhlmann, J., Yu, L., Alexander, A., Matsumoto, J., Morris, J., McCollough, C.H., 2016. Construction of realistic phantoms from patient images and a commercial three-dimensional printer. *Journal of Medical Imaging* **3**, 033501. doi:10.1117/1.JMI.3.3.033501.

- Lennie, E., Tsoumpas, C., Sourbron, S., 2021. Multimodal phantoms for clinical PET/MRI. *EJNMMI Physics* **8**, 62. doi:10.1186/s40658-021-00408-0.
- Lens, E., van der Horst, A., Versteijne, E., Bel, A., van Tienhoven, G., 2016. Considerable pancreatic tumor motion during breath-holding. *Acta Oncologica* **55**, 1360–1368. doi:10.1080/0284186X.2016.1221532.
- Li, S., Gong, Y., Yang, Y., Guo, Q., Qian, J., Tian, Y., 2020. Evaluation of small bowel motion and feasibility of using the peritoneal space to replace bowel loops for dose constraints during intensity-modulated radiotherapy for rectal cancer. *Radiation Oncology (London, England)* **15**, 211. doi:10.1186/s13014-020-01650-z.
- Liermann, J., Naumann, P., Hommertgen, A., Pohl, M., Kieser, M., Debus, J., Herfarth, K., 2020a. Carbon ion radiotherapy as definitive treatment in non-metastasized pancreatic cancer: study protocol of the prospective phase II PACK-study. *BMC Cancer* **20**, 947. doi:10.1186/s12885-020-07434-8.
- Liermann, J., Shinoto, M., Syed, M., Debus, J., Herfarth, K., Naumann, P., 2020b. Carbon ion radiotherapy in pancreatic cancer: A review of clinical data. *Radiotherapy and Oncology* **147**, 145–150. doi:10.1016/j.radonc.2020.05.012.
- Lin, Y., Zhang, W., Prezado, Y., Traneus, E., Johnson, D., Li, W., Gan, G.N., Chen, R.C., Gao, H., 2023. Towards Clinical Proton Minibeam Radiation Therapy (pMBRT): Development of Clinical pMBRT System Prototype and pMBRT-Specific Treatment Planning Method. *International Journal of Radiation Oncology*Biography*Physics* **117**, S38. doi:10.1016/j.ijrobp.2023.06.307.
- Liu, J., Lee, P., McGee, H.M., Chung, V., Melstrom, L., Singh, G., Raof, M., Amini, A., Chen, Y.J., Williams, T.M., 2022. Advances in Radiation Oncology for Pancreatic Cancer: An Updated Review. *Cancers* **14**, 5725. doi:10.3390/cancers14235725.
- Liu, Z., Parveen, N., Rehman, U., Aziz, A., Sheikh, A., Abourehab, M.A.S., Guo, W., Huang, J., Wang, Z., Kesharwani, P., 2023. Unravelling the enigma of siRNA and aptamer mediated therapies against pancreatic cancer. *Molecular Cancer* **22**, 8. doi:10.1186/s12943-022-01696-5.
- Loehrer, P.J., Feng, Y., Cardenas, H., Wagner, L., Brell, J.M., Cella, D., Flynn, P., Ramanathan, R.K., Crane, C.H., Alberts, S.R., Benson, A.B., 2011. Gemcitabine alone versus gemcitabine plus radiotherapy in patients with locally advanced pancreatic cancer: an Eastern Cooperative Oncology Group trial. *Journal of Clinical Oncology: Official Journal of the American Society of Clinical Oncology* **29**, 4105–4112. doi:10.1200/JCO.2011.34.8904.
- Lopez Perez, R., Nicolay, N.H., Wolf, J.C., Frister, M., Schmezer, P., Weber, K.J., Huber, P.E., 2019. DNA damage response of clinical carbon ion versus photon radiation in human glioblastoma cells. *Radiotherapy and Oncology: Journal of the European Society for Therapeutic Radiology and Oncology* **133**, 77–86. doi:10.1016/j.radonc.2018.12.028.
- Mahaney, B.L., Meek, K., Lees-Miller, S.P., 2009. Repair of ionizing radiation-induced DNA double strand breaks by non-homologous end-joining. *The Biochemical journal* **417**, 639–650. doi:10.1042/BJ20080413.
- Mali, S.B., 2024. Mini review of spatially fractionated radiation therapy for cancer management. *Oral Oncology Reports* **9**, 100175. doi:10.1016/j.oor.2024.100175.
- Malouff, T.D., Mahajan, A., Krishnan, S., Beltran, C., Seneviratne, D.S., Trifiletti, D.M., 2020. Carbon Ion Therapy: A Modern Review of an Emerging Technology. *Frontiers in Oncology* **10**. doi:10.3389/fonc.2020.00082.

- Martíšíková, M., Jäkel, O., 2010. Dosimetric properties of Gafchromic® EBT films in monoenergetic medical ion beams. *Physics in Medicine & Biology* **55**, 3741. doi:10.1088/0031-9155/55/13/011.
- Martínez-Rovira, I., González, W., Brons, S., Prezado, Y., 2017. Carbon and oxygen minibeam radiation therapy: An experimental dosimetric evaluation. *Medical Physics* **44**, 4223–4229. doi:10.1002/mp.12383.
- Mayer, R., Liacouras, P., Thomas, A., Kang, M., Lin, L., Simone, II, C.B., 2015. 3D printer generated thorax phantom with mobile tumor for radiation dosimetry. *Review of Scientific Instruments* **86**, 074301. doi:10.1063/1.4923294.
- Mazal, A., Prezado, Y., Ares, C., de Marzi, L., Patriarca, A., Miralbell, R., Favaudon, V., 2020. FLASH and minibeam radiation therapy: the effect of microstructures on time and space and their potential application to protontherapy. *The British Journal of Radiology* **93**, 20190807. doi:10.1259/bjr.20190807.
- Medeiros Oliveira Ramos, S., 2017. Anthropomorphic phantoms-potential for more studies and training in radiology. *International Journal of Radiology & Radiation Therapy* **2**(4), 101–104. doi:10.15406/ijrrt.2017.02.00033.
- Meyer, J., Eley, J., Schmid, T.E., Combs, S.E., Dendale, R., Prezado, Y., 2019. Spatially fractionated proton minibeam radiation therapy. *The British Journal of Radiology* **92**, 20180466. doi:10.1259/bjr.20180466.
- Meyer, J.E., Kharofa, J., 2023. The Role of Dose Escalation in Pancreatic Cancer: Go Big or Go Home? *International Journal of Radiation Oncology, Biology, Physics* **115**, 395–397. doi:10.1016/j.ijrobp.2022.09.050.
- Mitchel, R.E.J., 2004. The Bystander Effect: Recent Developments and Implications for Understanding the Dose Response. *Nonlinearity in Biology, Toxicology, Medicine* **2**, 173–183. doi:10.1080/15401420490507512.
- Mori, S., Shinoto, M., Yamada, S., 2014. Four-dimensional treatment planning in layer-stacking boost irradiation for carbon-ion pancreatic therapy. *Radiotherapy and Oncology* **111**, 258–263. doi:10.1016/j.radonc.2014.02.014.
- Möller, K., Jenssen, C., Braden, B., Hocke, M., Hollerbach, S., Ignee, A., Faiss, S., Iglesias-Garcia, J., Sun, S., Dong, Y., Carrara, S., Dietrich, C.F., 2023. Pancreatic changes with lifestyle and age: What is normal and what is concerning? *Endoscopic Ultrasound* **12**, 213–227. doi:10.4103/EUS-D-22-00162.
- Naqvi, S.A., Mohiuddin, M.M., Ha, J.K., Regine, W.F., 2008. Effects of tumor motion in GRID therapy. *Medical Physics* **35**, 4435–4442. doi:10.1118/1.2977538.
- Narita, Y., Kato, T., Takemasa, K., Sato, H., Ikeda, T., Harada, T., Oyama, S., Murakami, M., 2021. Dosimetric impact of simulated changes in large bowel content during proton therapy with simultaneous integrated boost for locally advanced pancreatic cancer. *Journal of Applied Clinical Medical Physics* **22**, 90–98. doi:10.1002/acm2.13429.
- Nichols, R.C., 2015. Particle therapy for pancreatic cancer. *Translational Cancer Research* **4**. doi:10.3978/j.issn.2218-676X.2015.11.02.
- Nickoloff, J.A., 2015. Photon, light ion, and heavy ion cancer radiotherapy: paths from physics and biology to clinical practice. *Annals of Translational Medicine* **3**, 336. doi:10.3978/j.issn.2305-5839.2015.12.18.

- Niebuhr, N.I., Johnen, W., Echner, G., Runz, A., Bach, M., Stoll, M., Giske, K., Greilich, S., Pfaffenberger, A., 2019. The ADAM-pelvis phantom-an anthropomorphic, deformable and multimodal phantom for MRgRT. *Physics in Medicine and Biology* **64**, 04NT05. doi:10.1088/1361-6560/aafd5f.
- Okkalidis, N., 2022. 3D printing methods for radiological anthropomorphic phantoms. *Physics in Medicine & Biology* **67**, 15TR04. doi:10.1088/1361-6560/ac80e7.
- Ortiz, R., Belshi, R., De Marzi, L., Prezado, Y., 2023. Proton minibeam radiation therapy for treating metastases: A treatment plan study. *Medical Physics* **50**, 2463–2473. doi:10.1002/mp.16203.
- Ortiz, R., De Marzi, L., Prezado, Y., 2022. Preclinical dosimetry in proton minibeam radiation therapy: Robustness analysis and guidelines. *Medical Physics* **49**, 5551–5561. doi:10.1002/mp.15780.
- Palumbo, E., Piotto, C., Calura, E., Fasanaro, E., Groff, E., Busato, F., El Khouzai, B., Rigo, M., Baggio, L., Romualdi, C., Zafirooulos, D., Russo, A., Mognato, M., Corti, L., 2019. Individual Radiosensitivity in Oncological Patients: Linking Adverse Normal Tissue Reactions and Genetic Features. *Frontiers in Oncology* **9**, 987. doi:10.3389/fonc.2019.00987.
- Park, W., Chawla, A., O'Reilly, E.M., 2021. Pancreatic Cancer: A Review. *JAMA* **326**, 851–862. doi:10.1001/jama.2021.13027.
- Petit, S.F., Wu, B., Kazhdan, M., Dekker, A., Simari, P., Kumar, R., Taylor, R., Herman, J.M., McNutt, T., 2012. Increased organ sparing using shape-based treatment plan optimization for intensity modulated radiation therapy of pancreatic adenocarcinoma. *Radiotherapy and oncology : journal of the European Society for Therapeutic Radiology and Oncology* **102**, 38–44. doi:10.1016/j.radonc.2011.05.025.
- Peucelle, C., Nauraye, C., Patriarca, A., Hierso, E., Fournier-Bidoz, N., Martínez-Rovira, I., Prezado, Y., 2015. Proton minibeam radiation therapy: Experimental dosimetry evaluation. *Medical Physics* **42**, 7108–7113. doi:10.1118/1.4935868.
- Prezado, Y., 2021. Proton minibeam radiation therapy: a promising therapeutic approach for radioresistant tumors. *Comptes Rendus. Biologies* **344**, 409–420. doi:10.5802/crbio1.71.
- Prezado, Y., Dos Santos, M., Gonzalez, W., Jouvion, G., Guardiola, C., Heinrich, S., Labiod, D., Juchaux, M., Jourdain, L., Sebrie, C., Pouzoulet, F., 2017a. Transfer of Minibeam Radiation Therapy into a cost-effective equipment for radiobiological studies: a proof of concept. *Scientific Reports* **7**, 17295. doi:10.1038/s41598-017-17543-3.
- Prezado, Y., Jouvion, G., Hardy, D., Patriarca, A., Nauraye, C., Bergs, J., González, W., Guardiola, C., Juchaux, M., Labiod, D., Dendale, R., Jourdain, L., Sebrie, C., Pouzoulet, F., 2017b. Proton minibeam radiation therapy spares normal rat brain: Long-Term Clinical, Radiological and Histopathological Analysis. *Scientific Reports* **7**, 14403. doi:10.1038/s41598-017-14786-y.
- Principe, D.R., Underwood, P.W., Korc, M., Trevino, J.G., Munshi, H.G., Rana, A., 2021. The Current Treatment Paradigm for Pancreatic Ductal Adenocarcinoma and Barriers to Therapeutic Efficacy. *Frontiers in Oncology* **11**, 688377. doi:10.3389/fonc.2021.688377.
- Rawla, P., Sunkara, T., Gaduputi, V., 2019. Epidemiology of Pancreatic Cancer: Global Trends, Etiology and Risk Factors. *World Journal of Oncology* **10**, 10–27. doi:10.14740/wjon1166.
- Reaz, F., Sitarz, M.K., Traneus, E., Bassler, N., 2023. Parameters for proton minibeam radiotherapy using a clinical scanning beam system. *Acta Oncologica* **62**, 1561–1565.

- doi:10.1080/0284186X.2023.2266125.
- Reindl, J., Girst, S., 2019. pMB FLASH - Status and Perspectives of Combining Proton Minibeam with FLASH Radiotherapy. *Journal of Cancer Immunology* **Volume 1**, 0–0. doi:10.33696/cancerimmunol.1.003.
- Rivera, J.N., Kierski, T.M., Kasoji, S.K., Abrantes, A.S., Dayton, P.A., Chang, S.X., 2020a. Conventional dose rate spatially-fractionated radiation therapy (SFRT) treatment response and its association with dosimetric parameters-A preclinical study in a Fischer 344 rat model. *PloS One* **15**, e0229053. doi:10.1371/journal.pone.0229053.
- Rivera, J.N., Kierski, T.M., Kasoji, S.K., Abrantes, A.S., Dayton, P.A., Chang, S.X., 2020b. Should We Use Peak Dose To Prescribe A Spatially-Fractionated Radiation Therapy (SFRT) Treatment? *International Journal of Radiation Oncology, Biology, Physics* **108**, e571. doi:10.1016/j.ijrobp.2020.07.1760.
- Robinson, A.P., Tipping, J., Cullen, D.M., Hamilton, D., Brown, R., Flynn, A., Oldfield, C., Page, E., Price, E., Smith, A., Snee, R., 2016. Organ-specific SPECT activity calibration using 3D printed phantoms for molecular radiotherapy dosimetry. *EJNMMI Physics* **3**, 12. doi:10.1186/s40658-016-0148-1.
- Sak, A., Stuschke, M., 2010. Use of H2AX and other biomarkers of double-strand breaks during radiotherapy. *Seminars in Radiation Oncology* **20**, 223–231. doi:10.1016/j.semradonc.2010.05.004.
- Sammer, M., Girst, S., Dollinger, G., 2021a. Optimizing proton minibeam radiotherapy by interlacing and heterogeneous tumor dose on the basis of calculated clonogenic cell survival. *Scientific Reports* **11**, 3533. doi:10.1038/s41598-021-81708-4.
- Sammer, M., Dombrowsky, A.C., Schauer, J., Oleksenko, K., Bicher, S., Schwarz, B., Rudigkeit, S., Matejka, N., Reindl, J., Bartzsch, S., Blutke, A., Feuchtinger, A., Combs, S.E., Dollinger, G., Schmid, T.E., 2021b. Normal Tissue Response of Combined Temporal and Spatial Fractionation in Proton Minibeam Radiation Therapy. *International Journal of Radiation Oncology, Biology, Physics* **109**, 76–83. doi:10.1016/j.ijrobp.2020.08.027.
- Sammer, M., Teiluf, K., Girst, S., Greubel, C., Reindl, J., Ilicic, K., Walsh, D.W.M., Aichler, M., Walch, A., Combs, S.E., Wilkens, J.J., Dollinger, G., Schmid, T.E., 2019. Beam size limit for pencil minibeam radiotherapy determined from side effects in an in-vivo mouse ear model. *PloS One* **14**, e0221454. doi:10.1371/journal.pone.0221454.
- Sato, T., Ito, K., Tamada, T., Sone, T., Noda, Y., Higaki, A., Kanki, A., Tanimoto, D., Higashi, H., 2012. Age-related changes in normal adult pancreas: MR imaging evaluation. *European Journal of Radiology* **81**, 2093–2098. doi:10.1016/j.ejrad.2011.07.014.
- Schardt, D., Elsässer, T., Schulz-Ertner, D., 2010. Heavy-ion tumor therapy: Physical and radiobiological benefits. *Reviews of Modern Physics* **82**, 383–425. doi:10.1103/RevModPhys.82.383.
- Schneider, T., 2022. Technical aspects of proton minibeam radiation therapy: Minibeam generation and delivery. *Physica Medica* **100**, 64–71. doi:10.1016/j.ejmp.2022.06.010.
- Schneider, T., De Marzi, L., Patriarca, A., Prezado, Y., 2020. Advancing proton minibeam radiation therapy: magnetically focussed proton minibeam at a clinical centre. *Scientific Reports* **10**, 1384. doi:10.1038/s41598-020-58052-0.
- Schneider, T., Fernandez-Palomo, C., Bertho, A., Fazzari, J., Iturri, L., Martin, O.A., Trappetti, V., Djonov, V., Prezado, Y., 2022. Combining FLASH and spatially fractionated radiation

- therapy: The best of both worlds. *Radiotherapy and Oncology* **175**, 169–177. doi:10.1016/j.radonc.2022.08.004.
- Shinoto, M., Yamada, S., Terashima, K., Yasuda, S., Shioyama, Y., Honda, H., Kamada, T., Tsujii, H., Saisho, H., Working Group for Pancreas Cancer, 2016. Carbon Ion Radiation Therapy With Concurrent Gemcitabine for Patients With Locally Advanced Pancreatic Cancer. *International Journal of Radiation Oncology, Biology, Physics* **95**, 498–504. doi:10.1016/j.ijrobp.2015.12.362.
- Shinoto, M., Yamada, S., Yasuda, S., Imada, H., Shioyama, Y., Honda, H., Kamada, T., Tsujii, H., Saisho, H., Working Group for Pancreas Cancer, 2013. Phase 1 trial of preoperative, short-course carbon-ion radiotherapy for patients with resectable pancreatic cancer. *Cancer* **119**, 45–51. doi:10.1002/cncr.27723.
- Sokol, O., Durante, M., 2023. Carbon Ions for Hypoxic Tumors: Are We Making the Most of Them? *Cancers* **15**, 4494. doi:10.3390/cancers15184494.
- Sotiropoulos, M., Brisebard, E., Le Dudal, M., Jouvion, G., Juchaux, M., Crépin, D., Sebric, C., Jourdain, L., Labiod, D., Lamirault, C., Pouzoulet, F., Prezado, Y., 2021. X-rays minibeam radiation therapy at a conventional irradiator: Pilot evaluation in F98-glioma bearing rats and dose calculations in a human phantom. *Clinical and Translational Radiation Oncology* **27**, 44–49. doi:10.1016/j.ctro.2021.01.001.
- Steinmann, A., Alvarez, P., Lee, H., Court, L., Stafford, R., Sawakuchi, G., Wen, Z., Fuller, C., Followill, D., 2019. MRIgRT dynamic lung motion thorax anthropomorphic QA phantom: Design, development, reproducibility, and feasibility study. *Medical Physics* **46**, 5124–5133. doi:10.1002/mp.13757.
- Sultana, A., Tudur Smith, C., Cunningham, D., Starling, N., Tait, D., Neoptolemos, J.P., Ghaneh, P., 2007. Systematic review, including meta-analyses, on the management of locally advanced pancreatic cancer using radiation/combined modality therapy. *British Journal of Cancer* **96**, 1183–1190. doi:10.1038/sj.bjc.6603719.
- Tajik, M., Akhlaqi, M.M., Gholami, S., 2022. Advances in anthropomorphic thorax phantoms for radiotherapy: a review. *Biomedical Physics & Engineering Express* **8**, 052001. doi:10.1088/2057-1976/ac369c.
- Telarovic, I., Wenger, R.H., Pruschy, M., 2021. Interfering with Tumor Hypoxia for Radiotherapy Optimization. *Journal of Experimental & Clinical Cancer Research* **40**, 197. doi:10.1186/s13046-021-02000-x.
- Tino, R., Yeo, A., Leary, M., Brandt, M., Kron, T., 2019. A Systematic Review on 3D-Printed Imaging and Dosimetry Phantoms in Radiation Therapy. *Technology in Cancer Research & Treatment* **18**, 1533033819870208. doi:10.1177/1533033819870208.
- Treibel, F., Nguyen, M., Ahmed, M., Dombrowsky, A., Wilkens, J.J., Combs, S.E., Schmid, T.E., Bartzsch, S., 2021. Establishment of Microbeam Radiation Therapy at a Small-Animal Irradiator. *International Journal of Radiation Oncology*Biological*Physics* **109**, 626–636. doi:10.1016/j.ijrobp.2020.09.039.
- Tsubouchi, T., Henry, T., Ureba, A., Valdman, A., Bassler, N., Siegbahn, A., 2018. Quantitative evaluation of potential irradiation geometries for carbon-ion beam grid therapy. *Medical Physics* **45**, 1210–1221. doi:10.1002/mp.12749.
- Tubin, S., Vozenin, M., Prezado, Y., Durante, M., Prise, K., Lara, P., Greco, C., Massaccesi, M., Guha, C., Wu, X., Mohiuddin, M., Vestergaard, A., Bassler, N., Gupta, S., Stock, M., Timmerman, R., 2023. Novel unconventional radiotherapy techniques: Current status

- and future perspectives – Report from the 2nd international radiation oncology online seminar. *Clinical and Translational Radiation Oncology* **40**, 100605. doi:10.1016/j.ctro.2023.100605.
- Vedelago, J., Karger, C.P., Jäkel, O., 2022. A review on reference dosimetry in radiation therapy with proton and light ion beams: status and impact of new developments. *Radiation Measurements* **157**, 106844. doi:10.1016/j.radmeas.2022.106844.
- Vevec, M., Moseley, J.L., Eccles, C.L., Craig, T., Sharpe, M.B., Dawson, L.A., Brock, K.K., 2011. Effect of breathing motion on radiotherapy dose accumulation in the abdomen using deformable registration. *International Journal of Radiation Oncology, Biology, Physics* **80**, 265–272. doi:10.1016/j.ijrobp.2010.05.023.
- Vignard, J., Mirey, G., Salles, B., 2013. Ionizing-radiation induced DNA double-strand breaks: A direct and indirect lighting up. *Radiotherapy and Oncology* **108**, 362–369. doi:10.1016/j.radonc.2013.06.013.
- Vitolo, V., Cobianchi, L., Brugnattelli, S., Barcellini, A., Peloso, A., Facchetti, A., Vanoli, A., Delfanti, S., Preda, L., Molinelli, S., Klersy, C., Fossati, P., Orecchia, R., Valvo, F., 2019. Preoperative chemotherapy and carbon ions therapy for treatment of resectable and borderline resectable pancreatic adenocarcinoma: a prospective, phase II, multicentre, single-arm study. *BMC Cancer* **19**, 922. doi:10.1186/s12885-019-6108-0.
- Volz, L., Reidel, C.A., Durante, M., Prezado, Y., Schuy, C., Weber, U., Graeff, C., 2023. Investigating Slit-Collimator-Produced Carbon Ion Minibeams with High-Resolution CMOS Sensors. *Instruments* **7**, 18. doi:10.3390/instruments7020018.
- Volz, L., Sheng, Y., Durante, M., Graeff, C., 2022. Considerations for Upright Particle Therapy Patient Positioning and Associated Image Guidance. *Frontiers in Oncology* **12**. doi:10.3389/fonc.2022.930850.
- Wang, D., Liu, R., Zhang, Q., Luo, H., Chen, J., Dong, M., Wang, Y., Ou, Y., Liu, Z., Sun, S., Yang, K., Tian, J., Li, Z., Wang, X., 2022. Charged Particle Irradiation for Pancreatic Cancer: A Systematic Review of In Vitro Studies. *Frontiers in Oncology* **11**, 775597. doi:10.3389/fonc.2021.775597.
- Wang, J.s., Wang, H.j., Qian, H.l., 2018. Biological effects of radiation on cancer cells. *Military Medical Research* **5**, 20. doi:10.1186/s40779-018-0167-4.
- Woliner-van der Weg, W., Deden, L.N., Meeuwis, A.P.W., Koenrades, M., Peeters, L.H.C., Kuipers, H., Laanstra, G.J., Gotthardt, M., Slump, C.H., Visser, E.P., 2016. A 3D-printed anatomical pancreas and kidney phantom for optimizing SPECT/CT reconstruction settings in beta cell imaging using ¹¹¹In-exendin. *EJNMMI Physics* **3**, 29. doi:10.1186/s40658-016-0165-0.
- Wegner, M., Gargioni, E., Krause, D., 2023. Classification of phantoms for medical imaging. *Procedia CIRP* **119**, 1140–1145. doi:10.1016/j.procir.2023.03.154.
- Weidner, A., Stengl, C., Dinkel, F., Dorsch, S., Murillo, C., Seeber, S., Gnirs, R., Runz, A., Echner, G., Karger, C.P., Jäkel, O., 2022. An abdominal phantom with anthropomorphic organ motion and multimodal imaging contrast for MR-guided radiotherapy. *Physics in Medicine and Biology* **67**. doi:10.1088/1361-6560/ac4ef8.
- Yadav, N., Singh, M., Mishra, S.P., 2021. Tissue-equivalent materials used to develop phantoms in radiation dosimetry: A review. *Materials Today: Proceedings* **47**, 7170–7173. doi:10.1016/j.matpr.2021.06.359.

- Yan, W., Khan, M.K., Wu, X., Simone, C.B., Fan, J., Gressen, E., Zhang, X., Limoli, C.L., Bahig, H., Tubin, S., Mourad, W.F., 2019. Spatially fractionated radiation therapy: History, present and the future. *Clinical and Translational Radiation Oncology* **20**, 30–38. doi:10.1016/j.ctro.2019.10.004.
- Yonai, S., Arai, C., Shimoyama, K., Fournier-Bidoz, N., 2018. Experimental evaluation of dosimetric characterization of gafchromic EBT3 and EBT-XD films for clinical carbon ion beams. *Radiation Protection Dosimetry* **180**, 314–318. doi:10.1093/RPD/NCY006.
- Zeng, C., Li, X., Lu, W., Reyngold, M., Gewanter, R.M., Cuaron, J.J., Yorke, E., Li, T., 2020. Accuracy and efficiency of respiratory gating comparable to deep inspiration breath hold for pancreatic cancer treatment. *Journal of Applied Clinical Medical Physics* **22**, 218–225. doi:10.1002/acm2.13137.

8. Personal Contribution to Data Acquisition / Assessment and Personal Publications

8.1 Contribution to publications for cumulative thesis

The contribution of Christina Stengl (CS) to each of the three publications constituting this cumulative thesis is detailed below, according to the Contributor Roles Taxonomy⁵.

Paper I

CS played a key role in the **conceptualization** of **Paper I**, outlining the design of the phantom and defining research objectives to ensure compatibility with MRI, CT, and CIRT. Additionally, CS implemented the **methodology** and developed both the phantom's external and internal structures, did the 3D design and printing of organs and dosimetric inserts, and planned the experiments and irradiations. CS programmed the **software** for the motion system. CS led the **investigation** by performing MRI and CT measurements and the irradiation at HIT. Furthermore, CS contributed to the **validation** and **formal analysis**, conducting MRI and CT image analysis, motion analysis as well as IC and film analysis. In addition to **data curation**, CS **wrote the original draft** and subsequent **review and editing** stages. Her contributions also encompassed **visualization**, including the creation of all the pictures and graphs used in the publication.

Paper II

CS made significant contributions to **Paper II**. CS **conceptualized** the idea of a variable mini-beam collimator with interchangeable metal and plastic plates. In

⁵<https://credit.niso.org/>, accessed on 8 May 2024.

terms of **methodology**, CS 3D-designed the plastic plates and scaffold for the mini-beam collimator, and planned the irradiation of films and cells with an X-ray machine. Her contribution in **software** was conducting the film analysis. In the **investigation** phase, CS performed experiments with the mini-beam collimator, conducting film and IC dosimetry and *in vitro* studies. Additionally, CS significantly contributed to **formal analysis**, including film and microscopy analysis of cell data, as well as **data curation**. CS did the **visualization**, which encompassed creating all plots and microscopy images for the paper. CS wrote the manuscript, including **original draft preparation**, as well as **review and editing** stages.

Paper III

CS **conceptualized** the integration of carbon ion radiation therapy and mini-beam radiotherapy with the developed phantom and the mini-beam collimator, as reported in **Paper III**. In terms of **methodology**, CS adapted the mini-beam collimator for carbon ion irradiations and planned and executed irradiation at HIT. CS refined the **software** to conduct film analysis. For the **investigation**, CS supervised the experiments at HIT. Additionally, CS did the **formal analysis**, including the analysis of films and mini-beam patterns from Monte Carlo simulations and experiments. CS played the main role in **data curation** and **visualization**, which involved creating and adapting all the plots and images. Furthermore, she wrote the manuscript, including the **original draft preparation**, as well as the **review and editing** stages.

8.2 Peer-reviewed publications

1. **Stengl, C.**, Muñoz, I. D., Arbes, E., Rauth, E., Christensen, J. B., Vedelago, J., Runz, A., Jäkel, O., & Seco, J. (2024). Dosimetric study for breathing-induced motion effects in an abdominal pancreas phantom for carbon ion mini-beam radiotherapy. *Medical Physics*, Advance online publication. doi:10.1002/mp.17077
2. **Stengl, C.**, Panow, K., Arbes, E., Muñoz, I. D., Christensen, J. B., Neelsen, C., Dinkel, F., Weidner, A., Runz, A., Johnen, W., Liermann, J., Echner, G., Vedelago, J., & Jäkel, O. (2023). A phantom to simulate organ motion and its effect on dose distribution in carbon ion therapy for pancreatic cancer. *Physics in Medicine and Biology*, 68(24), doi:10.1088/1361-6560/ad0902
3. Christensen, J. B., Muñoz, I. D., Bassler, N., **Stengl, C.**, Bossin, L., Togno, M., Safai, S., Jäkel, O., & Yukihiro, E. G. (2023). Optically stimulated luminescence detectors for dosimetry and LET measurements in light ion

beams. *Physics in Medicine and Biology*, 68(15), doi:10.1088/1361-6560/acdfb0

4. **Stengl, C.**, Arbes, E., Thai, L. J., Echner, G., Vedelago, J., Jansen, J., Jäkel, O., & Seco, J. (2023). Development and characterization of a versatile mini-beam collimator for pre-clinical photon beam irradiation. *Medical Physics*, 50(8), 5222–5237. doi:10.1002/mp.16432
5. Ghafoory, S., **Stengl, C.**, Kopany, S., Mayadag, M., Mechtel, N., Murphy, B., Schattschneider, S., Wilhelmi, N., & Wölfl, S. (2022). Oxygen Gradient Induced in Microfluidic Chips Can Be Used as a Model for Liver Zonation. *Cells*, 11(23), 3734. doi: 10.3390/cells11233734
6. **Stengl C**, Ghafoory S, Weidner A, Murphy B, Wölfl S. Development of an Artificial 3D Liver Phantom for Analysis of Radiotherapeutic Effects In Vitro. *Applied Sciences*. 2022; 12(21):10867. doi:10.3390/app122110867
7. Weidner, A., **Stengl, C.**, Dinkel, F., Dorsch, S., Murillo, C., Seeber, S., Gnirs, R., Runz, A., Echner, G., Karger, C. P., & Jäkel, O. (2022). An abdominal phantom with anthropomorphic organ motion and multimodal imaging contrast for MR-guided radiotherapy. *Physics in Medicine and Biology*, 67(4). doi:10.1088/1361-6560/ac4ef8
8. Hoffmann, M. D., Mathony, J., Upmeier Zu Belzen, J., Harteveld, Z., Aschenbrenner, S., **Stengl, C.**, Grimm, D., Correia, B. E., Eils, R., & Niopek, D. (2021). Optogenetic control of *Neisseria meningitidis* Cas9 genome editing using an engineered, light-switchable anti-CRISPR protein. *Nucleic Acids Research*, 49(5), e29. doi:10.1093/nar/gkaa1198
9. Mathony, J., Harteveld, Z., Schmelas, C., Upmeier Zu Belzen, J., Aschenbrenner, S., Sun, W., Hoffmann, M. D., **Stengl, C.**, Scheck, A., Georgeon, S., Rosset, S., Wang, Y., Grimm, D., Eils, R., Correia, B. E., & Niopek, D. (2020). Computational design of anti-CRISPR proteins with improved inhibition potency. *Nature Chemical Biology*, 16(7), 725–730. doi:10.1038/s41589-020-0518-9

8.3 Conference contributions

1. Invited Talk: ASI Seminar 2024, Paul Scherrer Institute (PSI), Switzerland; Optimization of pancreatic cancer therapy - Potential and challenges of treatment approaches.
2. Invited Talk: Science@DKFZ 2023, Heidelberg, Germany; Development and characterization of a versatile mini-beam collimator for pre-clinical photon beam irradiation.

3. Oral Presentation: ESTRO 2023, Vienna, Austria; Multimodal anthropomorphic pancreas phantom with real-time breathing motion for Carbon Ion radiotherapy.
4. Oral Presentation: International Workshop on Particle Minibeam Therapy 2023, Paris, France; Dosimetry and in vitro studies using a novel and versatile mini-beam collimator.
5. Poster: NCRO Retreat 2023, Heidelberg, Germany; PPIeT: Pancreas Phantom for Carbon Ion beam Therapy.
6. Oral Presentation: FRPT 2022, Barcelona, Spain; Development of a versatile mini-beam collimator.
7. Oral Presentation: ECMP 2022, Dublin, Ireland; Spatial fractionation: Development of a variable and low-cost mini-beam collimator.
8. Oral Presentation: DGMP 2021, online: Development of an anthropomorphic breathing phantom for IGRT.
9. Poster, ESTRO 2021, online: Multimodal anthropomorphic abdomen phantom with real-time breathing motion for IGRT

9. Appendix

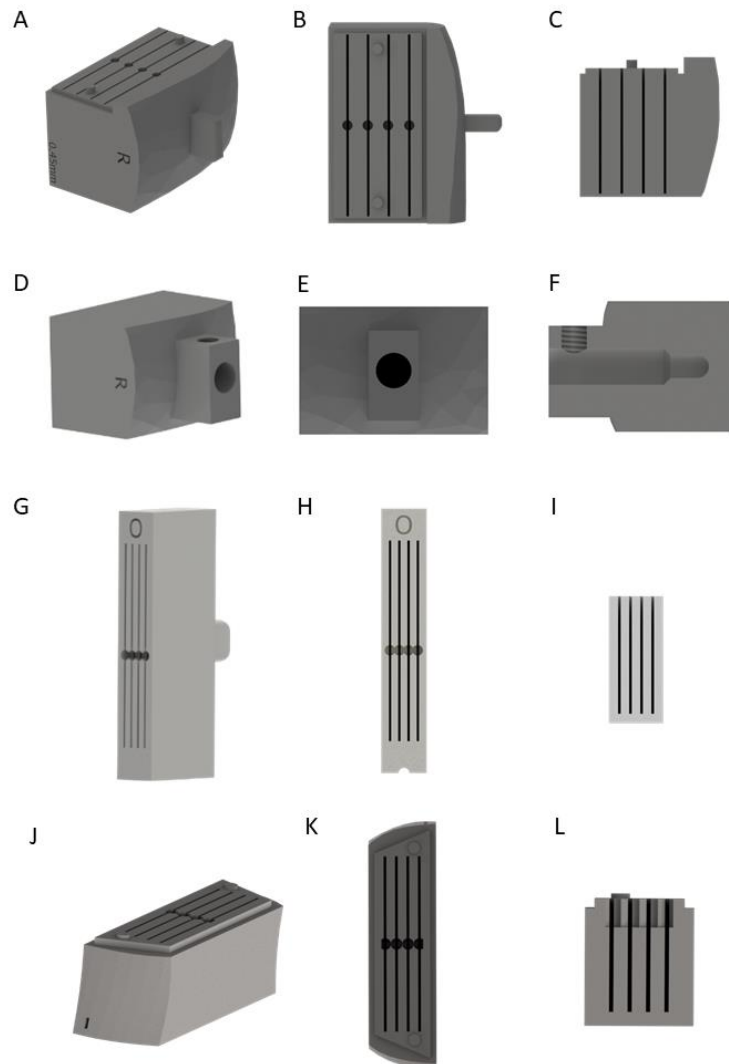
9.1 Supplementary material Paper I

A phantom to simulate organ motion and its effect on dose distribution in carbon ion therapy for pancreatic cancer

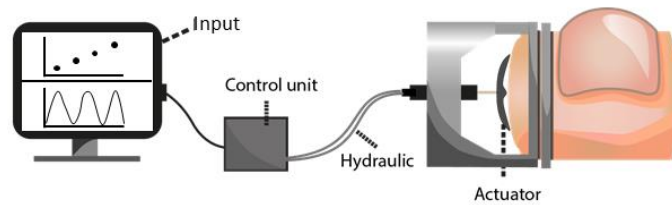
Supplementary Material

Supplementary Table S1: Composition of organ filling to achieve human-equivalent contrast (Elter et al., 2021). The total volume is overestimated to have enough solution to fill the pancreas or the two kidneys.

Organ \ Material	Agarose [g]	NiDTPA [mL]	KCl [g]	Water [mL]
Pancreas	18.67	11.60	9.50	469.73
Kidney	10.48	7.89	3.51	481.63

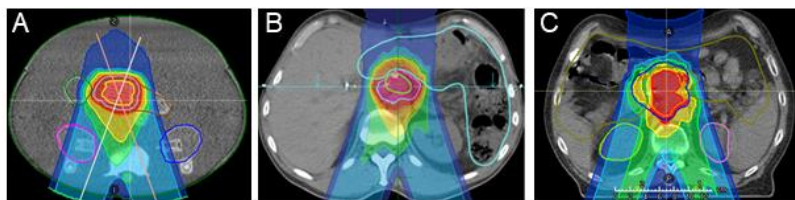


Supplementary Figure S1: 3D printed detector inserts. Film insert for the pancreas as 3D rendering (A), top view (B) and an inside view (C). Insert for the ionization chamber in the pancreas as 3D rendering (D), side view (E) and inside view (F). Films insert for the kidney as 3D rendering (G), top view (H) and inside view (I). Film insert for the spine as 3D rendering (J), top view (K) and inside view (L).

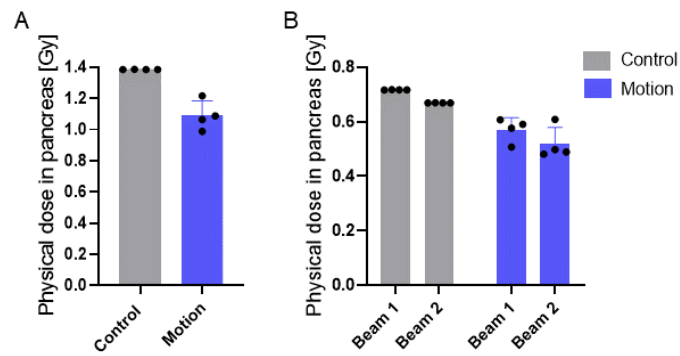


Supplementary Figure S2: Illustration of the motion control for PPIeT. Input feed of either a fixed motion input or a sinusoidal breathing motion is transferred to the control unit and via a hydraulic system the actuator is moved accordingly.

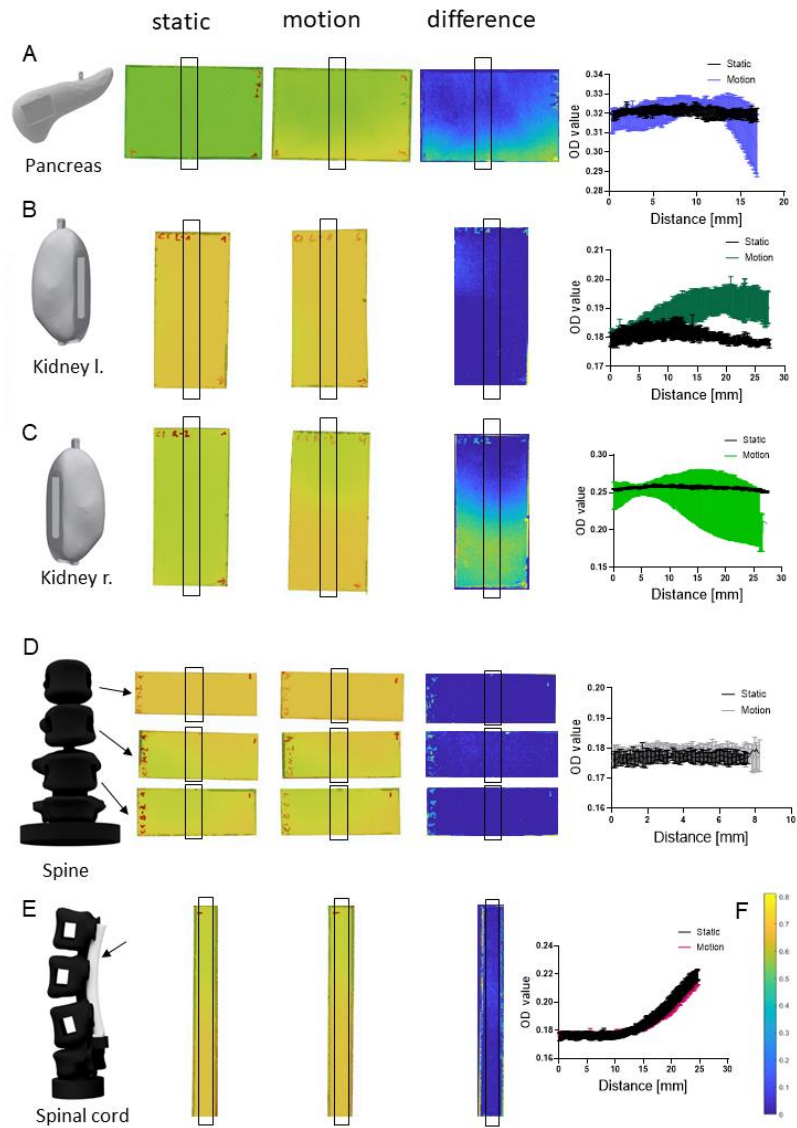
Supplementary Video S1: Recording of PPIeT during breathing-induced motion. The initial sequence of the video presents the motion of the abdominal wall. In the subsequent part of the video, the motion of the kidneys is visible while the spine does not exhibit motion. The video is given as extra .mp4 file.



Supplementary Figure S3: Carbon ion treatment plan for pancreatic cancer for PPIeT (A), from a previous study (adapted from Liermann et al., 2022. CC BY 4.0) (B), and from a randomly selected patient from the pancreas motion quantification study (C).



Supplementary Figure S4: Total physical dose for both beams in static condition (Control) and motion condition (A). The 1.37 Gy physical dose calculated in the treatment plan matched the mean physical dose measured with the ionization chamber with a deviation of 1.17 %. Single beam contribution to the total physical dose in static condition and motion condition (B).



Supplementary Figure S5: Raw film data for static and motion conditions, along with the OD two-dimensional difference and OD profile in CC direction for static and motion conditions in the pancreas (A), the left (B) and right (C) kidney, the spine (D) and the spinal cord (E). Scale bar for film overlay with unit OD value (F). The black boxes indicate the region used for the profiles. The size of the films for each organ is described in Section "2.3. 3D printing of detector inserts".

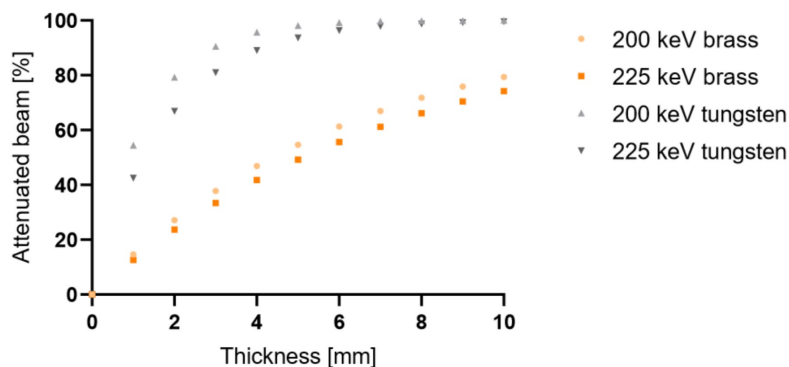
9.2 Supplementary material Paper II

Supplementary material

Development and characterization of a versatile mini-beam collimator
for pre-clinical photon beam irradiation

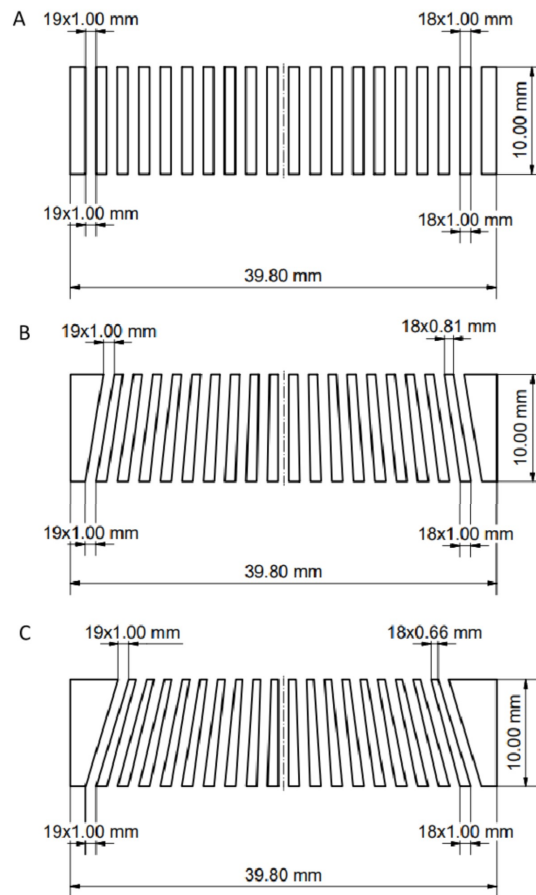
Christina Stengl, Eric Arbes, Long-Yang Jan Thai, Gernot Echner,
José Vedelago, Jeannette Jansen, Oliver Jäkel, Joao Seco

Submitted to *Medical Physics* on November 2022.

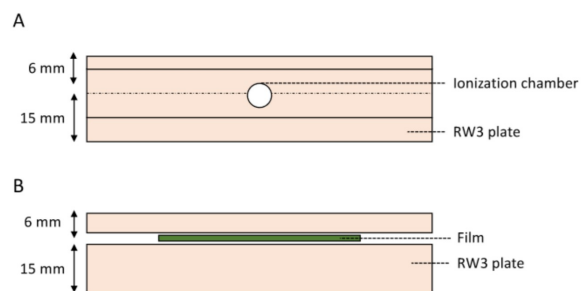


Supplementary Figure S1: Attenuation of tungsten and brass over a thickness of 10 mm. To justify the choice of the 10 mm thick metal plates, the attenuated beam in percentage is plotted against the thickness in mm for monoenergetic photon beams with energies of 200 keV and 225 keV. As continuous X-ray beams were used, the attenuation values represent the worst-case scenarios, since these energies are the maximum energies of the two X-ray beams used, and lower energies can be attenuated up to the same percentage with lower thicknesses. The gray color symbols correspond to tungsten and the orange color symbols correspond to brass. The reported values were retrieved from Hubbell and Seltzer (2004). The attenuation for brass was computed considering a mixture of 2/3 of copper and 1/3 of zinc.

Hubbell and Seltzer, 2004. <https://dx.doi.org/10.18434/T4D01F>



Supplementary Figure S2: Technical drawing of the plastic plates arranged for each mini-beam collimator at the different SCDs. At SCD_A no divergence was considered, thus parallel plastic plates were used. Instead, for SCD_B and SCD_C the divergence compensation is evident in the design of the plastic plates. The hollowed parts of the designs are filled with 1 mm thick metal plates, and they repeat 19 times for all the configurations. According to the norms of technical drawings, the number multiplying the length indicates that this structure is repeated that number of times. For example, for SCD_A the 1 mm thickness is repeated 18 times. For SCD_B and SCD_C , at the top part, the 0.81 mm and 0.66 mm is respectively repeated 18 times. The dash lines in the middle are symmetry lines.



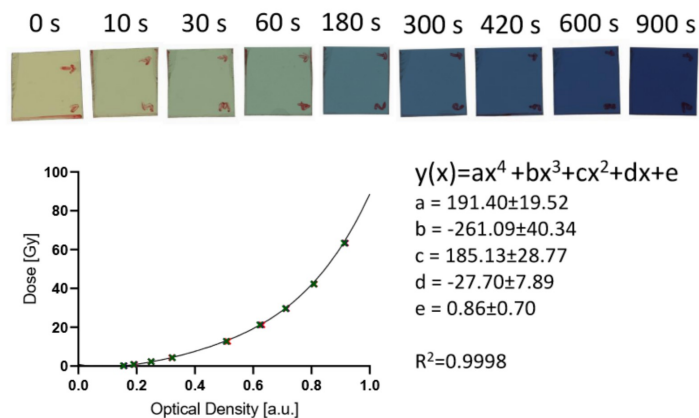
Supplementary Figure S3: RW3 plate setup for absolute dosimetry where radiation is coming from top to bottom. An ionization chamber was placed in an RW3 center plate with a form-fitting hole extending into the center of the plate with a total thickness of 10 mm. On top, a 4 mm RW3 plate was positioned to achieve 6 mm of water-equivalent depth (A). Gafchromic films were positioned accordingly in the MultiRad with a water-equivalent depth of 6 mm above the film (B).

Supplementary Table S1: Dose rate measurements done with the Semiflex Ionization Chamber 31010 from PTW (Germany), with a calibration factor of 2.827×10^8 Gy/C ($T_0=293.15$ K; $P_0=1013.25$ mbar) at SCD_A . The collected charge was measured with the ionization chamber on four different days, by doing five independent acquisitions of two minutes each day. For every day, temperature and pressure corrections were considered, and the mean charge was converted to dose by multiplying by the calibration factor of the chamber. The dose rate value used for irritations at SCD_A was computed as the mean value, and its standard deviation is reported as uncertainty, yielding a mean dose rate of $\dot{D}_A = (4.217 \pm 0.035)$ Gy/min.

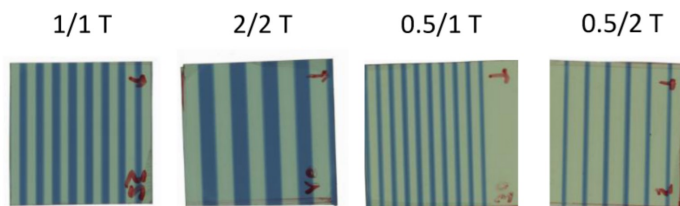
Measurement	Charge [nC]	T [°C]	P [mbar]	Dose rate [Gy/min]
Day 1	29.85	21.95	1005.8	4.265
	29.77			
	29.75			
	29.70			
	29.71			
Day 2	28.82	23.35	1004.1	4.189
	28.92			
	29.16			
	29.15			
	29.14			
Day 3	29.27	23.35	1004.1	4.222
	29.28			
	29.27			
	29.26			
	29.24			
Day 4	29.13	23.45	1005.5	4.193
	29.13			
	29.11			
	29.10			
	29.10			

Supplementary Table S2: Dose rate measurements done with the Semiflex Ionization Chamber 31010 from PTW (Germany), with a calibration factor of 2.827×10^8 Gy/C ($T_0=293.15$ K; $P_0=1013.25$ mbar) at SCD_B . The collected charge was measured with the ionization chamber on four different days, by doing five independent acquisitions of two minutes each day. For every day, temperature and pressure corrections were considered, and the mean charge was converted to dose by multiplying by the calibration factor of the chamber. The dose rate value used for irritations at SCD_B was computed as the mean value, and its standard deviation is reported as uncertainty, yielding a mean dose rate of $\dot{D}_B = (17.74 \pm 0.20)$ Gy/min.

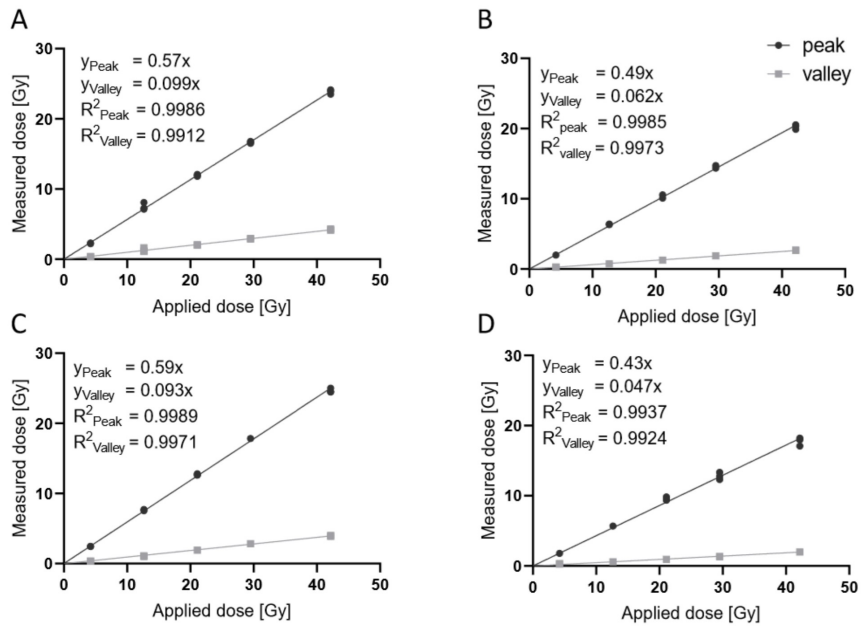
Measurement	Charge [nC]	T [°C]	P [mbar]	Dose rate [Gy/min]
Day 1	121.9	22.10	1004.9	17.487
	121.9			
	121.8			
	121.6			
	121.9			
Day 2	123.8	21.80	1007.4	17.686
	123.8			
	123.7			
	123.4			
	123.5			
Day 3	125.1	22.65	1009.5	17.875
	124.6			
	124.8			
	124.8			
	125.0			
Day 4	125.1	22.5	1006.6	17.920
	125.1			
	125.1			
	124.6			
	124.5			



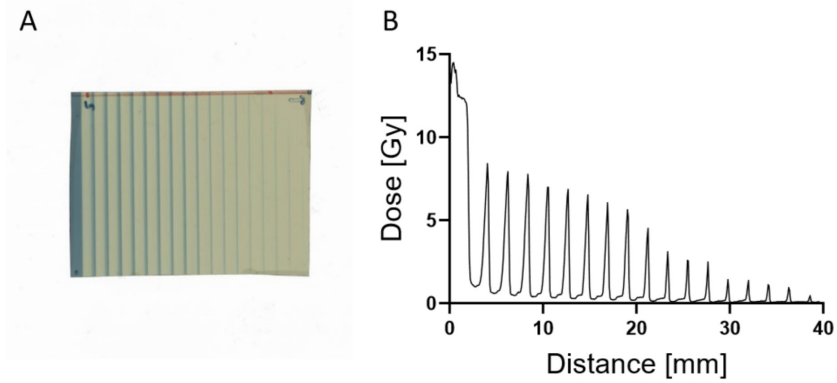
Supplementary Figure S4: On top, the raw data of the scanned films for the calibration curve are shown for each irradiation time with a size of $1.5 \times 1.5 \text{ cm}^2$. The red marks were used to identify the films and reproduce their positioning. For each film, an average of 100 pixels along the horizontal direction was used. The plot on the bottom left depicts the Optical Density mean values from three independent film measurements and the 4th-order polynomial fit. The resulting fitting parameters are reported on the right.



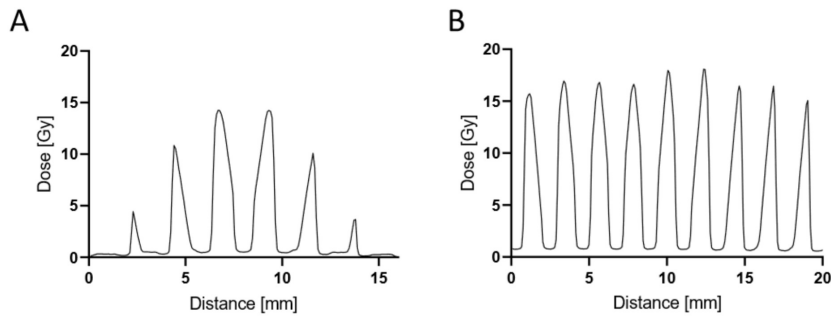
Supplementary Figure S5: Raw data of the scanned films irradiated at the *in vitro* setup of SCD_A for configuration 1/1 T, 2/2 T, 0.5/1 T and 0.5/2 T. The red marks were used to identify the films and reproduce their positioning.



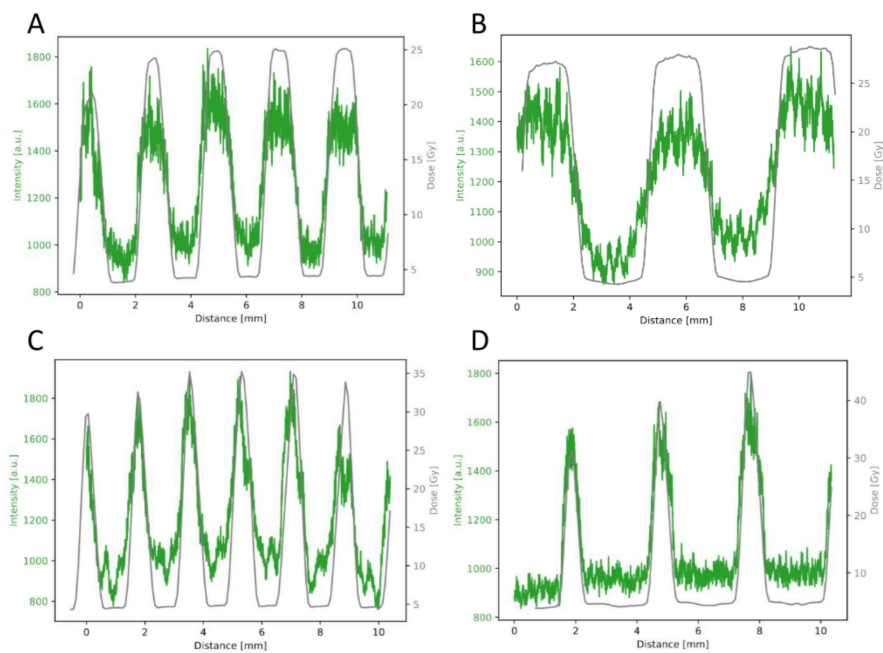
Supplementary Figure S6: Peak dose and valley dose for the mini-beam collimator configurations 1/1 T (A), 2/2 T (B), 0.5/1 T (C), and 0.5/2 T (D). The applied dose is the dose determined with the ionization chamber at SCD_A , and the measured dose is the one resulting from the film measurements with each collimator configuration. A linear fit was made for each data set, setting the intercept to zero. The resulting fitting parameters are reported for each subplot. From the slopes, it can be inferred that the presence of the mini-beam collimator yields a dose value at the peak that is on average two times lower than in the case without the collimator. For the valley regions, the dose is one order of magnitude lower compared to the situation without the mini-beam collimator.



Supplementary Figure S7: Effect of intentional misalignment of the mini-beam collimator. Raw film data (A) when positioning the mini-beam collimator 15 mm off from the center, and resulting mini-beam dose profiles (B). This irradiation was done with the 1/1 T mini-beam collimator configuration at SCD_C . A clear difference in the peak intensities is observed, with a continuous drop in intensity from left to right. This illustrates the relevance of properly aligning the mini-beam collimator to the center of the X-ray radiation field.



Supplementary Figure S8: Dose profiles of mini-beam collimator with 1/1 T configuration using parallel plates (A) and plastic plates accounting for divergence (B) at SCD_C . The drop in intensity of the lateral peaks in A is evident, with 69% less dose than the central peaks. This difference indicates the importance of considering the X-ray beam divergence in the plastic plate design for the mini-beam collimator at lower SCD_C s.



Supplementary Figure S9: Overlay of the *in vitro* fluorescence intensity (in green) and the dose measured with the EBT-XD film (in gray) for the mini-beam collimator configurations 1/1 T (A), 2/2 T (B), 0.5/1 T (C), and 0.5/2 T (D). The original profiles are reported in Fig. 3 and Fig. 9 for EBT-XD films and the *in vitro* study, respectively. In all the cases, it can be observed that the fluorescence intensity profiles follow the mini-beam dose distribution. This can also be seen in the agreement between the geometrical parameters FWHM and ctc reported in Supplementary Table S3. Instead, the difference between the peak and the valley is always larger for the dose mini-beam profiles, yielding larger PVDR values than PVIR values.

Supplementary Table S3: Comparison of mini-beam parameters for film measurements and *in vitro* irradiations. The original values reported are in Table 3 and Table 6. The uncertainties were computed considering σ_{inter} and σ_{intra} as independent contributions. It can be observed that the geometrical parameters FWHM and ctc obtained with the two different measurements agree with the uncertainties for all the mini-beam collimator configurations. This behavior is visible in the overlapping profiles in Supplementary Fig. S9. Due to the nature of the measurement *in vitro*, the uncertainties are always larger than for film measurements. In addition, PVDR values are systematically higher than PVIR values because in the latter the intensities correspond to the discrete signal originating in the cell foci, instead of the continuous profile obtained with films. Furthermore, as the foci intensity profiles present a larger dispersion, the relative uncertainties of the PVIR values are larger than the PVDR values.

Mini-beam collimator ID	Measurement	FWHM [mm]	ctc [mm]	PVDR	PVIR
1/1 T	Films	0.98±0.08	2.30±0.01	6.38±0.24	-
1/1 T	<i>In vitro</i>	1.18±0.10	2.29±0.03	-	1.68±0.68
2/2 T	Films	2.11±0.09	4.61±0.02	7.03±0.23	-
2/2 T	<i>In vitro</i>	2.35±0.17	4.60±0.17	-	1.56±0.11
0.5/1 T	Films	0.53±0.05	1.77±0.01	8.66±0.75	-
0.5/1 T	<i>In vitro</i>	0.69±0.08	1.75±0.04	-	1.57±0.12
0.5/2 T	Films	0.52±0.05	2.93±0.03	10.09±1.07	-
0.5/2 T	<i>In vitro</i>	0.66±0.11	2.87±0.14	-	1.64±0.23

9.3 Supplementary material Paper III

Supplementary material

Dosimetric study for breathing-induced motion effects in an abdominal pancreas phantom for carbon ion mini-beam radiotherapy

Christina Stengl, Iván D. Muñoz, Eric Arbes, Evelyn Rauth, Jeppe B. Christensen, José Vedelago, Armin Runz, Oliver Jäkel, Joao Seco

Submitted to Medical Physics on November 2023.

Supplementary Section S.I. Energies of the treatment plans

Supplementary Table S1: Energy, SOBP relative weight and focal spot FWHM size of Beam 1.

Energy [MeV/u]	SOBP relative weight	Focal spot FWHM [mm]
226.05	0.01160	10.3
229.76	0.03279	10.2
233.42	0.04459	10.2
237.05	0.05349	10.2
240.65	0.05799	10.2
244.21	0.05889	10.2
247.74	0.06049	10.1
251.24	0.06719	10.1
254.71	0.08028	10.1
258.15	0.08608	10.1
261.56	0.09468	10.1
264.95	0.10548	10.1
268.32	0.10558	10.1
271.66	0.09558	10.0
274.98	0.04079	10.0
278.29	0.00450	10.0

Supplementary Table S2: Energy, SOBP relative weight and focal spot FWHM size of Beam 2.

Energy [MeV/u]	SOBP relative weight	Focal spot FWHM [mm]
229.76	0.00490	10.2
233.42	0.01220	10.2
237.05	0.02140	10.2
240.65	0.02940	10.2
244.21	0.03620	10.2
247.74	0.04080	10.1
251.24	0.05149	10.1
254.71	0.05819	10.1
258.15	0.06599	10.1
261.56	0.07859	10.1
264.95	0.08419	10.1
268.32	0.09099	10.1
271.66	0.09459	10.0
274.98	0.09019	10.0
278.29	0.08759	10.0
281.57	0.07199	10.0
284.84	0.05379	10.0
288.10	0.02380	10.0
291.34	0.00370	10.0

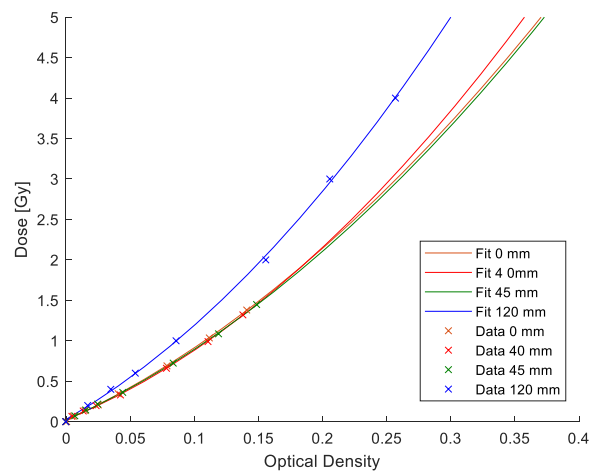
Supplementary Section S.II. Film calibration for carbon ion beam dosimetry

To achieve dose values for the films, a calibration curve was done for each mentioned depth. The calibration films were cut with a size of (30×30) mm² and placed at the center of the RW3 phantom for $\{0; 40; 45; 120\}$ mm. For the irradiation, the mini-beam collimator was positioned 50 mm in front of the RW3 plates. To match the energies, and consequently the LET values, of the clinical plan for PPIeT, two different plans were used for the calibration of the films. Calibration beam 1 was set according to the energies and relative weights of Beam 1 used for PPIeT. Calibration beam 2 was calculated accordingly based on the energies and relative weights of Beam 2 used for PPIeT. These calibration plans have a field size of (26×26) mm² with each pencil beam spot 2 mm apart from each other, and focal spot sizes between 10.0 mm to 10.2 mm FWHM, depending on the energy of each layer. This way, a homogeneous irradiation of the calibration films was achieved.

The absolute dose values were determined with a 0.03 cm³ PinPoint 31015 ionization chamber (PTW, Germany), and measured independently for calibration beam 1 and calibration beam 2. The absolute number of primary particles was adjusted to obtain 1 Gy at 120 mm for each calibration beam. For the calibration beam 1, the dose was measured at the entrance region for the 0 mm depth and at depths of 45 mm and 120 mm. For the calibration beam 2, the dose was measured at 40 mm and 120 mm depth. For the calibration irradiation, films were placed at 0 mm, 45 mm and 120 mm for calibration beam 1. Afterwards, only the film at 120 mm was kept inside the RW3 phantom, and a new film was placed at 45 mm, following irradiation with calibration beam 2. By doing this, the LET distribution at 120 mm is the same as the one in the pancreas, composed of the contribution of the two beams. This procedure was repeated several times while scaling the number of primary particles to obtain several dose reference values for the OD-dose calibrations.

Supplementary Table S3: Dose values in Gy at depths {0; 40; 45; 120} mm within the RW3 phantom for calibration beam 1 and calibration beam 2 measured with the ionization chamber. The uncertainty was computed by considering the calibration certificate of the chamber, the temperature and pressure corrections, and the standard deviation of three independent measurements.

	0 mm	40 mm	45 mm	120 mm
Calibration beam 1	0.690 ± 0.016	-	0.724 ± 0.018	0.998 ± 0.025
Calibration beam 2	-	0.660 ± 0.016	-	1.004 ± 0.024

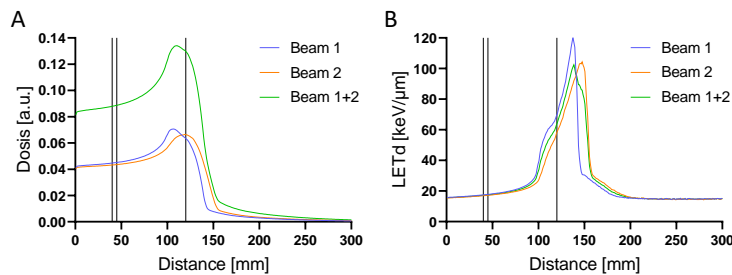


Supplementary Figure S1: Dose-calibration of EBT3 gafchromic films for each depth.

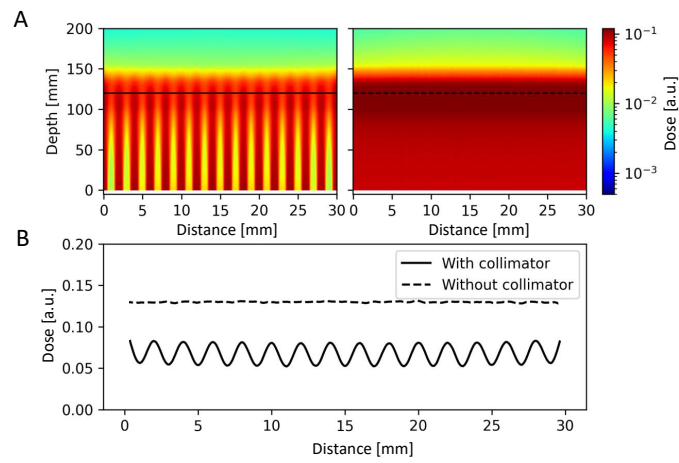
Supplementary Section S.III. Monte Carlo simulations

Supplementary Table S4: Summary of the Monte Carlo simulation parameters as proposed by Sechopoulos et al. (2018)¹. Further details related to the Monte Carlo simulations can be found in a previous publication².

Item name	Description	References
Code, version	TOPAS, version 3.9.1	3
Validation	Depth-dose measurements against simulations	2
Timing	2×48 cores, CPU time 5×10^6 s	
Geometry	The mini-beam collimator geometry is detailed in the manuscript. The dose and LET were scored in an RW3 phantom with dimensions $(400 \times 300 \times 300)$ mm ³ . The scoring grid was set to 400 bins along the central axis with 300 bins in the horizontal plane to score the mini beam pattern with a resolution of 10 bins/mm	
Physics	A modular list consisting of <code>g4decay</code> , <code>g4h-elastic_HP</code> , <code>g4em-standard_opt4</code> , <code>g4h-phy_QGSP_BIC_HP</code> , <code>g4stopping</code> , <code>g4ion-binarycascade</code>	
Scoring	Dose to water and dose-averaged LET in water; the latter excluding secondaries heavier than the primary particle	
# histories	10^9 primary total with the weights given in Supplementary Table S1 and Supplementary Table S2	

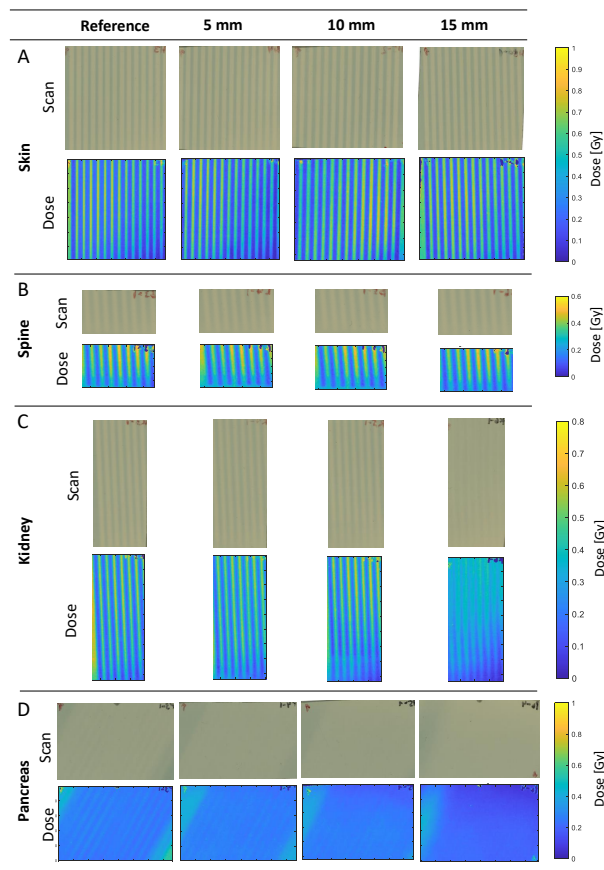


Supplementary Figure S2: Dose values (A) and LET_d (B) profiles for calibration beam 1 (blue), calibration beam 2 (orange), and their combined beam (green). Black lines indicate the depths of 0 mm for skin, 40 mm for spine, 45 mm for kidney, and 120 mm for pancreas.



Supplementary Figure S3: Comparison of dose distribution with mini-beam collimator (left) and without mini-beam collimator (right) (A). Black line indicates the depth of 120 mm from where the dose profile for both conditions was used. Dose profiles at 120 mm with mini-beam collimator (black line) and without collimator (black dotted line) (B). This result shows that if the same number of primary carbon ions are simulated, the mean peak dose is 61.3 % of the mean dose without the mini-beam collimator.

Supplementary Section S.IV. Quantification of the mini-beam dose distribution with films

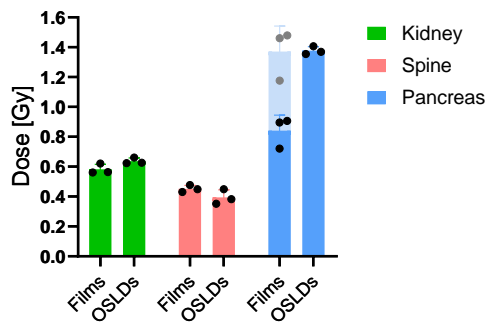


Supplementary Figure S4: Visualization of 2D film raw data and dose distribution at the skin (A), spine (B), kidney (C) and pancreas (D) for reference condition, 5 mm motion, 10 mm motion and 15 mm motion.

Supplementary Section S.V. Optically simulated luminescence detectors

Optically stimulated luminescent dosimeters (OSLDs) based on $\text{Al}_2\text{O}_3:\text{C}$ are capable of performing dosimetry measurements in light ion beams². Although the dose is subject to an ionization quenching, the inherent way of assessing the radiation quality through averaged LET enables quenching-corrected dosimetry. After irradiation, the material is characterized by two emissions during stimulation, one emission in the UV band and another in the blue band of the optical spectrum. While each band is subject to non-linearity effects caused by variations in the ionization density, the ratio of the two emissions has been shown to correlate with the radiation quality, and in particular averaged LET⁴. This means that OSLDs can be used to determine both dose and averaged LET simultaneously, where the latter can be exploited to assess ionization quenching corrections factors, finally enabling dosimetry of carbon ion beams².

With the OSLDs embedded in the pancreas, a dose of (1.35 ± 0.05) Gy was measured when irradiating PPIeT with the two beams of the treatment plan without using the mini-beam collimator. This value agrees with the 1.37 Gy retrieved from the treatment plan and the (1.39 ± 0.03) Gy obtained with an ionization chamber previously reported⁵.



Supplementary Figure S5: Comparison of dose measured at the mean peak dose values of the mini-beam profiles in the films to the dose values measured by OSLDs without the collimator. The kidney, spine and pancreas are visualized in green, red and blue, respectively. For the pancreas, a correction factor (Supplementary Figure S3) derived from the MC simulation was applied and is visualized by the light blue bar.

References

- ¹ I. Sechopoulos, D. W. O. Rogers, M. Bazalova-Carter, W. E. Bolch, E. C. Heath, M. F. McNitt-Gray, J. Sempau, and J. F. Williamson, RECORDS: improved Reporting of monte Carlo RaDiation transport Studies: Report of the AAPM Research Committee Task Group 268, *Medical Physics* **45**, e1–e5 (2018). doi: 10.1002/mp.12702.
- ² J. B. Christensen, I. D. Muñoz, N. Bassler, C. Stengl, L. Bossin, M. Togno, S. Safai, O. Jäkel, and E. G. Yukihiro, Optically stimulated luminescence detectors for dosimetry and LET measurements in light ion beams, *Physics in Medicine & Biology* **68**, 155001 (2023). doi: 10.1088/1361-6560/acdfb0.
- ³ J. Perl, J. Shin, J. Schumann, B. Faddegon, and H. Paganetti, TOPAS: an innovative proton Monte Carlo platform for research and clinical applications, **39**, 6818–6837 (2022). doi: 10.1118/1.4758060.
- ⁴ J. B. Christensen, M. Togno, L. Bossin, O. V. Pakari, S. Safai, and E. G. Yukihiro, Improved simultaneous LET and dose measurements in proton therapy, *Scientific Reports* **12**, 8262 (2022). doi: 10.1038/s41598-022-10575-4.
- ⁵ C. Stengl, K. Panow, E. Arbes, I. D. Munoz, J. B. Christensen, C. Neelsen, F. Dinkel, A. Weidner, A. Runz, W. Johnen, J. Liermann, G. Echner, J. Vedelago, and O. Jäkel, A phantom to simulate organ motion and its effect on dose distribution in carbon ion therapy for pancreatic cancer, *Physics in Medicine and Biology* **68**, 245013 (2023). doi: 10.1088/1361-6560/ad0902.

Christina Stengl

Curriculum Vitae

Personal Information

 Worms, Germany

 christina.stengl@dkfz.de

 <https://www.linkedin.com/in/christina-stengl/>

 <https://orcid.org/0000-0003-0273-0878>

 Scopus Author Identifier: 57217976027

 Web of Science ResearcherID: JOK-0516-2023

Education

- 05/2021 - today **PhD Student**, German Cancer Research Center, Heidelberg, Prof. Dr. Oliver Jäkel
Topic: In-phantom dosimetry study for target and organs at risk during breathing-induced motion: improving pancreatic cancer treatment by combining carbon ion and mini-beam irradiation
- 10/2018 - 12/2020 **Master: Molecular Biotechnology**, Heidelberg University, Grade: 1.0
Topic: Simulation of phantom breathing motion for CT/MRI
- 10/2015 - 10/2018 **Bachelor: Molecular Biotechnology**, Heidelberg University, Grade: 1.1
Topic: The role of ORAI proteins in Ca²⁺ signaling and degranulation in murine peritoneal mast cells

Awards

- 2023 **PhD Poster Prize**, Granted by German Cancer Research Center (DKFZ)
- 2024 **Young Talent Award National Decade against Cancer**, Granted by Federal Ministry of Education and Research (BMBF)
- 2024 **Public Award price**, Future X Change, Granted by BMBF
- 2024 Selected as Young Scientist for the **73rd Lindau Nobel Laureate Meeting**, dedicated to Physics
- 2024 Selected for **Oral presentation** at 73rd Lindau Nobel Laureate Meeting

10. Acknowledgments

As a scientist, one of the most rewarding aspects is the collaborative nature of our profession, enriching our experience. It is thanks to the invaluable support of numerous individuals that I have been able to reach this stage in my journey. First and foremost I would like to thank my supervisor and doctor father Prof. Dr. Oliver Jäkel for allowing me to be part of an exceptional project at the intersection of medical physics and engineering. His guidance and support have been invaluable throughout my research process, offering me valuable insights and direction that significantly influenced the outcome of this thesis and my personal development. I want to extend my gratitude to Prof. Dr. Joao Seco, Dr. Jakob Liermann and Gernot Echner for being my Thesis Advisory Committee (TAC) and for their helpful suggestions, important guidance and insightful feedback in shaping the direction of my work. In particular, I thank Joao for providing me with lab space when most needed and for the warm welcome into his group. I would like to thank Jakob for his assistance in anatomy, ensuring everything was positioned correctly in PPIeT. Your input for the clinical know-how was incredibly enlightening, and I am grateful for the knowledge gained. I am especially thankful to Gernot, who was not only my TAC member, but also my group leader for most of my PhD. I would like to thank him for his advice on any engineering question and exceptional ideas, especially when I was drowning in a sea of technical terms. At this point, I would like to thank all my other core group members — Armin Runz, Wibke Johnen, and Anahita Bakhtiari Moghaddam for their continuous support and enjoyable conversations. Armin you made my PhD life as pleasant as possible with your support and dedication, even if the laser pointer was off and Wibke with whom I had the most enjoyable art and sewing sessions that you can have in the context of science. And let's not forget Artur Weidner and Fabian Dinkel for their friendship, and shared laughter that made our time productive and enjoyable. Additionally, the discussions and chats in the lab were thoroughly enjoyable with all of you from E041. A big thanks to Dr. Jeannette Jansen and Dr. Daniel Garcia for engaging in discussions, even when experiments seemed dauntingly hopeless. Your willingness to persevere through challenges made our collaborative efforts all the more rewarding. I extend my heartfelt gratitude to all my students that I had the pleasure to supervise during my time as PhD, Teresa Büning, Kathrin Panow, Long-Yang Jan Thai, Eric Arbes, Hüseyin Yildiz, Yun Joong Kim and Evelyn Rauth. I deeply appreciate all the great contributions, thought-provoking questions, and eagerness to learn from me. Your engagement has

been truly invaluable. Furthermore, I would like to thank the Bufdis and Bufdine we had over the last couple of years who helped with retrieving and cleaning my never-ending 3D printing jobs. During the last years of my PhD, I have had the privilege of collaborating closely with group members of the Dosimetry Group at the Paul Scherrer Institute under Dr. Eduardo G. Yukihara. Special thanks to Dr. Jeppe Brage Christensen for being my OSLD superhero, tirelessly aiding with the thousands of detectors I have thrown his way. And bonus points for making a visit to HIT to meet PPIeT face-to-face. A great thank you to Dr. José Vedelago for being my research wingman, both personally and professionally. Thanks for enduring countless hours dissecting manuscripts, cracking the reviewer's codes, and strategizing for prizes and conferences, your friendship and expertise have been priceless. I am also grateful for the help with the experiments at HIT from Ivan Munoz who sacrificed sleep to bombard OSLDs and ionization chambers with carbon ions. Also, I would like to thank Dr. Stephan Brons, the soul of HIT, for supplying me with all the essentials, especially beam time. And extra thanks for always bringing a smile to my face when you were on babysitting duty for little PPIeT. I'd like to extend a huge thank you to everyone at HIT, especially Alexander Neuholz, Beate Koczur, and Jan Knoll. Thank you for sitting with me to plan PPIeT's treatment. Additionally, I would like to thank Martina Jochim for her patients with me and PPIeT for the CT sessions we had. I want to extend my gratitude to the DKFZ mechanical workshop team for consistently providing me with the necessary parts and materials, even when the screws I required seemed to shrink to invisibility (M2 can be tiny). Your dedication and support truly saved the day. Furthermore, I would like to thank Michaela Schmitt for being more than just a colleague – she is been my partner in PhD crime! Together, we have conquered the peaks and valleys of this academic journey, whether by chatting it out in our office or fueling up on hot chocolate and coffee. I am immensely thankful for Emma Koeleman, who started as my Dutch and German tandem (at least we tried) and ended up as an incredible friend. Our journey began with crash courses in Dutch but evolved into a fantastic friendship, including countless gaming nights and movie marathons. I would like to express my gratitude to Dr. Roger Ottenheijm, whose encouragement and unwavering support have been crucial in completing this demanding endeavor. Thank you especially for the bottomless coffee cups! I would like to express my profound appreciation to my mum, my brother and my grandma, who supported me in my journey to becoming a Dr. Despite my lack of diagnostic superpowers, their support has been invaluable and greatly appreciated.

Finally, I would like to thank PPIeT, the real hero of this thesis who endured scars and battle wounds during our experiments, underwent more repairs than a vintage car, and even had a few organ transplants but still held on till the bitter end.

11. Eidesstattliche Versicherung

1. Bei der eingereichten Dissertation zu dem Thema **In-phantom dosimetry study for target and organs at risk during breathing-induced motion: improving pancreatic cancer treatment by combining carbon ion and mini-beam irradiation** handelt es sich um meine eigenständig erbrachte Leistung.
2. Ich habe nur die angegebenen Quellen und Hilfsmittel benutzt und mich keiner unzulässigen Hilfe Dritter bedient. Insbesondere habe ich wörtlich oder sinngemäß aus anderen Werken übernommene Inhalte als solche kenntlich gemacht.
3. Die Arbeit oder Teile davon habe ich bislang nicht an einer Hochschule des In- oder Auslands als Bestandteil einer Prüfungs- oder Qualifikationsleistung vorgelegt.
4. Die Richtigkeit der vorstehenden Erklärungen bestätige ich.
5. Die Bedeutung der eidesstattlichen Versicherung und die strafrechtlichen Folgen einer unrichtigen oder unvollständigen eidesstattlichen Versicherung sind mir bekannt.

Ich versichere an Eides statt, dass ich nach bestem Wissen die reine Wahrheit erklärt und nichts verschwiegen habe.

Heidelberg, 24.06.2024
Ort und Datum

Unterschrift